

Semiannual Technical Report

Interface Properties of Wide Bandgap Semiconductor Structures

Supported under Grant #N00014-92-J-1477
Office of the Chief of Naval Research
Report for the period 7/1/96-12/31/96

R. F. Davis, S. Bedair*, J. Bernholc†, R. J. Nemanich†, and Z. Sitar
c/o Materials Science and Engineering Department,
*Electrical and Computer Engineering Department
and †Department of Physics
North Carolina State University
Campus Box 7907
Raleigh, NC 27695-7907

19970121 135

December, 1996

DISTRIBUTION STATEMENT A

Approved for public release;
Distribution Unlimited

DTIC QUALITY INSPECTED 1

REPORT DOCUMENTATION PAGE			Form Approved OMB No. 0704-0188	
Public reporting burden for this collection of information is estimated to average 1 hour per response, including the time for reviewing instructions, searching existing data sources, gathering and maintaining the data needed, and completing and reviewing the collection of information. Send comments regarding this burden estimate or any other aspect of this collection of information, including suggestions for reducing this burden to Washington Headquarters Services, Directorate for Information Operations and Reports, 1215 Jefferson Davis Highway, Suite 1204, Arlington, VA 22202-4302, and to the Office of Management and Budget Paperwork Reduction Project (0704-0188), Washington, DC 20503.				
1. AGENCY USE ONLY (Leave blank)		2. REPORT DATE December, 1996	3. REPORT TYPE AND DATES COVERED Semiannual Technical 7/1/96-12/31/96	
4. TITLE AND SUBTITLE Interface Properties of Wide Bandgap Semiconductor Structures			5. FUNDING NUMBERS uri41114a-01 1114SS N00179 N66005 4B855	
6. AUTHOR(S) R. F. Davis, S. Bedair, J. Bernholc, R. J. Nemanich, and Z. Sitar				
7. PERFORMING ORGANIZATION NAME(S) AND ADDRESS(ES) North Carolina State University Hillsborough Street Raleigh, NC 27695			8. PERFORMING ORGANIZATION REPORT NUMBER N00014-92-J-1477	
9. SPONSORING/MONITORING AGENCY NAMES(S) AND ADDRESS(ES) Sponsoring: ONR, 800 N. Quincy, Arlington, VA 22217-5660 Monitoring: Administrative Contracting Officer, Office of Naval Research Regional Office Atlanta, 101 Marietta Tower, Suite 2805 101 Marietta Street Atlanta, GA 30323-6145			10. SPONSORING/MONITORING AGENCY REPORT NUMBER	
11. SUPPLEMENTARY NOTES				
12a. DISTRIBUTION/AVAILABILITY STATEMENT Approved for Public Release; Distribution Unlimited			12b. DISTRIBUTION CODE	
13. ABSTRACT (Maximum 200 words) Page 2 of 2 doping of GaN was achieved with doping levels of 5×10^{16} - 3×10^{18} cm ⁻³ . Growth of GaN in H ₂ and N ₂ was accomplished with the two main differences being stronger PL intensity and slower growth rate for the films grown in N ₂ . Biaxial strains resulting from mismatches in thermal expansion coefficients and lattice parameters in 22 GaN films grown on AlN buffer layers previously deposited on vicinal and on-axis 6H-SiC(0001) substrates were measured via changes in the c-axis lattice parameter. A Poisson's ratio of $n=0.18$ was calculated. The shift in the bound exciton energy with film stress was 23 meV/GPa. As-deposited Pt contacts on Mg-doped, p-type GaN showed ohmic behavior with $r_c = 0.46$ W-cm ² . Values of r_c increased upon annealing to a maximum of 8.11×10^3 W-cm ² at 700°C due to significant intermixing of Pt, Ga, N, and Mg, as revealed by SIMS analysis. As-deposited, 50 and 100 µm dia. Pt Schottky contacts on Si-doped, n-type GaN, possessed barrier heights of 1.36 and 1.28 eV, respectively. The ideality factor for both diameters was 1.13. Leakage currents <1 nA at -10V reverse bias were achieved. A new inductively coupled plasma (ICP) system has been designed, fabricated and initially tested. Parametric studies involving process gas flow rates, ICP and RF bias power and pressure to optimize the system for fast etch rates with the least surface damage/contamination are ongoing. Films of GaN were ion implanted with Si, Mg and Ca/P at energies of 160 keV (Si), 120 keV (Mg), and 180 keV/130 keV (Ca/P). The dose varied from 1×10^{14} cm ⁻² to 1×10^{15} cm ⁻² for Si and Mg and from 5×10^{14} cm ⁻² to 5×10^{15} cm ⁻² for Ca/P. Samples were implanted at 25°C (RT) and 550°C. Electrical activation has not been observed after repeated annealing. Analysis via RBS showed little or no damage compared to a virgin sample; however no PL spectra were observed in the implanted samples. TEM and HRTEM show regions of damaged located near the surface of the film in as-implanted and in samples annealed one min at 700 and 900°C. Laterally orientated, n-type GaN MIS capacitors have been fabricated using silicon oxide deposited via low temperature and remote plasma-enhanced CVD processes. Substantial leakage currents were measured in the former but much reduced in the latter.				
14. SUBJECT TERMS microscopy, photoluminescence, InGaN, doping, nitrogen, biaxial strain, thermal expansion coefficient, lattice parameter, Poisson's ratio, bound exciton energy, ohmic contacts, Schottky contacts, barrier height, ideality factor, leakage current, inductively coupled plasma, ion implantation, damage, low temperature CVD, remote plasma-enhanced CVD, MIS capacitors			15. NUMBER OF PAGES 97	
			16. PRICE CODE	
17. SECURITY CLASSIFICATION OF REPORT UNCLAS	18. SECURITY CLASSIFICATION OF THIS PAGE UNCLAS	19. SECURITY CLASSIFICATION OF ABSTRACT UNCLAS	20. LIMITATION OF ABSTRACT SAR	

Table of Contents

I. Introduction	1
Carbon-based Materials	
II. Interface Effects on Field Emitted Electrons from Diamond Coated Molybdenum Emitters <i>M. T. McClure, R. Schlessner, and Z. Sitar</i>	3
III. Characterization of Metal-Diamond Interfaces: Electron Affinity and Schottky Barrier Height <i>P. K. Baumann, S. P. Bozeman, B. L. Ward, and R. J. Nemanich</i>	12
IV. Dry <i>Ex Situ</i> Cleaning Processes for (0001) _{Si} 6H-SiC Surfaces <i>S. W. King and R. F. Davis</i>	19
Nitrogen-based Materials	
V. Growth of Bulk AlN and GaN Single Crystals by Sublimation <i>C. M. Balkas, Z. Sitar, T. Zheleva, L. Bergman, R. Nemanich and R. F. Davis</i>	30
VI. Growth of III-V Nitride Thin Films on α (6H)-SiC(0001) Via Organometallic Vapor Phase Epitaxy <i>D. Hanser and R. F. Davis</i>	38
VII. Correlation of Biaxial Strains, Bound Exciton Energies, and Defect Microstructures in GaN Films Grown on AlN/6H-SiC(0001) Substrates <i>W. G. Perry and R. F. Davis</i>	46
VIII. Ohmic Contact Formation on p-type GaN <i>L. Smith and R. F. Davis</i>	62
IX. Schottky Barriers on GaN <i>K. M. Tracy and R. F. Davis</i>	71
X. Dry Etching of Gallium Nitride <i>S. Smith and R. F. Davis</i>	77
XI. Ion Implantation, Annealing and Microstructural Investigations in GaN Thin Films <i>E. Carlson, D. Bray and R. F. Davis</i>	83
XII. III-V Nitrides for Use in Semiconductor Microelectronic Device Applications <i>R. Therrien and R. F. Davis</i>	92
XIII. Distribution List	97

I. Introduction

Heteroepitaxy is the growth of a crystal (or a film) on a foreign crystalline substrate that determines its orientation. Such oriented growth requires that lattice planes in both materials have similar structure. In general, an epitaxial relationship is probable whenever the orientation of the substrate and overgrowth produces an interface with a highly coincident atomic structure having low interfacial energy relative to a random arrangement.

During the past decade, nonequilibrium techniques have been developed for the growth of epitaxial semiconductors, superconductors, insulators and metals which have led to new classes of artificially structured materials. In many cases, the films were deposited on substrates having a different chemistry from that of the film, and heteroepitaxy was achieved. Moreover, layered structures with a periodicity of a few atomic layers have also been produced by the sequential heteroepitaxial deposition of a film of one type on another. Metastable structures can be generated which possess important properties not present in equilibrium systems. A consideration of the materials under consideration for next generation electronic and optoelectronic devices, e.g., the III-V nitrides show that only a few of them can currently be grown in bulk, single crystal form having a cross-sectional area of $>3\text{cm}^2$. Thus, other commercially available substrates must be used. This introduces a new set of challenges for the successful growth of device quality films which are not present in homoepitaxial growth and which must be surmounted if these materials are to be utilized in device structures.

In addition to providing structures which do not exist in nature, applications of advanced heteroepitaxial techniques permit the growth of extremely high-quality heterostructures involving semiconductors, metals, and insulators. These heterostructures offer the opportunity to study relationships between the atomic structure and the electrical properties of both the film itself and the interface between the two dissimilar materials. They also allow the study of epitaxial growth between materials exhibiting very different types (ionic, covalent, or metallic) of bonding.

While the potential of heteroepitaxial deposition has been demonstrated, significant advances in theoretical understanding, experimental growth and control of this growth, and characterization are required to exploit the capabilities of this process route. It is particularly important to understand and control the principal processes which control heteroepitaxy at the atomic level. It is this type of research, as well as the chemistry of dry etching via laser and plasma processing, which forms the basis of the research in this grant.

The materials of concern in this report are classified as wide bandgap semiconductors and include diamond, SiC and the III-V nitrides of Al, Ga, and In and their alloys. The extremes in electronic and thermal properties of diamond and SiC allow the types and numbers of current and conceivable applications of these materials to be substantial. However, a principal driving force for the interest in the III-V nitrides is their potential for solid-state optoelectronic devices

for light emission and detection from the visible through the far ultraviolet range of the spectrum.

The principal objectives of the research program are the determination of (1) the fundamental physical and chemical processes ongoing at the substrate surface and substrate/film interface during the heteroepitaxial deposition of both monocrystalline films of the materials noted above, as well as metal contacts on these materials, (2) the mode of nucleation and growth of the materials noted in (1) on selected substrates and on each other in the fabrication of multilayer heterostructures, (3) the resulting properties of the individual films and the layered structures and the effect of interfacial defects on these properties, (4) the development and use of theoretical concepts relevant to the research in objectives (1-3) to assist in the fabrication of improved films and structures and (5) the determination of process chemistry which leads to the laser assisted and plasma etching of these wide bandgap compound semiconductors.

This is the ninth bi-annual report since the initiation of the project. The following sections introduce each topic, detail the experimental approaches, report the latest results and provide a discussion and conclusion for each subject. Each major section is self-contained with its own figures, tables and references.

Carbon-based Materials

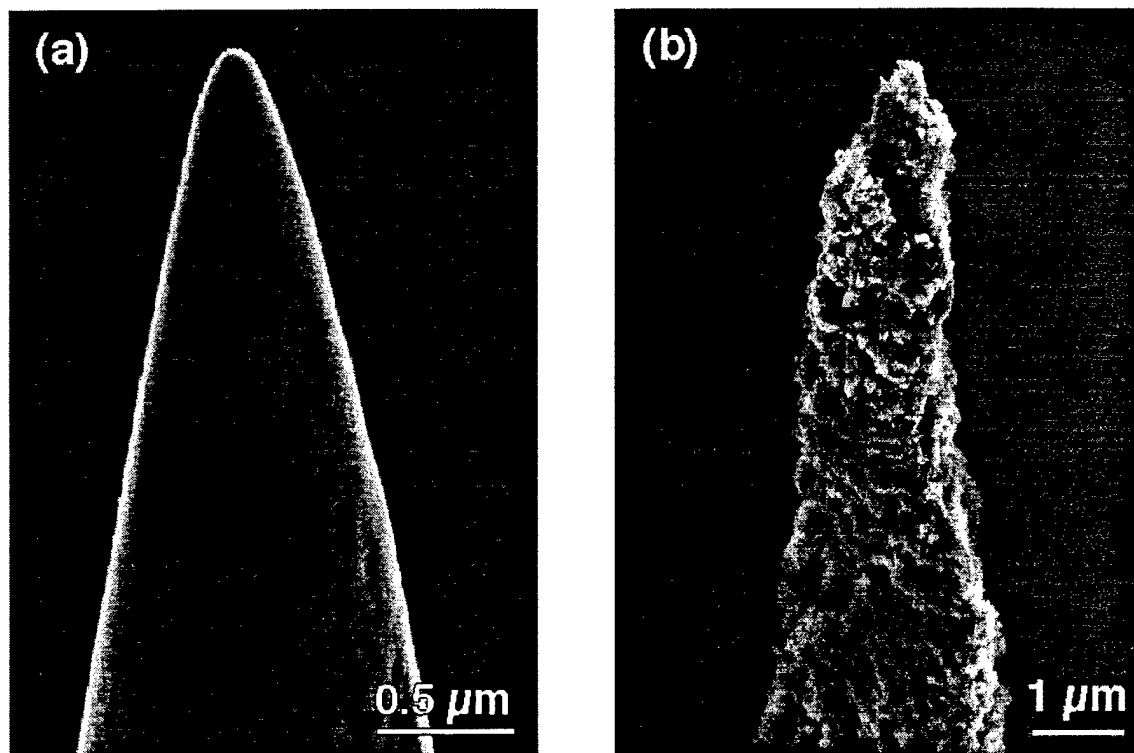
II. Interface Effects on Field Emitted Electrons from Diamond Coated Molybdenum Emitters

A. Introduction

Envisioned vacuum microelectronic devices, such as flat panel displays and ion sources, have stimulated research of microstructured field emitters. In the late '60s, Mo-based field emitters were first demonstrated [1] and Mo continues to be a standard emitter material. However, to meet the requirements of potential applications, lowering the operating voltage is necessary to improve long term stability. Field emission is a surface sensitive process; typical surface degradation problems include oxide formation and backspitting of self-generated ions [2]. Addressing this problem has led to investigation of diamond coatings as protective overlayers. Diamond has attractive thermal and mechanical properties to dissipate heat and remain inert in a variety of environments. Additionally, diamond has superlative electronic properties (e.g., high breakdown voltage and NEA behavior on H-terminated (111) [3] and (100) [4] surfaces) that have been shown to enhance the emission current [5]. Despite the beneficial aspects of diamond coatings, the presence of an additional interface (i.e., the Mo/diamond interface) adds complexity to the emission process. Thus, investigating the influence of this interface is necessary for comprehension of the electron emission process through diamond overlayers. A study of diamond-coated Mo emitters before and after annealing procedures was undertaken to investigate the influence of the Mo/diamond interface on the emission process.

B. Experimental

Single Mo emitter tips were made from Mo wire (diameter: 0.125 mm) and were sharpened by electrochemical etching in a concentrated KOH solution (applied voltage: 10 V DC, counterelectrode: Pt). Typical radii of curvature of the sharpened Mo tips were less than 100 nm. diamond coatings were deposited subsequently by a dielectrophoretic procedure, which consisted of dipping a positively biased (ca. 10 V) Mo tip into an ultrasonically prepared suspension of diamond powder (typical particle size: 100 nm) in ethanol. Due to dipolar interaction with the nonuniform external electric field, the electrostatically neutral, suspended diamond particles moved toward regions of higher field strength and were thus deposited on the Mo tip. Careful timing of the coating procedure allowed deposition of diamond layers with a thickness of a few hundred nanometers, see Fig. 1. The diamond powder used was nominally undoped; Raman spectroscopy of the diamond powder evidenced no Raman active defects. The shape of the pure Mo tips, as well as the thickness and uniformity of the dielectrophoretic coatings, was monitored by scanning electron microscopy (SEM), before and after the FEED experiments.



(a) SEM of etched, uncoated Mo tip

(b) SEM of diamond-coated Mo tip.

Figure 1. (a) SEM micrographs of the electrochemically etched Mo wire and (b) after dielectrophoresis diamond powder coating.

Field emission energy distribution (FEED) experiments were carried out using a test device that consisted of a tip holder facing an electrically insulated, metallic gate with a circular opening (diameter: 500 μm), see Fig. 2. A tip was mounted at a distance of 500 μm from the gate, and was aligned with the gate opening using a stereo-microscope. Measurements were performed in a UHV analysis chamber (pressure: 10^{-9} Torr), where the test device was aligned with the entrance lens system of a hemispherical electron analyzer (VG Instruments CLAM II) used to record the energy distribution of the field emitted electrons that passed through the gate opening. The gate was kept at ground potential, while a negative bias voltage was applied to the tip.

The emitters underwent different annealing cycles to investigate potential annealing effects occurring at the diamond/Mo interface. The uncoated Mo emitter was heated in vacuum (10^{-7} Torr) to 550°C for 1 hour before FEED spectra were taken. After coating with diamond powder, the emitter was heated to 350°C in vacuum for 1 hour to remove any solvent and atmospheric contamination. After a first series of FEED measurements, the coated emitter was heated in a second heating cycle to 450°C for 45 minutes and an additional series of FEED spectra was recorded. All FEED spectra were taken from samples at room temperature.

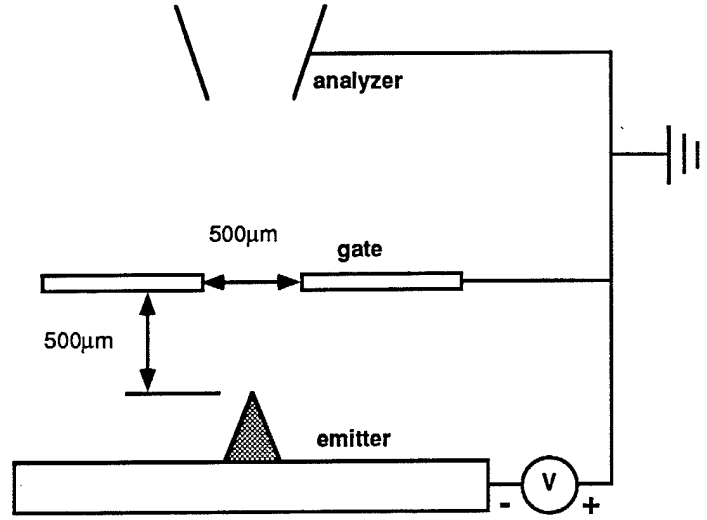


Figure 2. Schematic drawing of the FEED test device and circuit diagram.

C. Results and Discussion

Field Emission Energy Distribution from Mo Tips. Before studying diamond coated emitters, analysis of the uncoated Mo emitter was necessary to quantify certain field emission parameters. First, FEED spectra were taken from uncoated Mo tips, after *in vacuo* desorption at 550°C for 1h. Figure 3 shows a typical FEED spectrum obtained from a bare Mo tip. The count rate is proportional to the field emission current j . The (kinetic) energy scale, $(E - E_{f,Mo})$, is referenced to the kinetic energy of field emitted electrons from the Fermi level of Mo, $E_{f,Mo}$:

$$(E - E_{f,Mo}) = E - (V_o - \Phi_A). \quad (1)$$

V_o denotes the potential applied between the gate (+) and tip (-), and E the measured kinetic energy of the emitted electrons. The work function of the analyzer, $\Phi_A = 4.3$ eV, was calibrated by X-ray photoelectron spectroscopy (Mg-anode) of a Cu sample, where the positions of the $2p_{1/2}$ and $2p_{3/2}$ peaks were taken as energy references.

The description of the field emission energy distribution j based on the free electron model for metals is given by [6]:

$$j = \frac{e\pi(2m)^{1/2} f(E - E_{f,Mo})}{\hbar^3 (\Phi_{Mo} - (E - E_{f,Mo}))^{1/2}} \exp\left(-\frac{4}{3} \left(\frac{2m}{\hbar^2}\right)^{1/2} \frac{(\Phi_{Mo} - (E - E_{f,Mo}))^{3/2}}{eF}\right), \quad (2)$$

where e and m denote the charge and mass of the electron, respectively, F is the electric field at the emission site, and Φ_{Mo} is the work function of the Mo tip. The Fermi-Dirac distribution at a temperature T is given by

$$f(E - E_{f,Mo}) = (1 + \exp(E - E_{f,Mo})/kT)^{-1}. \quad (3)$$

T was set to 300K for the analysis of the experiments reported here. Taking into account the finite resolution of the electron spectrometer, modeled by a Gaussian instrument function

$$i(E) \sim \exp(-4 \ln^2(E/\Delta E_{FWHM})^2), \quad (4)$$

the experimental data were fitted to the convolution $j(E - E_{f,Mo}) \otimes i(E - E_{f,Mo})$. Fit parameters were the field enhancement factor, $\beta = F/V_o$, the full width at half maximum of the instrument function, ΔE_{FWHM} , as well as a factor linking the observed count rates to the calculated field emission current j . This factor took into account that a portion of the emitted electron current did not pass through the gate, and that the electron analyzer captured only part of the angular distribution of the emitted beam. The work function of Mo, $\Phi_{Mo} = 4.3$ eV, was taken from the literature [5].

Field emission energy distribution data collected from several Mo tips at applied voltages in a range from 500 to 900 V consistently yielded field enhancement factors in the order of $\beta \approx 10^5 \text{ cm}^{-1}$, which is in good agreement with previous I - V characterization data of similar tips [6]. The width of the analyzer instrument function was determined to be $\Delta E_{FWHM} = (0.47 \pm 0.06)$ eV at an analyzer pass energy of 20 eV. Determination of the field enhancement factor, β , was necessary for analysis of the diamond coated Mo emitter.

Field Emission Energy Distribution from Diamond Coated Mo Tips. Having characterized the uncoated Mo tip, the same tip was coated with diamond powder and the emission behavior was examined. In particular, the energy position of the peak ($E - E_{f,Mo}$) was determined as a

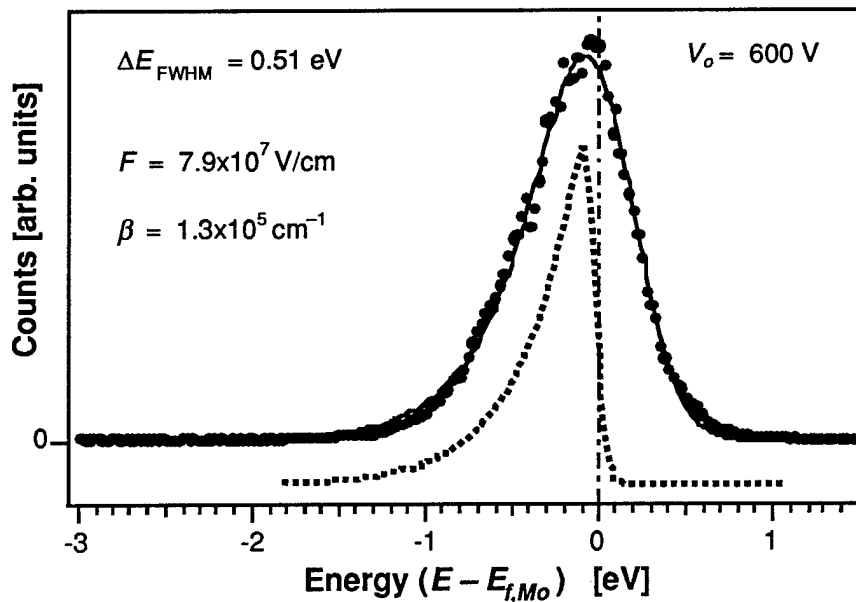


Figure 3. FEED spectrum from bare Mo emitter and theoretical spectrum (dashed line) based on the free electron model.

function of applied voltage. The set of emitters studied produced two typical emission behaviors: (i) before annealing: an exponential deviation of peak position ($E - E_{f,Mo}$) with increasing applied voltage, V_0 , and (ii) after annealing: a linear deviation of peak position with increasing applied voltage, see Fig. 4.

The nonlinear response of peak position ($E - E_{f,Mo}$) versus voltage can be understood by considering a “poor” contact between the diamond powder and the Mo emitter so that the surface of the diamond particle became electrostatically charged during the field emission process. To consider this case, the applied voltage was converted to a calculated Fowler-Nordheim (FN) current using Eqn. (a) below [7]:

$$j = \frac{e^3 F^2}{8\pi h \Phi t^2(y)} \exp \left[\frac{8\pi(2m)^{1/2} \Phi^{3/2}}{3heF} v(y) \right], \quad (a)$$

where $t^2(y)$ and $v(y)$ are the Nordheim elliptic functions. Based on the analysis of the emission spectra from the uncoated Mo emitter, the field enhancement factor was used to convert the applied voltage to the electric field ($F = \beta V_0$). The peak position ($E - E_{f,Mo}$) was then plotted versus the calculated FN current (see Fig. 5) and displayed a linear correlation. This behavior suggests that the emission current would create a surface charge to the diamond powder so that emitted electrons lost kinetic energy overcoming this additional electrostatic potential. The fact that the observed peak shifts depended linearly on current rather than applied voltage strongly suggests that the dynamic equilibrium between charge injection from Mo and field emission into vacuum created the mentioned electrostatic potential and that a poor contact between Mo and diamond limited charged transport toward the emitting surface.

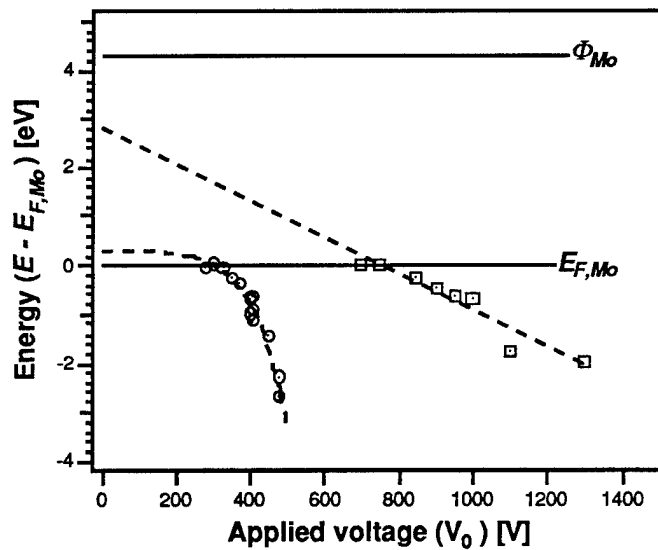


Figure 4. Emission response, peak position ($E - E_{f,Mo}$) vs. applied voltage, from a non-annealed (trace a) and an annealed (trace b) diamond coated Mo emitter.

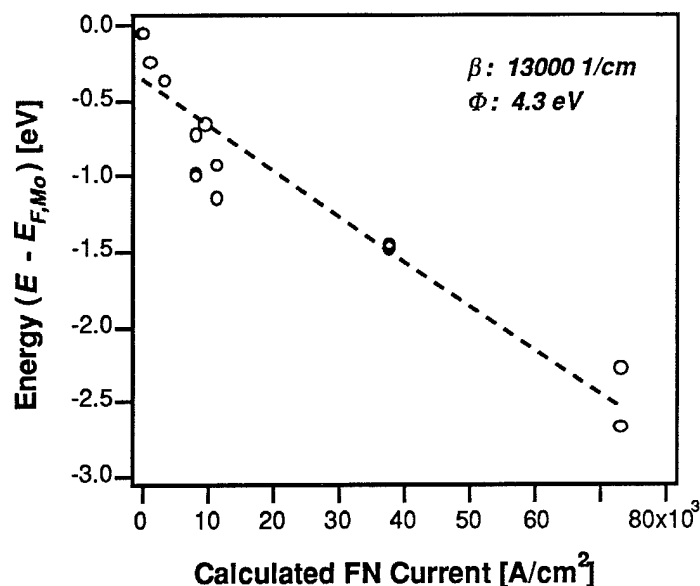


Figure 5. Emission response of the non-annealed diamond coated Mo emitter plotted as peak position ($E - E_{f,Mo}$) versus calculated Fowler-Nordheim current according to Eqn. (2) ($F = \beta V_0$). The peak position has a linear correlation with the calculated current.

The annealing temperature was chosen to promote the formation of a carbide layer between the Mo emitter and the diamond coating. Previously reported data revealed that annealing temperatures greater than 430°C were sufficient to create an interfacial carbide layer for refractory metals [8] and electron diffraction patterns revealing a Mo_2C layer after annealing for other Mo/diamond emitters has been observed [9]. The formation of an interfacial carbide would improve the physical contact between the Mo emitter and the diamond powder, make the contact more ohmic in behavior [8], and eliminate the electrostatic charging effects seen prior to annealing and allow field penetration of the diamond. After annealing, the FEED spectra displayed the second type of emission response. This emission response described a linear increase in peak position ($E - E_{f,Mo}$) with increasing applied voltage (V_0) (Fig. 4, trace b) appeared after annealing. Peak shifts of the same order of magnitude have been reported earlier in the case of chemical vapor deposited diamond on Mo substrates [10]. The observed linear decrease in kinetic energy with the applied voltage can be explained by a model taking into account the voltage drop across the dielectric diamond coating, see Fig. 6.

As has been discussed in the literature [11, 12], electrons are injected from the Fermi level $E_{f,Mo}$ of the Mo tip into the conduction band of diamond, where they settle down close to the conduction band minimum (CBM). The observed emission originates from the diamond/vacuum interface, where the CBM is lowered by a voltage drop ΔV , proportional to the applied voltage V_0 and the thickness of the layer, and inversely proportional to the dielectric

constant ϵ of the layer material. The kinetic energy of the emitted electrons, E , is given in this case by (see Fig. 6):

$$(E - E_{f,Mo}) = (\Phi_{Mo} - \chi_{dia}) - \Delta V, \quad (5)$$

where χ_{dia} is the electron affinity of diamond. Extrapolation of the data shown in Fig. 4 toward $V_o = 0$, where ΔV vanishes, yields $(\Phi_{Mo} - \chi_{dia}) = (3 \pm 0.3)$ eV, indicating, within the experimental accuracy and the limits of this model, a small positive electron affinity of diamond in the order of 1 eV. The fact that no emission was observed at voltages $V_o < 400$ V confirms that the CBM of diamond has to be lowered by field penetration in order to enable injection of electrons from Mo into the conduction band of diamond. As has been reported recently [11], the injection mechanism at the Mo/diamond interface may be the dominant current limiting factor, since, due to the low electron affinity of diamond, its surface potential barrier is lower than that at the Mo/diamond interface. The minor peak broadening with applied voltage indicates a fast thermalization process of the injected electrons to the bottom of the conduction band.

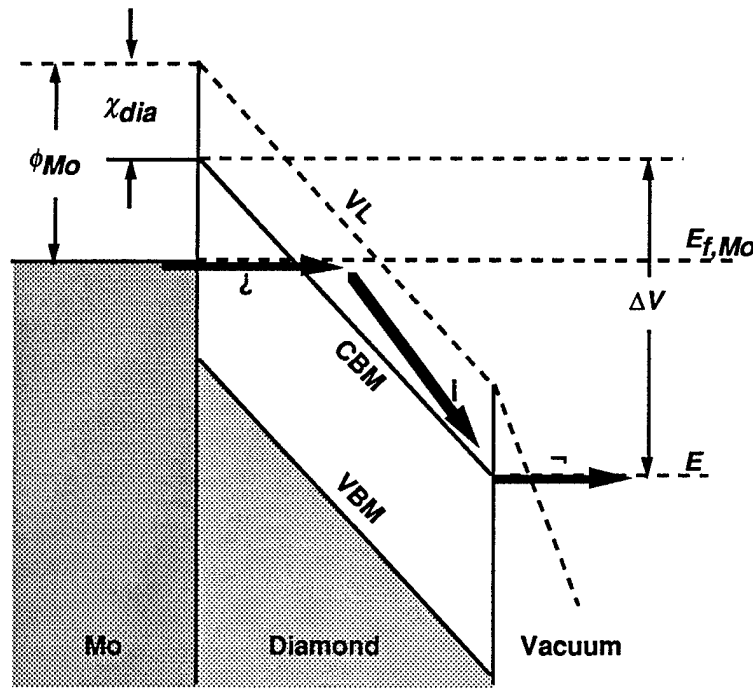


Figure 6. Simplified band diagram illustrating the field emission mechanism from a diamond coated Mo emitter. Electrons are injected (1) from the Mo/diamond interface ($E_{f,Mo}$: Fermi level of the Mo tip) into the conduction band of diamond, where they settle down (2) to the conduction band minimum (CBM). Field emission (3) takes place from the conduction band minimum at the diamond/vacuum interface at an energy E . Lowering of the CBM at the emission site is due to a voltage drop ΔV across the dielectric diamond layer and is proportional to the applied voltage.

In contrast to recently published FEED data [13] obtained from a natural *p*-type diamond sample, there was no observation of any field emission from the valence band maximum (VBM) in the case of nominally undoped diamond powder. Presumably a sufficiently large hole conductivity is a mandatory requirement to obtain considerable valence band field emission.

D. Conclusions

In conclusion, a test apparatus has been assembled and tested for analyzing the field emission energy distribution from microtip emitters. Initially, a Mo emitter was analyzed and characterized using a theoretical energy distribution based on the free electron model. The spectrometer broadening function was included in the computer model. After analyzing the uncoated Mo emitter, a dielectrophoresis procedure was used to apply a diamond powder coating. The affect of interfacial contact between the Mo emitter and the diamond coating was studied after two annealing cycles. Based on the FEED spectra collected, two field emission responses have been characterized from diamond coated Mo emitters. The first response showed a linear dependence of the energy position ($E - E_{F,Mo}$) of the spectrum with the calculated Fowler-Nordheim current from emitter structures that were not annealed. A model was developed based on "poor" contact between the diamond powder and the Mo emitter whereby the emission from Mo adds a surface charge on the diamond powder. After annealing the emission response showed a linear dependence of the energy position ($E - E_{F,Mo}$) of the spectrum with the applied voltage (V_0). Based on this behavior a simple model was developed based on emission from the conduction band minimum of diamond at the diamond/vacuum interface. The effect of the annealing process was the formation of an interfacial carbide that facilitated the injection of electrons from Mo into the conduction band of diamond.

E. Future Work

Future investigations will address the emission characteristics of other wide band gap dielectrics, particularly cubic BN, and continue to investigate the role of the molybdenum carbide in the emission process.

F. References

1. C. A. Spindt, J. Appl. Phys. **39** (7), 3504 (1968).
2. R. Smith, J. Phys. **D 17** (5), 1045 (1984).
3. F. J. Himpsel, J. A. Knapp, J. A. Van Vechten and D. E. Eastman, Phys. Rev. B **20** (2), 624 (1979).
4. J. van der Weide, Z. Zhang, P. K. Baumann, M. G. Wensell, J. Bernholc and R. J. Nemanich, Phys. Rev. B **50** (8), 5803 (1994).
5. G. A. Haas, in *American Institute of Physics Handbook*, edited by D. W. Gray (McGraw-Hill, New York, 1972).

6. W. B. Choi, J. Liu, M. T. McClure, A. F. Myers, V. V. Zhirnov, J. J. Cuomo and J. J. Hren, *J. Vac. Sci. Technol.* **B 14** (3), 2050 (1996).
7. I. Brodie and C. A. Spindt, *Adv. Electron. Electron Phys.* **83**, 1 (1992).
8. T. Tachibana, B. E. Williams and J. T. Glass, *Phys. Rev. B.* **45** (20), 11975 (1992).
9. W. B. Choi, A. F. Myers, G. J. Wojak, M. T. McClure, J. J. Cuomo and J. J. Hren, "The effects of the interface and surface treatment on the electron emission from diamond coated field emitters" in *Proceedings of 9th International Vacuum Microelectronics Conference*, Saint-Petersburg, Russia, p. 288.
10. N. S. Xu, Y. Tzeng and R. V. Latham, *J. Phys. D* **27** (9), 1988 (1994).
11. M. W. Geis, J. C. Twichell, N. N. Efremov, K. Krohn and T. M. Lyszczarz, *Appl. Phys. Lett.* **68** (16), 2294 (1996).
12. E. I. Givargizov, V. V. Zhirnov, A. N. Stepanova, E. V. Rakova, A. N. Kiselev and P. S. Plekhanov, *Appl. Surf. Sci.* **87/88**, 24 (1995).
13. C. Bandis and B. B. Pate, *Appl. Phys. Lett.* **69** (3), 366 (1996).

III. Characterization of Metal-Diamond Interfaces: Electron Affinity and Schottky Barrier Height

A. Introduction

Negative electron affinity (NEA) surfaces based on wide band gap semiconductors such as diamond may be important for the development of cold cathode devices. However, n-type doping of diamond still poses a major challenge. The electron affinity of a semiconductor is defined as the energy difference between the vacuum level and the conduction band minimum. For most materials, the vacuum level lies above the conduction band minimum, corresponding to a positive electron affinity. Surfaces of wide band gap semiconductors such as diamond have the potential of exhibiting a NEA since the conduction band minimum lies near the vacuum level. For a NEA surface, the electrons from the conduction band minimum have sufficient energy to overcome the surface potential and can be emitted into vacuum.

Various surface treatments such as plasma cleaning, as well as annealing in ultra high vacuum (UHV), can shift the position of the vacuum level and, therefore, induce a NEA or remove it [1-6]. Pre-cleaning the diamond (100) samples with a wet chemical etch results in an oxygen termination of the surface. This chemisorbed oxygen layer forms a surface dipole that results in an increase in the surface workfunction. It is found that such a surface exhibits a positive electron affinity. Annealing these samples to 900°C–1050°C or exposing them to a H-plasma results in the removal of oxygen from the surface, a 2×1 reconstruction and a NEA [3, 5, 6]. The different threshold temperatures are related to different wet chemical pre-treatments [3]. It was found that 900°C was sufficient for samples pre-cleaned by an electrochemical etch. But 1050°C was required for a pre-clean employing chromic acid. The diamond (100) surface has been proposed to exhibit a monohydride termination subsequent to a 900°C–1050°C anneal or a H-plasma exposure. An H surface layer results in a dipole such that the work function is reduced, resulting in a NEA. Heating these samples to 1150°C resulted in a 2×1 reconstructed surface with a positive electron affinity [6]. This surface has been suggested to be free of adsorbates. In agreement with the experimental results, *ab initio* calculations for the 2×1 reconstructed surface predict a NEA for a monohydride terminated surface and a positive electron affinity for an adsorbate free surface [5].

Furthermore, it has been demonstrated that metals like Ti, Ni Co, Cu and Zr can induce a NEA on diamond surfaces [7-11]. In addition, no significant dependence of the Schottky barrier height on the metal work function has been found [3, 7-12]. Metal films deposited on adsorbate-free surfaces tend to result in lower Schottky barrier heights and lower electron affinities than for surfaces terminated by species such as hydrogen or oxygen [8, 9]. Photoemission spectroscopy is found to be a very sensitive method to determine whether a surface exhibits a NEA or not. Electrons get photoexcited from the valence band into states in

the conduction band and can quasi-thermalize to the conduction band minimum. Secondary electrons from the conduction band minimum appear as a sharp peak at the low kinetic energy end of photoemission spectra for NEA surfaces [13, 14].

Photoemission spectroscopy determines the emission properties of the surface itself. In comparison field emission data reflect a combination of carrier injection, transport and emission processes. In this study, diamond (100) surfaces have been cleaned by anneals to 1050°C or 500°C. Thin Cu or Zr films were deposited on these diamond substrates. The surface properties were characterized before and after metal deposition.

B. Experimental Details

The UHV system used in this study consists of several interconnected chambers including systems used for annealing, metal deposition, UPS and AES. Natural type IIb single crystal diamond (100) substrates ($3.0 \times 3.0 \times 0.25$ mm) were used. The samples were electrochemically etched to remove non-diamond carbon and metal contaminants [15]. This etch included applying a DC bias of 350V between two Pt electrodes that were placed in deionized (DI) water as an electrolyte. The samples were suspended in water between the two electrodes. Following the electrochemical etch, a HF dip was employed to remove SiO_2 from the surface [3]. The wafers were then mounted on a Mo holder and transferred into the UHV system (base pressure $\sim 1 \times 10^{-10}$ Torr). As an *in vacuo* cleaning step, the wafers were annealed to 1150°C or 500°C for 10 minutes. This caused the pressure to rise to $\sim 7 \times 10^{-9}$ Torr. Subsequent to annealing, 2 Å thick films of Cu or Zr were deposited by means of e-beam evaporation. The thickness of the metal layers was determined by a quartz crystal oscillator. During deposition, the pressure rose to $\sim 2 \times 10^{-9}$ Torr. Following the annealing and the growth steps, UPS and AES were employed to analyze the surface properties.

The presence of a Cu or Zr film was confirmed by using AES. AFM images of the diamond wafers clearly showed arrays of linear groves parallel to each other with a depth of ~ 20 Å. This surface structure is due to the commercial polishing of the samples. No island structures were observed in AFM measurements after 2 Å of deposition, which may be indicative of a uniform 2D layer for both Cu and Zr.

HeI (21.21 eV) radiation was used to excite the photoemission of electrons. A 50 mm hemispherical analyzer was employed to measure the emitted electrons with an energy resolution of 0.15 eV. A bias of 1V was applied to the sample to overcome the workfunction of the analyzer and, thus, to detect the low energy electrons emitted from the NEA surface. The position of the sharp NEA peak at the low energy end of photoemission spectra corresponds to the energy position of the conduction band minimum, E_c . Emission from E_c is positioned at $E_v + E_g$ in the spectrum, where E_v is the energy of the valence band maximum and E_g that of the bandgap. Emission from the valence band maximum appears at $E_v + h\nu$ in the

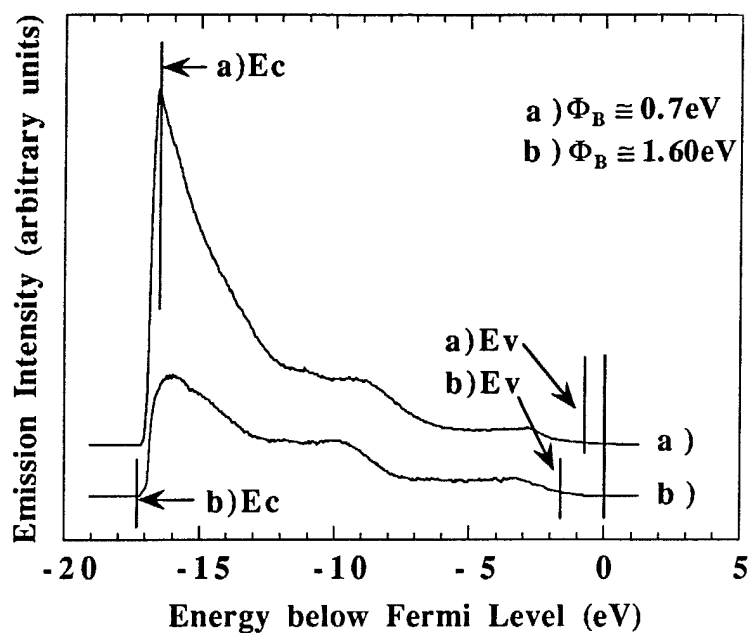


Figure 1. UV photoemission spectra of 2 Å of Cu grown on a diamond (100) surface following an anneal to a) 1150°C b) 500°C. A metal induced NEA is observed for a) whereas a positive electron affinity is detected for b).

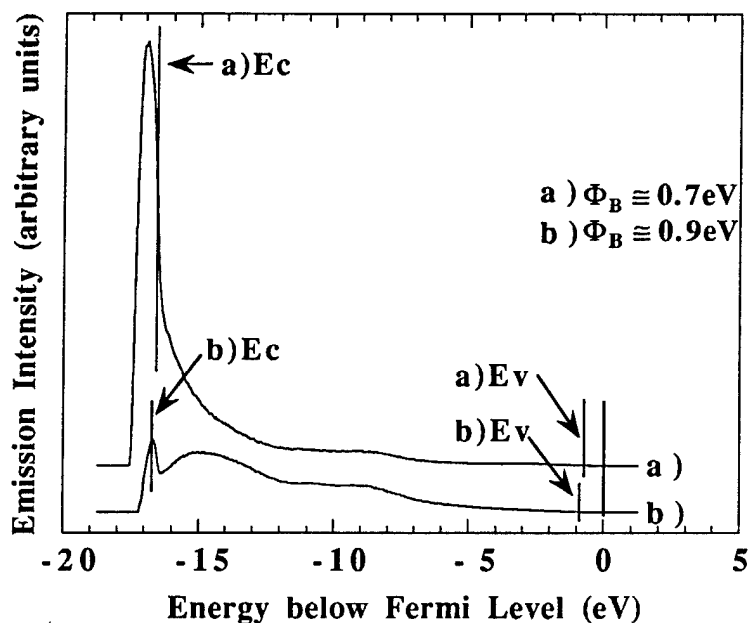


Figure 2. UV photoemission spectra of 2 Å of Zr deposited on a diamond (100) surface annealed to a) 1150°C b) 500°C. Metal induced NEA's are observed upon deposition of Zr for both a) and b). For a) emission below E_C is detected.

Table I. Results of Electron Emission Measurements

Sample	UPS	Field Emission Threshold (V/ μm)	Barrier Height (eV)
C(100)	after 500°C anneal PEA, $\chi \cong 1.4$ eV	79 ± 7	0.23 ± 0.01
Cu/C(100) clean	NEA, $\chi < 0$, $\Phi_B \cong 0.70$ eV	25 ± 3	0.10 ± 0.01
Cu/C(100) oxygen	PEA, $\chi \cong 0.75$ eV, $\Phi_B \cong 1.60$ eV	53 ± 4	0.21 ± 0.01
Zr/C(100) clean	NEA, $\chi < 0$, $\Phi_B \cong 0.7$ eV	20 ± 3	0.09 ± 0.01
Zr/C(100) oxygen	NEA, $\chi < 0$, $\Phi_B \cong 0.9$ eV	49 ± 4	0.20 ± 0.01

PEA: positive electron affinity, NEA: negative electron affinity. The averages and standard deviations of the field emission measurements at different distances are shown as the field emission threshold and the barrier height. The threshold current is 0.1 μA .

observed Schottky barrier heights electron affinities of $\chi \cong -0.72$ eV for the clean surface and $\chi \cong -0.52$ eV for the oxygen terminated surface are obtained. These results are in agreement with the NEA and positive electron affinity effects that were observed by means of UPS. The emission detected below E_c for Zr on the clean surface is consistent with the calculated value of $\chi \cong -0.72$ eV. The fact that no emission below E_c was observed for Zr on oxygen terminated diamond may be due to a different interface structure. It has been reported that carbon contaminants lower the workfunction of Ni [17]. The workfunction of the 2Å thick films in our study may be affected by the carbon of the diamond. But such an effect would only lead to a stronger NEA effect for Cu on the clean surface and both Zr on the clean and oxygenated surface and would be consistent with our results. For Cu on the oxygen-terminated surface, the measured and calculated values for the electron affinity are consistent with each other. Thus, at least for the latter case, this effect is not expected to be significant.

For systems like Ti or Ni layers on diamond (111) surfaces [7, 8] this simple workfunction model has been used successfully to explain NEA or positive electron affinity effects. It has been observed that Ni deposited on an adsorbate free (111) surface induced a NEA [8]. In comparison, a positive electron affinity and a larger Schottky barrier were obtained for thin Ni films on (111) surfaces terminated by hydrogen. In theoretical studies by Erwin and Pickett [18-21] and Pickett, Pederson and Erwin [22], it was reported that the most stable

configuration for Ni on clean (111) and (100) surfaces resulted in a Schottky barrier height of less than 0.1 eV. Regarding copper on diamond (111) surfaces, Lambrecht [23] obtained a value for the Schottky barrier height of less than 0.1 eV for clean surfaces and greater than 1.0 eV for hydrogen-terminated surfaces. According to these results, the interface termination appears to be crucial for the Schottky barrier height. For metals deposited on clean surfaces, lower values for the Schottky barrier height and a greater likelihood of inducing a NEA are expected than for metals on non adsorbate free surfaces. The Schottky barrier heights reported in this study for Cu and Zr on diamond are in agreement with this. Zr and Ti have a stronger affinity to C than is the case for Cu and Ni. This may play a role in the interface formation of the thin films on diamond. Both Zr or Ti on clean as well as oxygen-terminated diamond surfaces tend to exhibit lower electron affinities than Cu or Ni on corresponding surfaces. This can be determined from the results of this study, as well as previous reports [7, 8]. The workfunction of Ti is only 0.3 eV higher than that of Zr. Apparently the relatively small difference between Zr and Ti is sufficient to induce a NEA for Zr on the oxygen terminated surface but not for the case of Ti. It is significant that a metal induced NEA was observed for deposition of Zr on both clean and oxygen terminated surfaces. Prior to this work only low workfunction metals like Cs have been found to induce a NEA on non adsorbate free diamond surfaces [24].

Field emission measurements were performed on diamond samples and on Cu or Zr films deposited on clean and oxygen terminated diamond surfaces. For a current of 0.1 μA , values between 20 and 79 V/ μm were measured for the emission threshold field. A summary of the results is shown in Table I. Previous studies have reported comparable values for diamond samples [11, 25, 26]. As an example, I-V curves for the diamond surface are shown in Fig. 3. For comparison, one I-V curve for Zr on a clean diamond surface has been included also. These results have been compared to the Fowler–Nordheim equation [27]:

$$I = k \left(\frac{V}{d} \right)^2 \exp \left(\frac{-6530 d \phi^{3/2}}{V} \right). \quad (2)$$

I is the current in amps, V is the bias in volts, d is the distance between the sample and the anode in microns, k is a constant and ϕ is the effective barrier height in eV. The field enhancement factor has been neglected since the surfaces have been found to be essentially flat by means of AFM. The effective barrier heights ϕ were obtained by fitting the field emission data to Eq. 2 (see Table I). Depositing Cu or Zr onto both clean and oxygen-terminated diamond (100) surfaces improves the emission properties. The case of Zr on clean surfaces gave the best results. Both UPS and field emission measurements show these trends consistently.

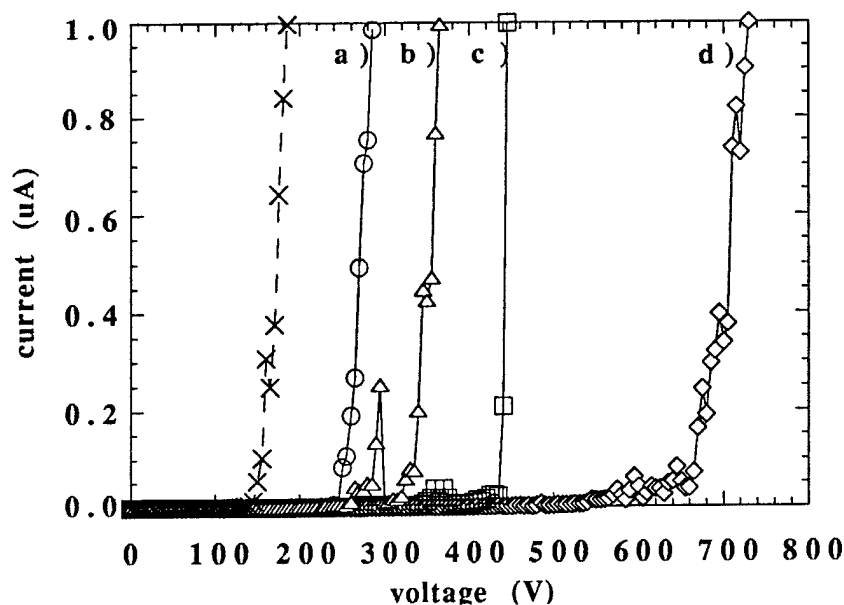


Figure 3. Field emission current-voltage curves for a type IIb single crystal diamond (100) sample. Distances between the sample and the anode: a) 3.3 μm , b) 4.3 μm , c) 5.6 μm , d) 8.5 μm . For comparison one current-voltage curve for Zr on a clean diamond (100) surface is also shown (dashed line) with a distance between the sample and the anode of 7.8 μm .

D. Conclusions

The effects of depositing thin metal films onto clean and oxygen terminated diamond (100) substrates has been studied by UPS. Cu only induced a NEA on clean surfaces. In comparison, Zr induced a NEA on both clean and oxygen terminated surfaces. Emission even below E_c was detected for Zr on clean surfaces. Both the field emission threshold and the effective barrier height were reduced in a manner consistent with the UPS results by depositing metals on diamond.

E. Future Work

Work in the future will involve the fabrication and characterization of electron injecting contacts. In addition, investigation of the electron emission mechanism is planned.

F. References

1. F. J. Himpsel, D. E. Eastman, P. Heimann and J. F. van der Veen, *Phys. Rev. B* **24**, 7270 (1981).
2. B. B. Pate, M. H. Hecht, C. Binns, I. Lindau and W. E. Spicer, *J. Vac. Sci. Technol.* **21**, 364 (1982).
3. P. K. Baumann, T. P. Humphreys and R. J. Nemanich, in *Diamond, SiC and Nitride Wide Bandgap Semiconductors*, edited by C. H. Carter, G. Gildenblat, S. Nakamura, R. J. Nemanich, (Mater. Res. Soc. Proc. **339**, Pittsburgh, PA, 1994) 69-74.
4. J. van der Weide and R. J. Nemanich, *Appl. Phys. Lett.* **62**, 1878 (1993).
5. J. van der Weide, Z. Zhang, P. K. Baumann, M. G. Wensell, J. Bernholc and R. J. Nemanich, *Phys. Rev. B* **50**, 5803 (1994).

6. P. K. Baumann and R. J. Nemanich, *Proc. of the 5th European Conference on Diamond, Diamond-like and Related Materials*, edited by P. K. Bachmann, I. M. Buckley-Golder, J. T. Glass, M. Kamo: *J. Diamond Rel. Mat.*, **4** (1995) 802.
7. J. van der Weide and R. J. Nemanich, *J. Vac. Sci. Technol. B* **10**, 1940 (1992).
8. J. van der Weide and R. J. Nemanich, *Phys. Rev. B*, **49**, 13629 (1994).
9. P. K. Baumann and R. J. Nemanich, *Appl. Surf. Sci.*, in press.
10. P. K. Baumann and R. J. Nemanich, in *Diamond for Electronic Applications*, edited by C. Beetz, A. Collins, K. Das, D. Dreifus, T. Humphreys, P. Pehrsson, (Mater. Res. Symp. Soc. Proc. **416**, Pittsburgh, PA 1996) 157-162.
11. P. K. Baumann, S. P. Bozeman, B. L. Ward and R. J. Nemanich in *III-Nitride, SiC, and Diamond Materials for Electronic Devices*, edited by C. Brandt, D. K. Gaskill, R. J. Nemanich, (Mater. Res. Soc. Proc., Pittsburgh, PA, 1996), in press.
12. P. K. Baumann, T. P. Humphreys, R. J. Nemanich, K. Ishibashi, N. R. Parikh, L. M. Porter and R. F. Davis, *Proc. of the 4th European Conference on Diamond, Diamond-like and Related Materials*, edited by P. K. Bachmann, I. M. Buckley-Golder, J. T. Glass, M. Kamo: *J. Diamond Rel. Mat.* **3** (1994) 883.
13. F. J. Himpsel, P. Heimann and D. E. Eastman, *Sol. State Commun.* **36**, 631 (1980).
14. B. B. Pate, W. E. Spicer, T. Ohta and I. Lindau, *J. Vac. Sci. Technol.* **17**, 1087 (1980).
15. M. Marchywka, P.E. Pehrsson, S.C. Binari and D. Moses, *J. Electrochem. Soc.*, **140**, (2), L19 (1993).
16. E. H. Rhoderick and R. H. Williams, *Metal-Semiconductor Contacts* Clarendon, Oxford, (1988).
17. C. Weiser, *Surf. Sci.* **20**, 143 (1970).
18. S. C. Erwin and W. E. Pickett, *Surf. Coat. Technol.* **47**, 487 (1991).
19. S. C. Erwin and W. E. Pickett, *Solid State Commun.* **81**, 891 (1992).
20. W. E. Pickett and S. C. Erwin, *Phys. Rev. B* **41**, 9756 (1990).
21. W. E. Pickett and S. C. Erwin, *Superlatt. Microstruct.* **7**, 335 (1990).
22. W. E. Pickett, M. R. Pederson and S. C. Erwin, *Mater. Sci. Eng. B* **14**, 87 (1992).
23. W. R. L. Lambrecht, *Physica B* **185**, 512 (1993).
24. M. W. Geis, J. C. Twichell, J. Macaulay, K. Okano, *Appl. Phys. Lett.* **67**, 1 (1995).
25. W. Zhu, G. P. Kockanski, S. Jin and L. Siebels, *J. Appl. Phys.*, in press.
26. S. P. Bozeman, P. K. Baumann, B. L. Ward, M. J. Powers, J. J. Cuomo, R. J. Nemanich and D. L. Dreifus, *Proc. of the 6th European Conference on Diamond, Diamond-like and Related Materials*, edited by P. K. Bachmann, I. M. Buckley-Golder, J. T. Glass, M. Kamo: *J. Diamond Rel. Mat.* (1996), 802.
27. R. Gomer, *Field Emission and Field Ionization*, Cambridge, MA, (1961).

IV. Dry *Ex Situ* Cleaning Processes for (0001)_{Si} 6H-SiC Surfaces

A. Introduction

For SiC to succeed as the semiconductor/substrate of choice for high frequency/high temperature, high power devices and III-N heteroepitaxy, a considerable reduction in defects (line, planar, point, etc.) must be achieved. Following Si technology, where surface cleaning and preparation are critical first steps in all processes [1], a continued reduction in defects in SiC should be expected as a result of improved SiC wafer surface cleaning techniques. In Si technology for example, improper removal of surface contamination and oxides prior to Si homoepitaxy has been shown to result in an increase in the density of line and planar defects in epitaxial films from $< 10^4/\text{cm}^2$ to $> 10^{10}/\text{cm}^2$ [2-4]. These increased defect densities were in turn found to correspond with a decrease in device yield [5]. In the case of heteroepitaxy, studies on $\text{Si}_x\text{Ge}_{1-x}$ alloy growth on Si (100) have additionally shown that surface defects produced in the Si substrate by residual organic/carbon contamination act as the preferred sites for misfit dislocation generation [6]. These examples clearly illustrate that surface preparation and cleaning should be equally important to the control of defects in both homoepitaxial and heteroepitaxial growth of SiC and III-V nitrides on (0001) 6H-SiC.

Due to a limited number of studies concerned with *ex situ* SiC cleaning practices [7-10], most SiC *ex situ* wet chemical processing has been based on processes specifically developed for and employed in Si technology [10,11]. Silicon carbide *ex situ* cleaning/surface preparation has typically consisted of some variation of solvent degreasing, organic contaminant removal using RCA or Piranha cleans, and finishing with oxide removal using an HF based solution [7-11]. However, an important assumption underlying the use of these procedures is that SiC surfaces should behave similar to silicon surfaces in these wet chemicals. In fact in a previous paper, examples were provided of where this assumption fails specifically with regard to oxide removal from SiC with an HF dip. In Si technology, oxide removal with HF is known to generate a hydrophobic, hydrogen terminated surface, stable against oxidation in air for several hours [12-17]. However, it has previously been shown that SiC surfaces are inherently hydrophilic after oxide removal with HF [18]. The hydrophilic surface allows water and HF to become trapped in micropipes in the SiC wafer which can lead to large concentrations of oxygen and fluorine at the SiC/dielectric interface if not properly outgassed. In order to produce a hydrophobic surface, passivation/capping layers based on silicon and/or fluorocarbons were required [18].

An alternative to the use of passivation layers to form hydrophobic SiC surfaces would be to develop a completely dry *ex situ* cleaning process and, thus, remove the need for a hydrophobic surface. In Si and GaAs technology, dry removal of carbon contaminants from surfaces using UV/O₃ oxidation has become a popular alternative to wet chemical

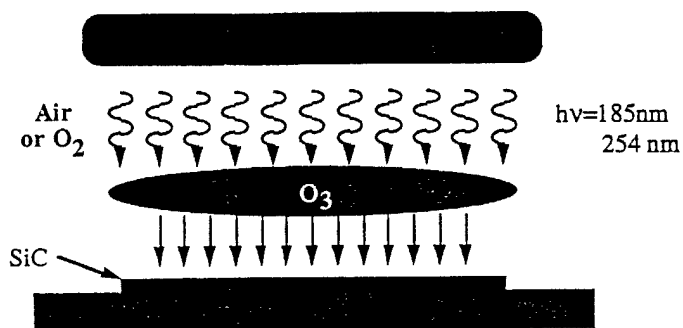
processing [19-25]. In UV/O₃ oxidation, UV radiation from a Hg lamp (specifically the 184.9 nm line) is used to photo excite molecular oxygen (O₂) to generate ozone (O₃). The 253.7 nm line of Hg is in turn adsorbed by O₃ to form atomic O. Atomic oxygen and ozone are extremely reactive species which rapidly oxidize organic contaminants forming CO and CO₂ which desorb from the surfaces. The 253.7 nm line of Hg also assists in removal of carbon contaminants as it is adsorbed by most hydrocarbons and excites C-H and C-C bonds. Removal of the UV/O₃ generated surface oxides is typically achieved by wet chemical processing and/or *in situ* thermal desorption [19,20,22,24]. However, Iyer *et al.* [25] have shown that the equilibrium vapor from an HF solution can be alternatively used to remove the native oxide from a silicon wafer via a dry *ex situ* process. Thus, the combined use of UV/O₃ oxidation for removal of carbon contaminants and HF vapor exposure for oxide removal represents a completely dry *ex situ* cleaning process. Completely dry *ex situ* cleaning processes are advantageous not only for working with hydrophilic surfaces but are economical and environmentally friendly. Use of completely dry processing techniques eliminates the need for large quantities of expensive high-purity chemicals while simultaneously reducing the costs for disposal of these toxic materials [26-28]. The use of smaller quantities of wet chemicals also has the added benefit of minimizing the amount of toxic chemicals released into the ecosystem [26].

In this paper, we demonstrate for the first time a completely dry *ex situ* cleaning process for (0001)_{Si} 6H-SiC surfaces which is based on the combined use of UV/O₃ oxidation and HF vapor cleaning. This clean has been found to be equivalent to or better than typical wet chemical processes in terms non-carbidic carbon and oxide contamination levels as measured by XPS. The combined UV/O₃-HF vapor treatment eliminates the need for a hydrophobic SiC surface and avoids the use of exotic passivation layers.

B. Experimental Procedure

On axis, n-type (typically $N_d=10^{18}/\text{cm}^3$) (0001)_{Si} 6H-SiC wafers were used in these experiments. Prior to UV/O₃ oxidation, each wafer was first ultrasonically degreased in trichloroethylene, acetone, and methanol for 10 min. each. The UV/O₃ treatments described in this study employed a box in which a high intensity Hg lamp was positioned in close proximity (≈ 1 cm) to the SiC wafer (see Fig. 1). In order to increase the concentration of O₃ generated (i.e. to increase oxidation rate), the UV/O₃ box was purged with 1 L/sec O₂ during the UV exposure. Further details of this process have been described previously [20]. HF vapor cleans were achieved by simply positioning the SiC wafer within approximately 5 mm of a 10:1 buffered HF solution for times ranging from 5-30 min. (see Fig. 1). Condensation of HF on the SiC surface was not observed for exposures of this length.

a.) UV/Ozone



b.) HF Vapor

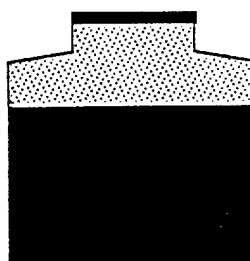


Figure 1. (a) Schematic of UV/O₃ oxidation system and (b) schematic of HF vapor procedure.

Surfaces prepared in the above manner were subjected to surface analysis in an integrated ultra-high vacuum system incorporating the following analytical techniques: X-ray Photoelectron Spectroscopy (XPS), Auger Electron Spectroscopy (AES), Electron Energy Loss Spectroscopy (EELS), and Low Energy Electron Diffraction (LEED). Details of this system are given elsewhere [29]. After each treatment above, the SiC wafer was mounted to a molybdenum sample holder and loaded into a load lock for subsequent analysis by AES, XPS, EELS, and LEED. XPS analysis was performed using the Al anode ($h\nu=1486.6$ eV) at 20mA and 12 kV. AES spectra were obtained using a beam voltage of 3 keV and an emission current of 1 mA. EELS spectra were obtained using a 100 eV electron beam and an emission current of 1 mA. LEED was performed using rear view optics, a beam voltage of approximately 115 eV, and an emission current of 1 mA. Calibration of the XPS binding energy scale was performed by measuring the position of the Au 4f_{7/2} and shifting the spectra such that the peak position occurred at 83.98 eV.

C. Results

Solvents and UV/O₃. Figures 2(a) and (b) show XPS spectrums of the C 1s core level taken from a (0001)_{Si} 6H-SiC surface before and after a UV/O₃ oxidation treatment. As can be seen in Fig. 2(a), a fairly broad C 1s spectrum was observed prior to UV/O₃ oxidation. Data analysis of this spectrum revealed the presence of two C 1s peaks centered at 282.5 and

283.6 eV which were assigned to carbidic (C-Si) and non-carbidic (C-C, C-H, etc.) carbon, respectively. The large FWHM (full width half maximum) of 2.6 eV for the non-carbidic C1s peak suggests that the non-carbidic carbon is a mixture of C-C and C-H bonding states. In addition, we have previously detected from these surface traces of non-carbidic carbon centered at 286.0 eV which may be indicative of C-F bonding [18]. Following a two-hour UV/O₃ treatment, a large shift in the non-carbidic C1s peak from 283.6 to 284.2 eV was observed. This was in contrast with the carbidic C1s peak which only increased by 0.1 eV to 282.6 eV. In addition, the carbidic/non-carbidic carbon ratio was observed to increase from 0.8 to 2.7 after the UV/O₃ treatment. The shift and reduction in the non-carbidic C1s peak is consistent with the formation of C-O bonding at the surface and removal of some non-carbidic carbon via desorption of CO and CO₂.

XPS of the Si 2p core level from the (0001)_{Si} 6H-SiC surface before and after UV/O₃ treatment (see Figs. 3a and 3b) additionally shows the formation of silicon oxides on the surface. As shown in Fig. 3a, a single Si 2p peak is detected before UV/O₃ oxidation. The line shape of this Si 2p peak is asymmetric suggesting the possibility of a Si-O bonding peak on the higher BE (binding energy) side. Unfortunately, deconvolution of this peak is complicated by the fact that the Si 2p peak is really an unresolved doublet (i.e. Si 2p_{3/2,1/2}). As such, it was not possible to irrefutably determine whether a Si-O peak existed. However, after the UV/O₃ treatment, a broad Si-O peak centered at 102.4 eV (FWHM=2.1 eV) was clearly detected (see Fig. 3b). The width of the Si 2p peak at 102.4 eV indicates that silicon in +2, +3, and +4 oxidation states is bonded to the oxygen (i.e. Si-O, O-Si-O, Si=O).

In a previous paper, it was demonstrated that the surfaces of as received on and off axis (0001)_{Si} 6H-SiC wafers were covered with a thin layer of fluorocarbon contamination [18]. As such removal of this contamination layer by UV/O₃ oxidation should be evidenced by a reduction in the F 1s peak which is exactly what was observed. As shown in Figure 4(b), two F 1s peaks at 685.4 and 687.2 eV were detected from the (0001)_{Si} surface prior to oxidation. These two peaks were assigned to Si-F and C-F bonding respectively. After the UV/O₃ treatment, only a slight trace of the lower binding energy F 1s peak was detected and it was observed to shift by 0.5 eV to 685.9 eV (see Fig. 4c). The higher binding energy peak at 687.2 eV believed to be due to fluorine bonded to carbon was completely eliminated indicating removal of any fluorocarbons present on the surface.

HF Vapor. After oxidation of the (0001)_{Si} 6H-SiC surface using a UV/O₃ treatment, removal of the thin silicon oxide layer grown on the surface was achieved by exposing the SiC surface to the vapor from a 10:1 buffered HF solution for 30 min. As shown in Fig. 3(c), the higher binding energy Si 2p peak centered at 102.4 eV was completely removed by the HF vapor treatment. Shorter HF vapor treatments were observed to still leave a Si-O Si2p peak at much larger BE (\approx 104 eV).

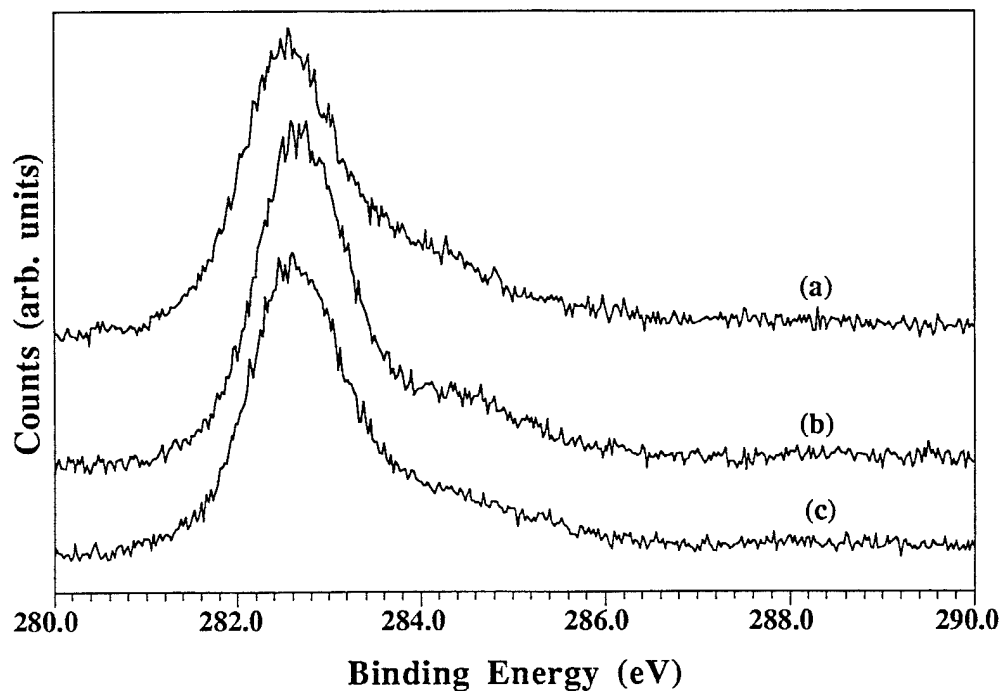


Figure 2. XPS of C 1s from on axis (0001)_{Si} 6H-SiC after (a) solvent cleaning, (b) UV/O₃, and (c) HF vapor cleaning.

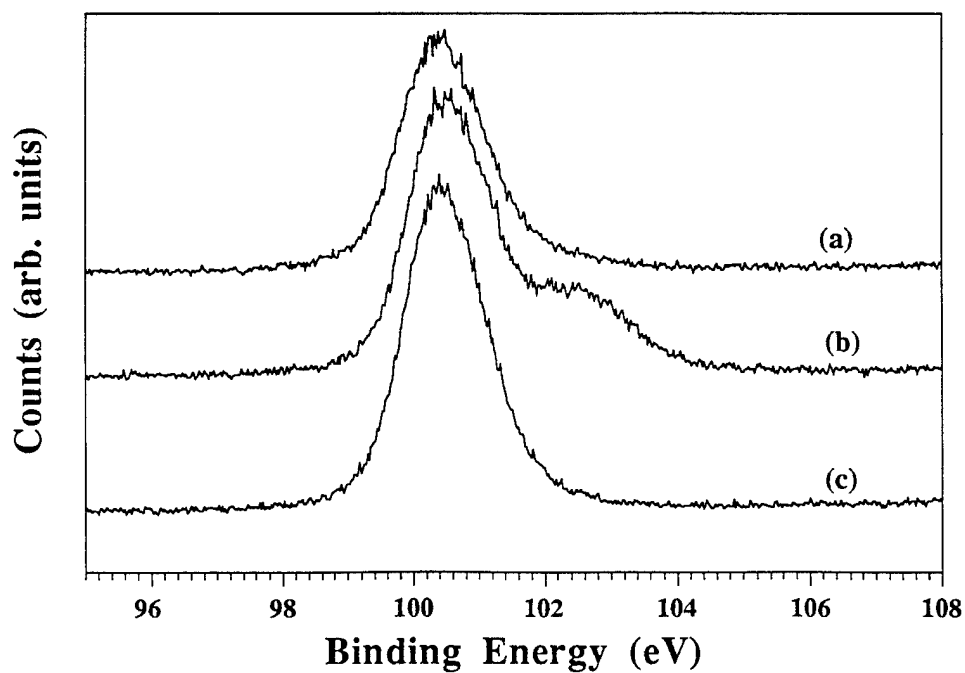


Figure 3. XPS of Si 2p from on axis (0001)_{Si} 6H-SiC after (a) solvent cleaning, (b) UV/O₃, and (c) HF vapor cleaning.

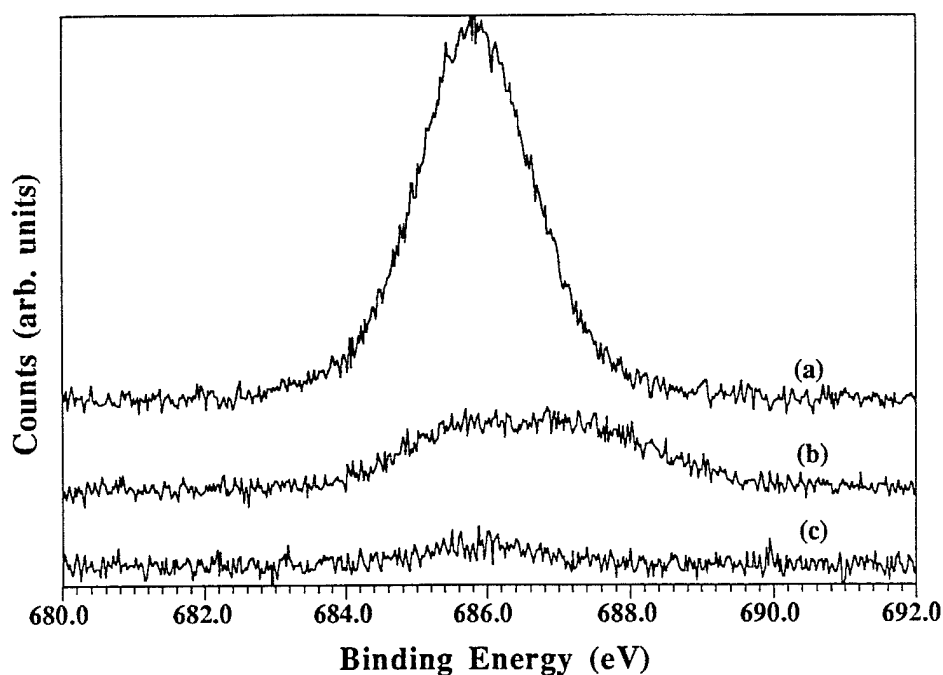


Figure 4. XPS of F 1s from on axis (0001)_{Si} 6H-SiC after (a) HF vapor cleaning, (b) solvent cleaning, and (c) UV/O₃.

Table I. Core Levels Positions from (0001)_{Si} 6H-SiC after Various Treatments

	Si 2p (FWHM)	C 1s	O 1s	F 1s
Solvents	100.4, 1.5	282.5, 1.1 283.6, 2.6	531.6, 2.3	685.4, 1.8 687.2, 2.7
UV/O ₃	100.5, 1.4	282.6, 1.1 102.4, 2.1	532.1, 2.4 284.2, 2.1	685.9, 1.9
HF Vapor	100.5, 1.5	282.6, 1.1 283.8, 2.8	531.8, 2.3	685.8, 1.9

Table II. Core Level Ratios from (0001)_{Si} 6H-SiC after Various Treatments

	carbodic/noncarbodic	Si/O	Si/F
Solvents	0.8	1.1	5.4
UV/O ₃	2.7	0.3	10.6
HF Vapor	1.7	1.3	0.5

After the HF vapor treatment, the amount of non-carbidic surface carbon was observed to increase with the corresponding carbidic/non-carbidic carbon ratio decreasing from 2.7 to 1.7. The non-carbidic C1s peak was likewise observed to shift down to 283.8 eV and with a huge increase in FWHM from 2.1 to 2.8 eV. However, the carbidic/non-carbidic carbon ratio of 1.7 after the HF vapor treatment is still much larger than the 0.8 that was found after only solvent cleaning.

In addition to an increase in non-carbidic carbon after the HF vapor treatment, the amount of fluorine on the surface was also observed to increase dramatically (see Fig. 4a). Prior to the HF vapor treatment, the Si/F ratio was equal to 10.6. However, after the HF vapor treatment the Si/F ratio plummeted to 0.56. Further, the position of the F 1s was not observed to shift but remained centered at 685.9 eV which suggests that fluorine is bonded only to silicon atoms at the surface.

D. Discussion

UV/O₃ Oxidation. In the above section, it was demonstrated that exposure of (0001)_{Si} 6H-SiC surfaces to ozone generated by a Hg UV lamp oxidized and removed non-carbidic carbon from the SiC surface. This resulted in an increase of the carbidic/non-carbidic carbon ratio from 0.8 to 2.7. This result is in agreement with previous studies of UV/O₃ oxidation of Si and GaAs surfaces which have also shown a removal of carbon contaminants [19-24]. However, some non-carbidic carbon was observed to be still present on the SiC surface after the long UV/O₃ treatment. Some of this non-carbidic carbon is surely due to recontamination of the SiC surface during sample transfer and mounting in a laboratory ambient prior to insertion into vacuum. However, contamination levels of this magnitude are usually not observed from silicon wafers cleaned in the same environment. Alternatively, the remaining non-carbidic carbon could be due to carbon trapped in the silicon oxide layer and or carbon bonded to both silicon and oxygen at the SiC/silicon oxide interface. The shift in the position of the non-carbidic C 1s peak from 283.6 to 284.2 eV with UV/O₃ oxidation is in the direction expected for oxidation of carbon. For HF dipped Si wafers, it has been previously determined that residual carbon contaminants with C 1s peaks positions of 284.6, 286.3, and 288.4 eV are composed mostly of C-H₂, C-O, and O-C=O bonded carbon respectively [30]. Additionally, the C 1s peak position from graphite is known to occur at 284.5 eV [31]. Unfortunately, a direct comparison between the non-carbidic C1s peak position/bonding configuration for both Si and SiC surfaces is complicated by the probable existence of 0.5-1.0 eV of band bending at the SiC surface due to surface Fermi level pinning. Pinning of the Fermi level causes the binding energy of the C 1s (and Si 2p, O1s, etc.) peak positions to be decreased by 0.5-1.0 eV relative to their corresponding "bulk" values. However, as HF dipped Si surfaces are known to exhibit a flat band condition, one can a priori add 1.0 eV to the SiC C1s core levels and see that

prior to UV/O₃ the non-carbidic carbon is composed of mostly C-C and CH₂ bonds and after the UV/O₃ treatment the non-carbidic carbon is closer to C-O bonding. The authors also note that the studies of Fominski *et al.* [32] and Baunack and Zehe [24] do not report complete removal of carbon contaminants from Si surfaces using O₃ generated from a Hg lamp. In fact, Fominski *et al.* [32] found it necessary to switch to deeper UV from a D₂ lamp and use an O₂/NF₃/H₂ gas mixture. Complete removal of non-carbidic carbon via UV/O₃ oxidation to the authors knowledge has only been clearly demonstrated for GaAs surfaces and even then it is debatable whether the carbon is removed or just buried at the GaAs/oxide interface.

Although the UV/O₃ oxidation treatment was not completely successful in removing all of the non-carbidic carbon from the SiC surface, a comparison of this technique with other wet chemical techniques does show the utility of the technique. In a previous paper, we examined the effect that standard wet chemical treatments such as RCA SC1 and Piranha etch have on the removal of the same carbon surface contamination observed in this study. Table III provides a direct comparison of the carbidic/non-carbidic carbon and Si/O ratios for each treatment. As can be seen, the UV/O₃ treatment provides the highest carbidic/non-carbidic ratio of all the treatments examined and is, therefore, the best at removal of carbon contaminants. The authors additionally note that UV/O₃ oxidation over RCA cleaning has been recently demonstrated by Afanas'ev *et al.* [33]. Their results have found UV/O₃ oxidation to be a useful cleaning/pre-oxidation procedure prior to thermal oxide growth for SiC/SiO₂ MOS structures. In comparison to RCA cleaned SiC samples, they observed that the UV/O₃ pre-oxidation treatment resulted in a reduction defect species (fast interface states) and positive charge at the SiC/SiO₂ interface from $2 \times 10^{12}/\text{cm}^2$ to $6-8 \times 10^{11}/\text{cm}^2$. They propose/speculate that the reduction in positive charge by the UV/O₃ treatment is due to the removal of carbon clusters (i.e. C-C bonding) left on the SiC surface after growth of epitaxial layers and which are not removed by RCA cleaning or the thermal oxidation process itself. The authors note that this speculation is supported by our observation that UV/O₃ oxidation removed and shifted non-carbidic carbon or C-C and C-H₂ bonding on our SiC surfaces to higher oxidation states.

Finally, the authors note the enhanced ability of the UV/O₃ to oxidize SiC surfaces in comparison to other standard wet chemical treatments such as RCA SC1, and boiling aqua regia which are known to form passivating oxides on silicon. As shown in Table III, the Si/O ratio of 0.3 produced by a UV/O₃ treatment is much lower than the ≈ 1.0 produced by wet chemical treatments such as boiling Aqua Regia and RCA SC1. In fact, this ratio is not significantly different from the Si/O ratio of 1.1 observed from solvent cleaned SiC surfaces. However, this observation is consistent with the known inability of any of these acids to etch SiC. Therefore, the ability of UV/O₃ to grow a thin (10-20 nm) passivating oxide is an added benefit over conventional wet chemical processing. Also, the ability to form the passivating

Table III. Summary of Carbodic/Non-carbodic Carbon and Si/O Ratios from XPS Data

Treatment	Carbodic/Non-carbodic	Si/O
Solvents	0.8	1.1
Piranha	1.1	0.9
RCA SC1	2.2	1.0
Aqua Regia	1.2	1.2
UV/O ₃	2.7	0.3
HF dip	6.6	1.4
HF vapor	1.3	1.2

oxide at room temperature is an additional bonus as thermal oxidation of SiC typically requires temperatures of 1000-1200°C [34]. Lastly, the authors note that the Si 2p spectrum generated from SiC by UV/O₃ oxidation (see Fig. 3b) bares a striking resemblance to the Si 2p spectra obtained from a SiC sample exposed to a total fluence of 9×10^{21} oxygen atoms (i.e. O instead of O₂) during low earth orbit on a satellite [35]. This suggests that UV/O₃ oxidation could be used to simulate the operational conditions of SiC devices in outer space and other harsh oxidizing environments.

HF Vapor. As Figures 2(b) and 2(c) show, the equilibrium vapor from an HF solution alone can be used to effectively remove silicon oxides from SiC surfaces. Though Fig. 2(c) shows the complete removal of the higher BE Si 2p peak at 102.4 eV, some oxygen was observed to remain on the SiC surface (probably in the form of suboxides of silicon and carbon i.e. C₃-Si-O and Si₃-C-O). Table III shows that the resulting Si/O ratio after the vapor treatment was observed to increase from 0.3 to 1.3. The Si/O ratio of 1.3 compares well with the value of 1.4 obtained from a SiC surface after removal of a thermal oxide with a 10:1 HF dip [18]. This clearly illustrates that HF vapor exposure is equally as effective as HF dips in removing surface silicon oxides from SiC surfaces. The authors do note, however, that the silicon oxide etch rates for HF vapor and HF dips are extremely different. In the HF vapor case, 30 minutes is required to remove only 10-20 nm of UV/O₃, whereas in the HF dip case, only 10 minutes were required to remove 100 nm of thermal oxide.

Unfortunately, the carbodic/non-carbodic carbon ratio was observed to decrease from 2.7 to 1.7 after the HF vapor treatment. Most of this can be blamed on the laboratory environment. A much smaller decrease would be expected for HF vapor treatments conducted in a clean room environment.

The authors also note that the HF vapor treatment left a significantly large amount of fluorine on the SiC surface. The observed fluorine coverage following the HF vapor treatment was 3-4 times larger than that observed from SiC wafers dipped in 10:1 HF and blown dry

without a de-ionized water rinse. The fluorine surface coverage approaches that of 1/2-full monolayer. As the peak position of the F 1s core level after the HF vapor treatment remains essentially unchanged at 685.9 eV (i.e. Si-F bonding), this suggests that the HF vapor treatment leaves a Si-F terminated SiC surface. These results are in contrast with those of Iyer *et al.* [25] for silicon (100) in which no fluorine was detected by XPS and hydrogen termination was confirmed by TPD. These results might explain the observed partial hydrophobic nature of SiC surfaces on removal from HF solutions where partial fluorine coverage has been found, and the observed hydrophilic nature of SiC surfaces after rinsing in de-ionized water which has been found to remove/rinse fluorine from the surface [18]. Perhaps in contrast to Si, fluorine termination of SiC surfaces is favored over hydrogen termination. For silicon, it has been reasoned that hydrogen termination exist due to the fact that the energy level of the hydrogen ion in solution corresponds closely to the top of the Si valence band [26]. In contrast, 6H-SiC has a wider band gap of 3.0 eV and hence the SiC valence band maximum will lie well below that of the hydrogen ion in HF. However, the fluorine ion is more electronegative and will lie at a lower energy level much closer to the SiC valence band maximum, hence the a possible explanation/reason for fluorine termination rather than hydrogen termination of SiC surfaces.

E. Conclusions

In conclusion, a completely dry process which removes carbon contamination from (0001)_{Si} 6H-SiC surfaces via UV/O₃ oxidation and removes surface oxides via HF vapor exposure has been demonstrated. Based on the levels of non-carbidic carbon and oxide surface contaminants, this dry cleaning procedure has been found to be equivalent to or better than other standard wet chemical processes. Contrary to silicon, the HF vapor exposure is observed to leave a fluorine terminated SiC surface as opposed to a hydrogen terminated SiC surface.

F. Future Research Plans and Goals

HF vapor and UV/O₃ cleaning of (000-1)_C 6H-SiC will be investigated. In addition, investigation will be conducted of other processes which could lead to better hydrogen or fluorine termination of (0001) 6H-SiC.

G. References

1. W. Kern, J. Electrochem. Soc. **137** (6), 1887 (1990).
2. G. R. Srinivasan and B. S. Meyerson, J. Electrochem. Soc. **134** (6), 1518 (1987).
3. B. S. Meyerson, E. Ganin, D. A. Smith, and T. N. Nguyen, J. Electrochem. Soc. **133** (6), 1232 (1986).
4. M. K. Sangneria, M. C. Ozturk, G. Harris, K. E. Violette, I. Ban, C. A. Lee, and D. M. Maher, J. Electrochem. Soc. **142** (11), 3961 (1995).
5. R. Williams, *Modern GaAs Processing Methods*, 2nd ed. (Artech House, Inc., New York, 1990), pp. 81-114.

6. F. K. LeGoues, MRS Bulletin **21**, 38 (1996).
7. L. M. Porter, R. F. Davis, J. S. Bow, M. J. Kim, R. W. Carpenter, R. C. Glass, J. Mater. Res. **10** (3), 668 (1995).
8. H. Tsuchida, I. Kamata, and K. Izumi, Jpn. J. Appl. Phys. **34**, 6003 (1995).
9. Y. Mizokawa, S. Nakanishi, O. Komoda, S. Miyase, H. S. Diang, C. Wang, N. Li, and C. Jiang, J. Appl. Phys. **67** (1), 264 (1990).
10. U. Starke, Ch. Bram, P. R. Steiner, W. Hartner, L. Hammer, K. Heinz, K. Muller, Appl. Surf. Sci. **89**, 175 (1995).
11. M. E. Lin, S. Strite, A. Agarwal, A. Salvador, G. L. Zhou, M. Teraguchi, A. Rockett, and H. Morkoc, Appl. Phys. Lett. **62**, 702 (1993).
12. B. S. Meyerson, F. J. Himpsel, and K. J. Uram, Appl. Phys. Lett. **57**, 1034 (1990).
13. M. Grundner and H. Jacob, Appl. Phys. A **39**, 73 (1986).
14. Y.J. Chabal, G. S. Higashi, K. Raghavachari, and V. A. Burrows, J. Vac. Sci. Technol. A **7** (3), 2104 (1989).
15. G. S. Higashi, R. S. Becker, Y. J. Chabal, A. J. Becker, Appl. Phys. Lett. **58**, 1656 (1991).
16. G. S. Higashi, Y. J. Chabal, G. W. Trucks, and K. Raghavachari, Appl. Phys. Lett. **56**, 656 (1990).
17. M. Houston and R. Maboudian, J. Appl. Phys. **68**, 3801 (1995).
18. S. King *et al.* to be published.
19. T. Takahagi, I. Nagai, A. Ishitani, H. Kuroda, and Y. Nagasawa, J. Appl. Phys. **64**, 3516 (1988).
20. J. A. McClintock, R. A. Wilson, and N. E. Byer, J. Vac. Sci. and Technol. **20**, 241 (1982).
21. R. F. Kopf, A. P. Kinsella, and C. W. Ebert, J. Vac. Sci. Technol. B **9**, 132 (1991).
22. M. Suemitsu, T. Kaneko, and M. Miyamoto, Jap. J. Appl. Phys. **28**, 2421 (1989).
23. S. J. Pearton, F. Ren, C. R. Abernathy, W. S. Hobson, and H.S. Luftman **58**, 1416 (1991).
24. S. Baunack and A. Zehe, Phys. Stat. Solid A **115**, 223 (1989).
25. S. S. Iyer, M. Arienzo, and E. de Fresart, Appl. Phys. Lett. **57**, 893 (1990).
26. T. Ohmi, J. Electrochem. Soc. **143**, 2957 (1996).
27. R. Iscoff, Semiconductor International **7**, 58 (1993).
28. W. A. Cady and M. Varadarajan, J. Electrochem. Soc. **143**, 2054 (1996).
29. J. van der Weide and R. J. Nemanich, Appl. Phys. Lett. **62**, 1878 (1985).
30. A. Miyauchi, Y. Inoue, M. Ohue, N. Momma, and T. Suzuki, J. Electrochem. Soc. **137**, 3257 (1990).
31. K. L. Smith and K. M. Black, J. Vac. Sci. and Technol. A **2**, 744 (1984).
32. V. Y. Fominski, O. I. Naoumenko, V. N. Nevolin, A. P. Alekhin, A. M. Markeev, and L. A. Vyukov, Appl. Phys. Lett. **68**, 2243 (1996).
33. V. V. Afanas'ev, A. Stesmans, M. Bassler, G. Pensi, M. J. Schulz, and C. I. Harris, Appl. Phys. Lett. **68**, 2141 (1996).
34. J. W. Palmour, PH. D. Dissertation, North Carolina State University.
35. G. N. Raikar, J. C. Gregory, W. D. Partlow, H. Herzig, and W. J. Choyke, Surface and Interface Analysis **23**, 77 (1995).

Nitrogen-based Materials

V. Growth of Bulk AlN and GaN Single Crystals by Sublimation

A. Introduction

The current lack of easily produced single crystal wafers of III-V nitrides of moderate cost is an impediment to the rapid enhancement/development of epitaxial thin films and selected devices produced from these materials. The realization of blue and green light emitting diodes and blue lasers, as well as prototypes of several microelectronic devices produced from GaN-based materials containing copious line and planar defects has been most fortunate. It also strongly indicates that the employment of substrates on which homoepitaxial films can be grown will result in marked improvements in the devices fabricated in these films.

The properties of the III-V nitrides which have made growth of bulk crystals a challenge include (1) high melting points, (2) low sublimation/decomposition temperatures relative to their melting temperatures, (3) very high equilibrium nitrogen vapor pressures at moderate temperatures and (4) low solubility in acids, bases and most other inorganic elements and compounds. Thus, novel bulk growth techniques must be employed which either take advantage of these inherent properties or surmount the difficulties presented by them.

Bulk growth of monocrystalline AlN by sublimation/recondensation [1-7], evaporation/reaction [8] and solution routes [9-10] has been attempted in several laboratories. The results of the first two processes [1-8] have been small crystals. Prior to the present research, Slack and McNelly [1,2] had achieved the largest crystals (10 mm long \times 3 mm in diameter) using the sublimation/recondensation method at 2250°C. An extensive experimental study for producing unseeded single crystals has been conducted by Dugger [9-10] using AlN-Ca₃N₂ solutions contained in graphite crucibles. The solutions were cooled from 1550°C at 2°/hr for 26 hours. Small (1.1 mm long \times 0.3 wide) crystals were achieved via nucleation on the crucible walls. The important aspect of this work is that Ca₃N₂ is an effective solvent for AlN with the solubility exceeding 10% at 1200°C. However, it is incompatible with graphite crucibles.

Relatively fewer attempts to grow bulk crystals of GaN have been reported. Elwell and Elwell [11] have reviewed this work to 1988. Two major approaches have been used: vapor phase transport [12-15] and solution techniques [16-21]. Success of these methods has been limited to small crystals. The high pressure solution approach has achieved approximately the same results. The initial research [19,20] in high pressure synthesis produced platelets limited in size to \approx 1 mm. Recent publications by these authors (see, e.g., Ref. [21]) note that they have now achieved crystals 8 mm square \times 0.2 mm thickness. The growth rate in this technique is reported to be \approx 20 μ m/hr. Recently, Sakai and coworkers [22] have grown GaN needles by sublimation of GaN powder on a sapphire substrate. However, crystal size was reported to be limited to small needles.

The recent results of research conducted by the present authors and described in the following sections represent important advances in the determination of the process parameters and the accomplishments regarding growth via sublimation of AlN and GaN bulk single crystals. This is also the first report of seeded growth of thick crystals of AlN. The crystals of both materials were of very high quality. Comparisons of our diffraction, photoluminescence and Raman data with those available in the literature indicate that our crystals are superior to any bulk GaN or AlN grown to date.

B. Experimental Procedures

Sublimation Growth of Single Crystals of AlN and Their Characterization. The AlN sublimation experiments were conducted in a resistively-heated graphite furnace having a maximum temperature of 2500°C. This furnace was also internally adaptable to allow the achievement of the temperature gradients required for material transfer from source-to-seed. An important feature of the growth system was the capability of changing the axial position of the seed crystal with respect to the source and heater.

A critical technical issue in the sublimation of AlN was the selection of the material for the crucible. Physical and chemical stability at very high temperatures and compatibility with the furnace atmosphere, source, seed and furnace construction materials and machinability were considered. Initial experiments with graphite resulted in severe degradation of the crucible components due to their reaction with Al vapor. Formation of aluminum carbide (Al_4C_3) was found in the crucibles below 1900°C. Above this temperature, large pits and loose carbon powder were found in the crucibles and believed to result from the formation and subsequent decomposition of Al_4C_3 . To surmount these problems, the crucibles were coated with SiC via chemical vapor deposition. However, the Al vapor slowly diffused through the SiC barrier coating, reacted with the graphite at the interface and eventually caused the coating to peel. However, the lifetime of each coating was sufficient to conduct several 10-15 hrs experiments.

Bulk 99% dense AlN produced via hot pressing without sintering additives was used as the source material to reduce the contamination that would come from the higher concentrations of surface oxide present on AlN powders. Using a solid form of the precursor allowed precise separation between the source and the seed and provided a more stable evaporation rate. The source was placed in the isothermal section of the furnace to ensure a constant evaporation rate. The source-to-seed distance was very important in the achievement of crystal growth, as explained below. The sublimation rate varied from approximately 10 mg/hr to 200 mg/hr as the temperature of the source was raised from 1950 to 2250°C at a background pressure of 500 Torr.

The choice of seed material was very limited due to the high temperatures needed to both sublime AlN and to achieve rapid surface diffusion on the seed, such as to produce bulk single

crystal over relatively short growth times. Single crystal, 6H-SiC wafers (10 mm \times 10 mm) were used as seeds in all experiments, because of their high temperature stability and close lattice matching to AlN (0.9% mismatch).

All experiments were performed under flowing ultra-high purity N₂ maintained at a background pressure of 500 Torr. Two source temperature regimes were investigated: 1950-2050°C and 2050-2250°C. The lower temperature range was chosen primarily because of the degradation of the furnace and seed crystals. In both cases, a temperature difference of 80-150°C was obtained between the source and the seed depending on the distance of separation (1 to 40 mm).

The as-grown AlN bulk crystals were first characterized via optical and transmission electron microscopes. Color, size, transparency and macrostructural features were observed using the former at magnifications between 5X-40X. C-axis oriented TEM samples were prepared by grinding and polishing the bulk AlN crystals to a thickness of 100 μ m, dimpling to a thickness of 20 μ m and Ar⁺-ion milling to electron transparency. The TEM studies were performed using a TOPCON EM-002B, operating at 200 kV. Micro-Raman spectra were obtained at RT from a back scattering geometry utilizing the 514.5 nm line of the Ar laser. The spot size and the spectral resolution were 4 μ m in diameter and 2 cm⁻¹, respectively.

Sublimation Growth of GaN Crystals and Their Characterization. Initial experiments on the growth of GaN were conducted in a modified AlN sublimation system. High purity GaN powder produced in our laboratory [23] and having exceptional structural quality such as to be classified as the X-ray standard for this material [24] or Ga metal were sublimed or evaporated in an ammonia atmosphere and condensed on a substrate. A wide range of experimental parameters including source temperature, seed temperature, pressure, ammonia flow rate and source-to-seed distance were varied to optimize the growth conditions. Efforts regarding the optimization of the process in the above mentioned parameter space is continuing. Prior to sublimation, the GaN powders were compacted to a density of \approx 60%. These pellets were then sublimed under a flow of NH₃. A detailed description of the experimental procedure will be presented in a forthcoming publication.

The GaN crystals were characterized using optical microscopy, Raman spectroscopy and photoluminescence (PL). Raman spectrum of the GaN crystals was acquired in a back scattering geometry from the face perpendicular to the c axis using the same experimental conditions as in AlN. The incoming polarization state of the light was chosen to be perpendicular to the c axis. For PL studies, an Ar-ion pumped mode-locked femtosecond titanium:sapphire laser with a frequency tripler was used as an excitation source. The duration of the excitation pulse is about 250 fs. Photoluminescence was collected, collimated and focused on to the entrance slits of 0.32 m spectrometer, and the sample emission was detected using a cooled GaAs photomultiplier dc coupled to the electrometer and chart recorder.

C. Results and Discussion

Aluminum Nitride. The highest growth rates and thickest crystals (≤ 1 mm) were obtained with a source temperature of $\approx 2150^\circ\text{C}$. Although deposition was observed above 2150°C , the SiC seeds were sufficiently chemically unstable such that only individual crystals nucleated and grew from selected areas. The color of the crystals grown within the temperature interval of 2050 - 2250°C varied from dark blue to dark green. This is believed to be due to carbon and silicon incorporation, respectively, from the SiC substrate. A growth rate of 0.5mm/hr was achieved at a 4 mm separation and 2150°C source and 2080°C seed temperatures. The resulting bulk crystals were analyzed by XRD and Laue back reflection techniques and shown to be monocrystalline.

Growth of AlN in the source temperature range of 1950 to 2050°C was investigated both to prevent seed deterioration and increase crucible lifetime. Complete structural and chemical stability of the SiC seeds and substantial reduction in the deterioration of the SiC-coated crucibles were attained. Crystals grown in this temperature range were always colorless. Typical growth rates were reduced to 30 - $50\text{ }\mu\text{m/hr}$. Thus, growth runs of 10 - 15 hrs yielded crystals having thicknesses of 0.3 - 0.5mm . An optical micrograph (OM) of a 0.4 mm thick transparent layer of AlN grown at 1975°C is shown in Fig. 1.

A bright field TEM micrograph taken in plan view along $[0001]$ and associated selected area diffraction (SAD) pattern are shown in Fig. 2. Uniform contrast density was observed throughout the specimen, indicating excellent quality single-crystalline AlN. No high angle boundaries, stacking faults or twinned regions were observed. The SAD pattern supports these results in that the diffraction spots are without arcs, which would indicate texture and/or grains with different orientation, and spikes, which would indicate stacking faults. Isolated cases of dislocations and low angle grain boundaries were observed at very large separations.

The Raman spectrum of the AlN bulk crystal is presented in Fig. 3. The spectrum was acquired in a back scattering geometry from the c face. The selection rules predict the allowed modes for this geometry to be the $A_1(\text{LO}) \approx 893\text{ cm}^{-1}$, $E_2^{(1)} \approx 250\text{ cm}^{-1}$, $E_2^{(2)} \approx 660\text{ cm}^{-1}$. The spectrum exhibits the allowed modes with no detectable contribution from the forbidden modes [25]. Thus, the AlN crystal has a well aligned c face of the WZ structure with no significant concentration of internal structural defects (which might relax the selection rules). The inset to the figure shows a high resolution spectrum of the $E_2^{(2)}$ mode.

Cracking and separation of the AlN crystal from the SiC seeds was commonly observed after cooling from within both temperature ranges. This is believed to be due primarily to the mismatch in the coefficients of thermal expansion; but the data for these materials are not available for the temperature range employed in this research. However, since AlN boules will ultimately be grown homoepitaxially on AlN seeds, such problems as cracking caused by foreign substrates will not be permanent.

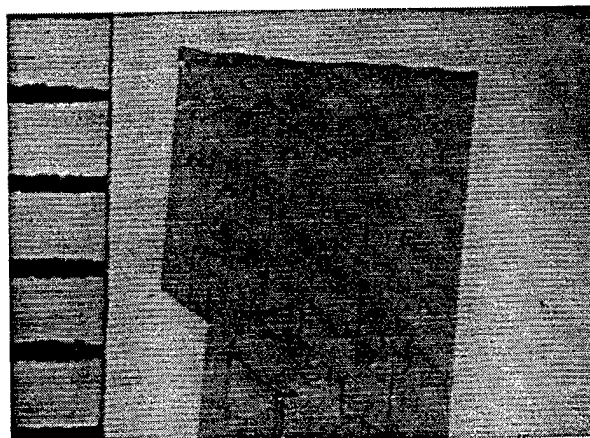


Figure 1. OM image of single crystal AlN grown at 1975°C source temperature. Space between ruled lines = 1 mm.

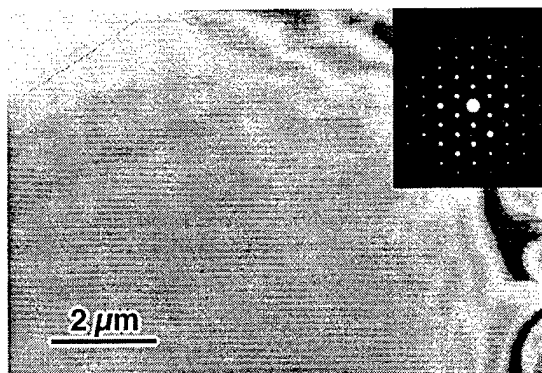


Figure 2. TEM image and selected area diffraction pattern of bulk AlN.

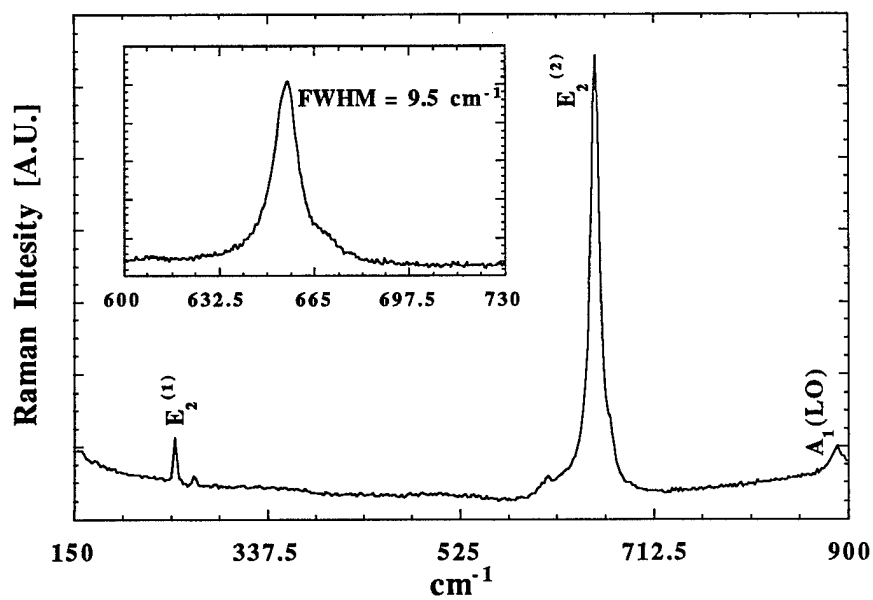


Figure 3. Raman spectrum of bulk AlN.

Gallium Nitride. Colorless, hexagonal crystals were obtained by sublimation of the GaN powder. Figure 4 shows an OM of ≈ 1 mm long, well-faceted, transparent GaN crystal with low aspect ratios which is in contrast to the commonly reported needle-shaped crystals grown via vapor phase reaction.

The direction of fastest growth and, thus, the crystal shape were controlled by changing the Ga/NH₃ flux ratio and the growth temperature. This is a significance advance in that previous work indicates growth of bulk GaN from the vapor phase results primarily in long needles.

Room temperature PL spectrum for bulk GaN is shown in Fig. 5. Strong band edge related emission with a peak position at 365.0 nm (3.4 eV) and the FWHM of 9.0 nm (83 meV) was observed, as shown in Fig. 5 (a). The visible portion of the PL spectrum is expanded 500 times in Fig. 5 (b). No yellow emission attributed to deep level transitions was detected on this scale. 77 K PL spectrum has a peak position at 358.0 nm and FWHM of 6.0 (53 meV).

The allowed modes of the WZ structure are presented in Fig. 6. As in the case of AlN, the conservation of selection rules here is indicative of excellent crystallinity. The inset to the figure shows that the $E_2^{(2)}$ mode is at 567 cm⁻¹ and has FWHM ≈ 3.5 cm⁻¹. These values are indicative of a material of the highest quality reported to date.

D. Conclusions

The first seeded growth of bulk single crystals of AlN (0001) has been achieved on 6H-SiC (0001) substrates in the range of 1950-2250°C at 500 Torr of N₂. The volume of these crystals is the largest ever reported. Close source-to-substrate distances and a 80-150°C temperature gradient were necessary to achieve these results. Color variations were observed above 2150°C and linked to the incorporation of Si and/or C from the substrate and the growth crucible. Cracks in these crystals were observed after cooling regardless of the growth

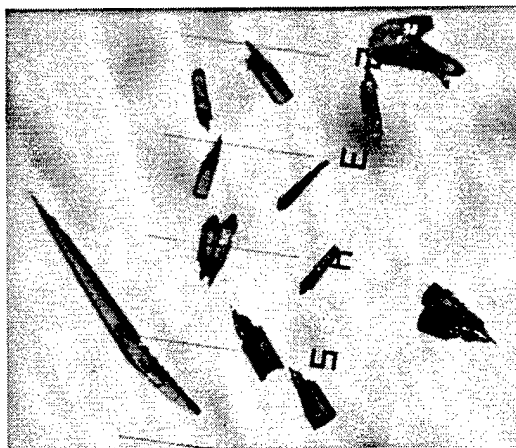


Figure 4. GaN crystals. Lines are spaced 1 mm.

temperature and believed to be caused primarily by stresses due to the mismatch in the coefficients of thermal expansion. Growth of bulk GaN crystals up to 1mm size was achieved via sublimation. Raman and PL spectrums of these crystals revealed excellent crystalline quality.

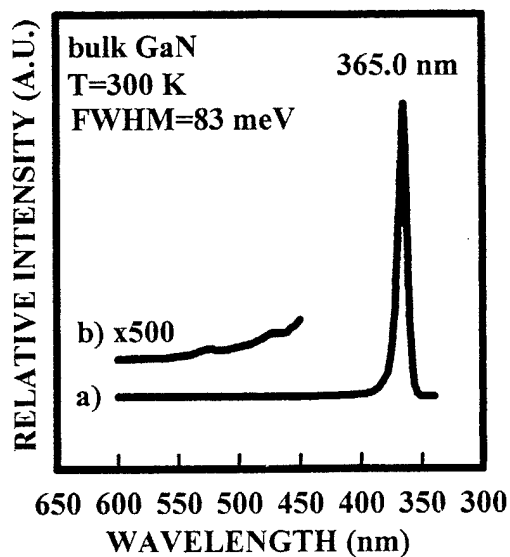


Figure 5. Photoluminescence spectrum of bulk GaN.

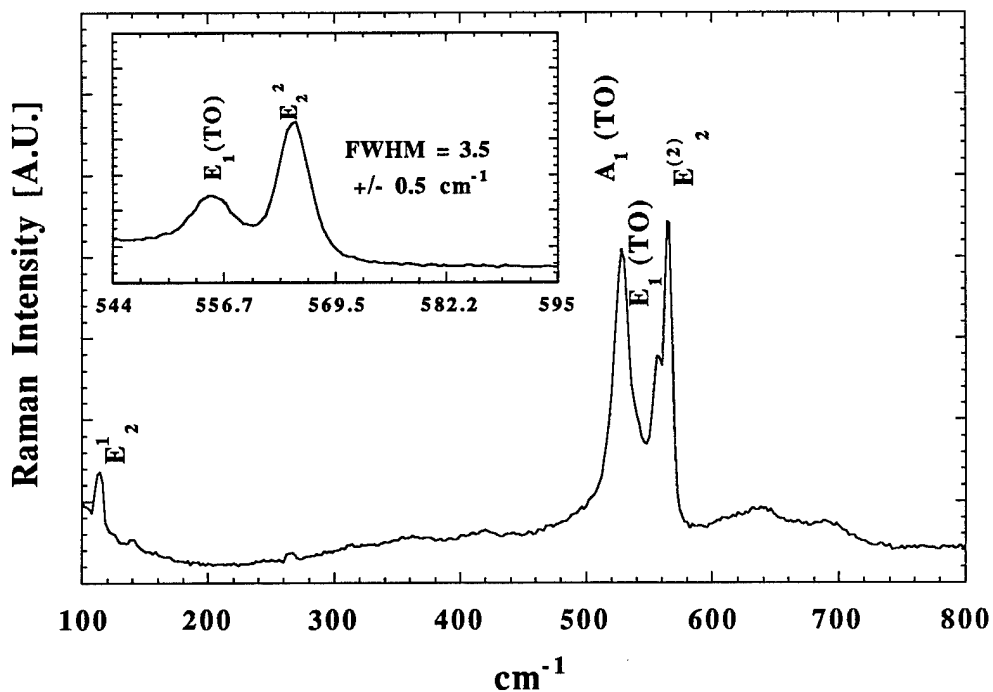


Figure 6. Raman spectrum of GaN.

E. References

1. G. A. Slack and T. F. McNelly, *J. Cryst. Growth* **34**, 263 (1976).
2. G. A. Slack and T. F. McNelly, *J. Cryst. Growth* **42**, 560 (1977).
3. W. F. Knippenberg and G. Verspui, US Pat, 3.634.149.
4. J. O. Huml, G. S. Layne, US. Pat., 3.607.014.
5. J. O. Huml, G. S. Layne, US. Pat., 3.598.526.
6. P. M. Dryburgh, The Ninth International Conference on Crystal Growth, *ICCG-9* (1989).
7. R. B. Campbell and H. C. Chang, Technical Report AFAPL-TR-67-23, Westinghouse Electrical Corporation, Pittsburgh, Pennsylvania (1967).
8. J. Pastrňák and L. Roskovcová, *Phys. Stat. Sol.* **7**, 331, (1964).
9. C. O. Dugger, *Mat. Res. Bull.* **9**, 331, (1974).
10. C. O. Dugger, Air Force Report, AFORL-TR-75-0486, Hanscom AFB Massachusetts, (1975)
11. D. Elwell and M. M. Elwell *Prog. Crystal Growth and Charact.* **17**, 53, (1988)
12. E. Ejder, *J. Cryst. Growth* **22**, 44, (1974)
13. M. Gershenzon, ONR Rept. 243-004F, May (1981).
14. I. G. Pichugin and D. A. Yaskov, *Neorg. Mat.* **6**, 1973, (1970).
15. D. Elwell, R. S. Fiegelson, M. M. Simkins and W. A. Tiller, *J. Cryst. Growth* **66**, 45, (1984).
16. C. J. Frosh, *J. Phys. Chem.* **66**, 877 (1962).
17. R. A. Logan and C. D. Thurmond, *J. Electrochem. Soc.* **119**, 1727, (1972).
18. T. Ogino and M. Aoki, *Oyo Butsuri* **48**, 269, (1962).
19. J. Karpinski, J. Jun and S. Porowski, *J. Cryst. Growth* **66**, 11, (1984).
20. J. Karpinski, and S. Porowski, *J. Cryst. Growth* **66**, 1, (1984).
21. S. Porowski, et.al., *Inst. Phys. Conf. Ser. no:137* **369**, (1994).
22. S. Sakai, S. Kurai, T. Abe and Y. Naoi, *Jpn. J. Apl. Phys.* **35**, L77, (1996)
23. C. M. Balkaş and R. F. Davis, *J. Am. Ceram. Soc.* **79**, [9], 2309, (1996).
24. C. M. Balkaş C. Başçeri and R. F. Davis, *J. Powder. Diffraction* **10**, [4], 266, (1995).
25. L. Bergman and R. J. Nemanich, *Annu. Rev. Mater. Sci.* **26**, 551, (1996).

VI. Growth of III-V Nitride Thin Films on $\alpha(6H)$ -SiC(0001) Via Organometallic Vapor Phase Epitaxy

A. Introduction

With recent world-wide research efforts, the III-V nitride compounds have shown their potential for optoelectronic and microelectronic semiconductor device applications. Advancements in film quality and the understanding of materials issues have led to the demonstration and production of high-quality LEDs. High power, high brightness LEDs with emission spectra ranging from yellow to violet have been produced [1-5]. Using a multiple quantum well heterostructure, Nakamura *et al.* have produced high power blue (5 mW) and green (3 mW) LEDs [5,6] which are now commercially available. There has also been progress recently in the development of laser diodes. Nakamura has demonstrated a current-injected laser diodes on sapphire and spinel substrates with operating voltages around 24 V [7,8]. Although progress has been made in both optoelectronic and microelectronic devices, further developments in the understanding of these materials and improvements in device applications are possible. To further investigate and demonstrate the capabilities of these materials, our research group developed and built a novel organometallic vapor phase epitaxy system. Progress made in the growth of GaN and InGaN films will be discussed in this report.

B. Experimental Procedure

An inverted flow rotating disc OMVPE system was used to grow the nitride films. The design and features of the system have been described in detail in a previous report [9]. The reactants used in the film growth were trimethylaluminum (TMA), triethylgallium (TEG), trimethylindium (TMI) and ammonia (NH_3). Silane (SiH_4) diluted in hydrogen was the silicon source for the n-type dopant. Depending on the film being grown, either hydrogen or nitrogen was used as the diluent. Nitrogen was used as the carrier gas for the metalorganic sources. The system was computer-controlled operated using a LabVIEW (National Instruments) control program developed in-house.

The nitride thin films were grown on on-axis Si-face $\alpha(6H)$ -SiC(0001) substrates. The as-received wafers were cleaved into smaller pieces and degreased. The SiC pieces were then dipped into a 10% HF solution for 10 minutes to remove the thermally grown oxide and then blown dry with N_2 . The substrates were then mounted on a molybdenum substrate holder and loaded in the system. The reactor chamber was evacuated to less than 1×10^{-5} Torr before initiating growth. The substrate was heated to the deposition temperature in the flowing diluent. The deposition pressure was 45 Torr. The substrate holder was rotated continuously during the deposition process. The temperature of the substrate was measured using an Ircon Ultimex Infrared Thermometer. While the growth temperature was being obtained, the flow of the

carrier gas through the metalorganic bubblers was established using a run/vent configuration. The temperature and pressure of each metalorganic bubbler were independently controlled.

Once the growth temperature was reached, film deposition was started by flowing the metalorganic precursor(s) and NH_3 into the reactor. For all films grown, a high temperature AlN buffer layer was used. Buffer layers of AlN were grown between 1100 and 1150°C for times ranging from 5 to 30 minutes. The TMA flow rate was varied between 3.0 and 8.0 $\mu\text{mol/min}$. After the growth of the buffer layer, the temperature was adjusted for the next film layer. GaN growth was investigated in the temperature range between 950 and 1050°C. The TEG flow rate was varied between 17.5 and 25 $\mu\text{mol/min}$. For Si doping, SiH_4 diluted in hydrogen was introduced into the reactor at flow rates varying between 0.15 and 3.75 nmol/min . The InGaN films were grown between 750 and 800°C. The TEG flow rate was varied between 1.4 and 3.8 $\mu\text{mol/min}$. The TMI flow rate was varied between 20 and 35 $\mu\text{mol/min}$. The InGaN films were grown exclusively in nitrogen.

The photoluminescence (PL) properties of the films were determined at room temperature and 4.2 K using a 15 mW He-Cd laser ($\lambda=325\text{ nm}$) as the excitation source. Scanning electron microscopy (SEM) was performed on a JEOL 6400 FE operating at 5 kV. Transmission electron microscopy (TEM) was performed at 200 keV using standard sample preparation techniques. Capacitance-voltage (CV) measurements were taken using a mercury (Hg) probe and a computer-controlled Hewlett-Packard 4284A LCR meter. Contacts for Hall-effect measurements were made using annealed electron-beam deposited Ti/Au.

C. Results and Discussion

GaN Growth. Figure 1 is an SEM micrograph representative of the quality of the surface of the GaN films. On SiC, it has been shown that a deposition of a high temperature, monocrystalline AlN buffer layer is necessary in order to deposit high-quality GaN films [10]. Figures 2 and 3 are TEM micrographs showing the cross-sectional defect structure of the GaN films. The AlN buffer layer has a smooth surface which helps in the deposition of a low defect density GaN layer. Figure 4 is a TEM plan view micrograph of a GaN sample showing the defect concentration in the film. The dislocation density in the film is on the order of $1\text{e}9\text{ cm}^{-2}$, which is approximately one order of magnitude lower than GaN films grown on sapphire [11]. The absence of defects in the GaN shows up in C-V measurements of the material. Undoped films have a measured net ionized carrier concentration ($N_d - N_a$) less than $1\text{e}16\text{ cm}^{-3}$, measured at 1 MHz. Si doping of GaN has been achieved in the range of $5\text{e}16\text{ cm}^{-3}$ to $3\text{e}18\text{ cm}^{-3}$, as measured by C-V at 1 MHz. The Hall-effect mobility for GaN doped at $2\text{e}17\text{ cm}^{-3}$ was measured to be $255\text{ cm}^2/\text{V-s}$, at room temperature. Figure 5 is the PL spectra of GaN at 4.2K. The absence of deep levels is indicative of the high quality of the material. The near-band-edge

peak occurs away from the relaxed value for GaN, possibly indicating strain in the film or near band-edge defect levels. The FWHM is 18 meV.

Gallium nitride films were grown in both hydrogen and nitrogen diluents. There appears to be a difference in film quality depending on the diluent used. Electrical properties for undoped films are similar. However, the PL spectra for the GaN films grown in nitrogen are approximately twice as strong as that for hydrogen grown films. Further optimization of the growth parameters may lead to similar PL results for the two diluents. One other difference between the two diluent gases is the growth rate of the films. AlN buffer layers grown in nitrogen grow at approximately 1/4 the rate of those grown in hydrogen. The GaN films grown in nitrogen grow at approximately 0.7 the rate of those grown in hydrogen. The difference in growth rates can be attributed to the metalorganic chemistry. In the presence of hydrogen, the methyl metalorganic species undergoes an assisted decomposition. The ethyl species, however, decomposes through a β -hydride elimination process, which is influenced less by the presence of hydrogen [12].

InGaN Growth. The InGaN nitride films were grown exclusively in nitrogen. Efforts were made to grow InGaN films in hydrogen, however, the same parameters which yielded indium incorporation in a nitrogen diluent produced only GaN films in a hydrogen diluent. This agrees with other experimental observation [13,14]. It is suggested the hydrogen plays a role in the decomposition of the nitride film, especially in indium containing films. Experiments

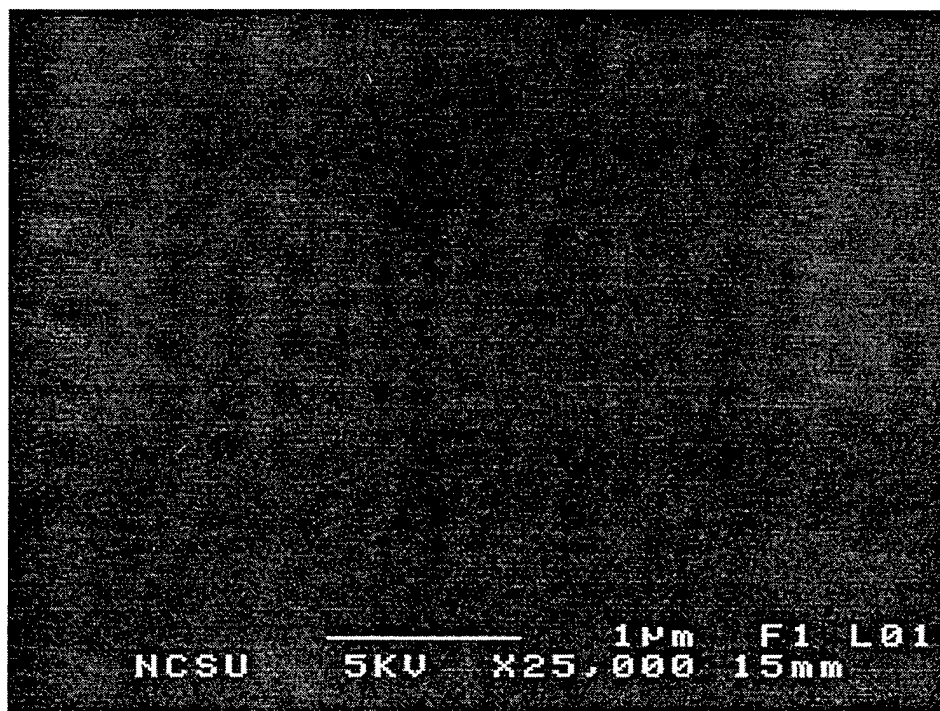


Figure 1. SEM of GaN surface.

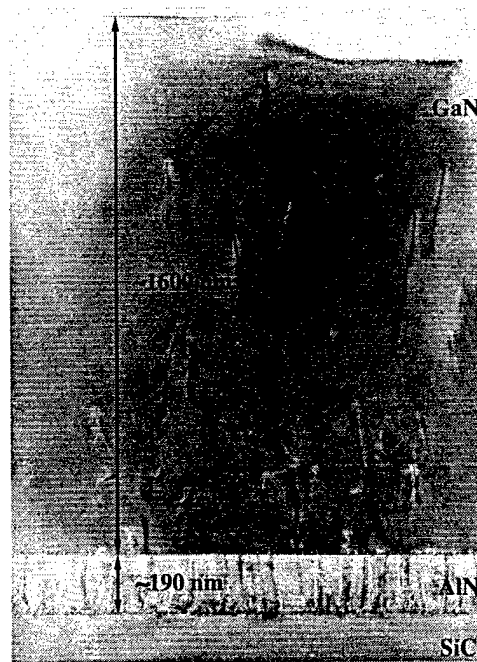


Figure 2. TEM micrograph of GaN and AlN films on SiC.



Figure 3. TEM micrograph of GaN and AlN films on SiC.

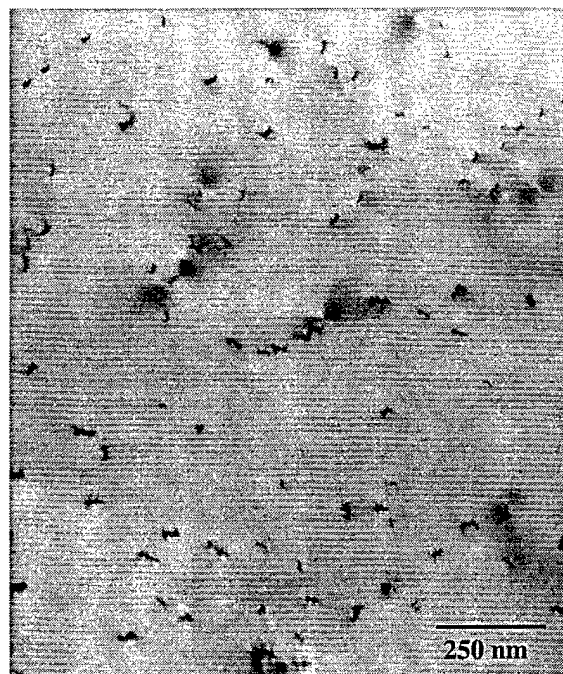


Figure 4. Plan view of GaN film. Dislocation density is approximately $1 \times 10^9 \text{ cm}^{-2}$.

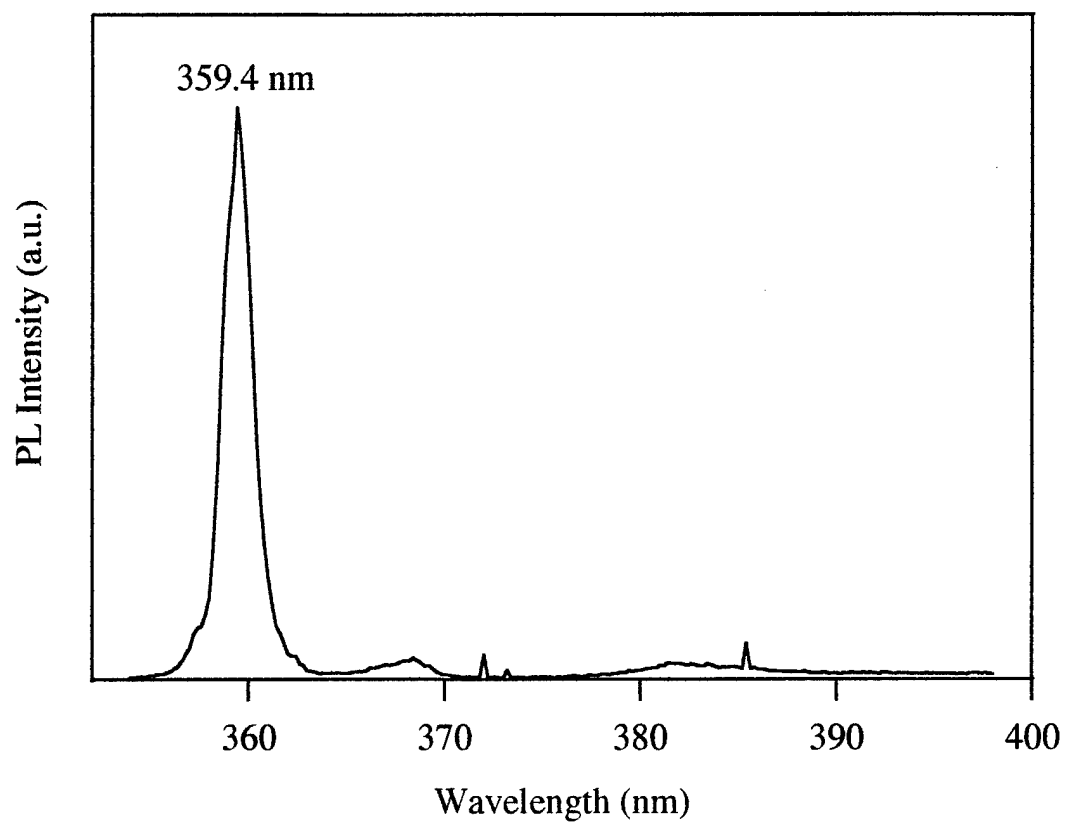


Figure 5. Photoluminescence of GaN at 4.2K.

using helium as a diluent support this argument by duplicating the results obtained using nitrogen diluents, suggesting it is the chemical nature of hydrogen, rather than the diffusion or heat transfer properties of nitrogen, that causes the difference [13].

All of the InGaN films characterized were approximately 1000Å grown on a 5000Å GaN underlayer. $\text{In}_x\text{Ga}_{1-x}\text{N}$ films were grown with x as large as 0.22. Figures 6 and 7 are PL spectra for InGaN films at room temperature and 12K, respectively. At room temperature the PL spectra have appreciable deep levels, which disappear at 12K with a noticeable increase in the near-band-edge emission. The emission at 418.5 nm in Figure 6 corresponds to an indium mole fraction of 0.22, while the emission at 405.5 nm corresponds to an indium mole fraction of 0.18 [2]. Figure 8 is a cross sectional TEM micrograph showing the InGaN film on the GaN. The interface is clean, with few threading dislocations generated at the interface. From the TEM, the surface of the InGaN is smooth, however, in SEM small pits can be seen, which may be a result of the surface of the GaN underlayer. With the improvement of the InGaN microstructure, as well as the GaN underlayer, the photoluminescence of the films should improve, providing device-quality material.

D. Conclusions

The growth of GaN and InGaN thin films on $\alpha(6\text{H})\text{-SiC}(0001)$ using a high temperature AlN buffer layer has been investigated. SEM and TEM of the GaN films show a smooth surface with a relatively low dislocation density of $1\text{e}9\text{ cm}^{-2}$. The near-band-edge photoluminescence peak occurs away from the relaxed value for GaN, possibly indicating strain in the film or near band-edge defect levels. Si doping of GaN was achieved, with doping levels between $5\text{e}16\text{ cm}^{-3}$ and $3\text{e}18\text{ cm}^{-3}$. Gallium nitride growth in hydrogen and nitrogen were compared, with two main differences being photoluminescence intensity and growth rate. InGaN films were grown with an In fraction of up to 0.22. Narrow and bright luminescence was observed both at room temperature and 12K. Cross sectional TEM shows a clean interface between the GaN and InGaN, with few threading dislocations being generated at the interface.

E. Future Research Plans and Goals

Future research includes optimizing the growth of GaN in both hydrogen and nitrogen diluents. p-type doping using Zn and Mg will be investigated. Further research of the InGaN compounds will focus on increasing film quality and the indium mole fraction. Quantum well structures using InGaN active layers will be grown. High speed microelectronic device structures will also be grown and characterized. Finally, quaternary alloys will be investigated in an effort to grow lattice-matched device structures.

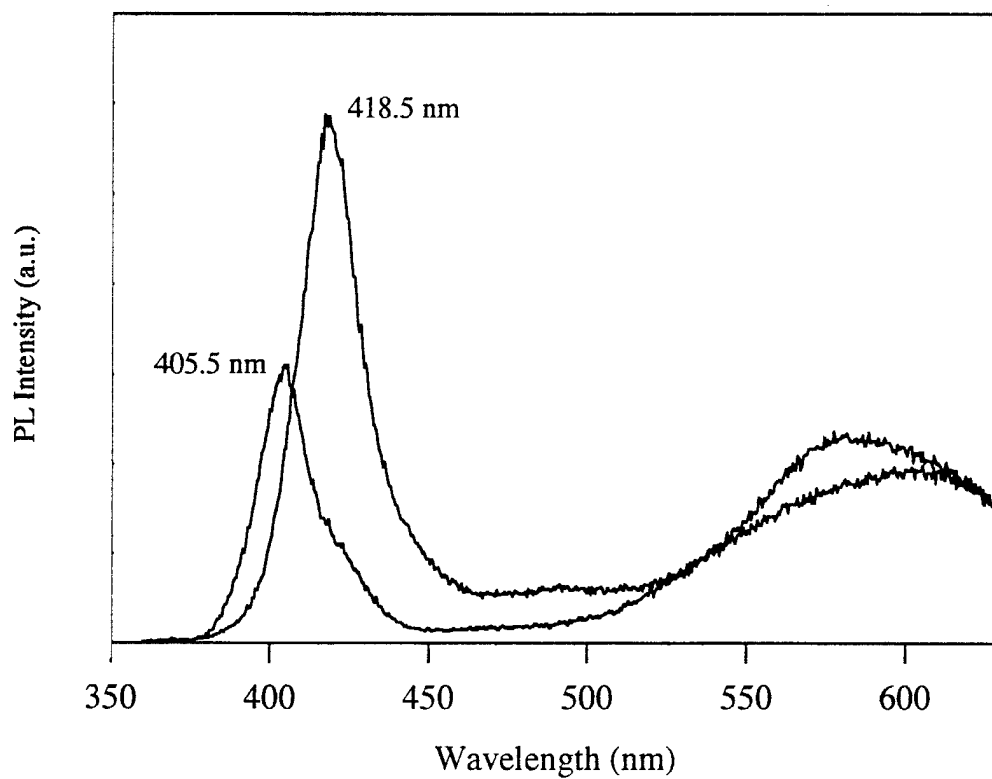


Figure 6. RT PL of $\text{In}_x\text{Ga}_{1-x}\text{N}$, $x = 0.18$ and 0.22 FWHM for $x=0.22$ is 82 meV .

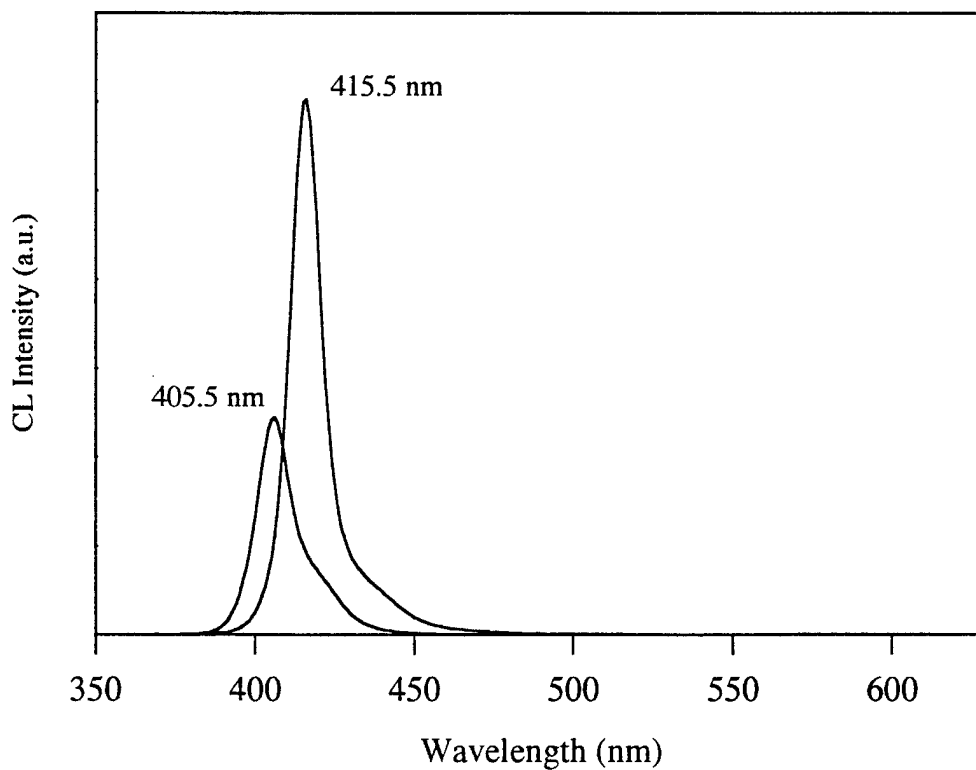


Figure 7. 12K CL of InGaN . $x = 0.18$ and 0.22 .

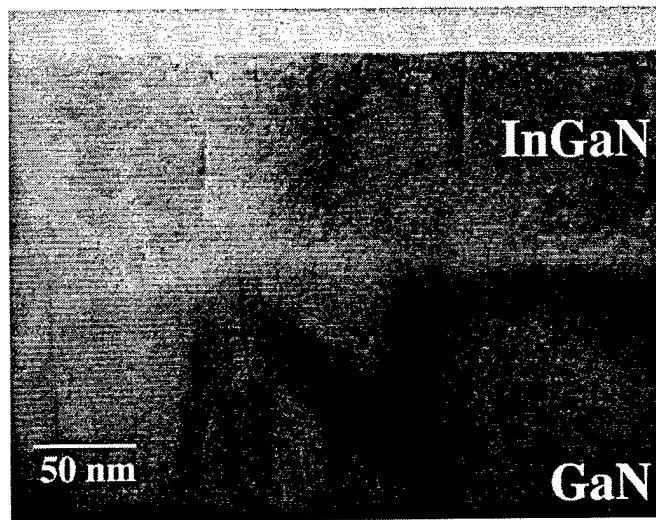


Figure 8. Cross Sectional TEM of $\text{In}_{0.22}\text{Ga}_{0.78}\text{N}$ on GaN.

F. References

1. S. Nakamura, T. Mukai, and M. Senoh, *Appl. Phys. Lett.* **64** (13), 1687 (1994).
2. S. Nakamura, *J. Cryst. Growth* **145**, 911 (1994).
3. M. A. Khan, Q. Chen, R. A. Skogman, and J. N. Kuznia, *Appl. Phys. Lett.* **66** (16), 2046 (1995).
4. S. Nakamura, T. Mukai, and M. Senoh, *J. Appl. Phys.* **76** (12), 8189 (1994).
5. S. Nakamura, M. Senoh, N. Iwasa and S. Nagahama, *Jpn. J. Appl. Phys.* **74**, L797 (1995).
6. S. Nakamura, M. Senoh, N. Iwasa, S. Nagahama, T. Yamada and T. Mukai, *Jpn. J. Appl. Phys. Lett.* **34**, L1332 (1995).
7. S. Nakamura, M. Senoh, S. Nagahama, N. Iwasa, T. Yamada, T. Matsushita, H. Kiyoku, and Y Sugimoto, *Appl. Phys. Lett.* **68**, 2105 (1996).
8. S. Nakamura, M. Senoh, S. Nagahama, N. Iwasa, T. Yamada, T. Matsushita, Y. Sugimoto, and H. Kiyoku, *Appl. Phys. Lett.* **69**, 1477 (1996).
9. Nitride Semiconductors for Ultraviolet Detection, Semiannual Report, 1994.
10. T. W. Weeks, M. D. Bremser, K. S. Ailey, E. Carlson, W. G. Perry, and R. F. Davis, *Appl. Phys. Lett.* **67** (3), (1995).
11. W. Qian, M. Skowronski, M. De Graef, K. Doverspike, L. B. Rowland, and D. K. Gaskill, *Appl. Phys. Lett.* **66** (10), 1252 (1995).
12. K. Jensen, *Microelectronics Processing: Chemical Engineering Aspects*; American Chemical Society, Washington, DC, (1989).
13. M. Weckwerth, K. Killeen, R. Biefeld, T. Drummond, M. Crawford and J. Zolper, EMC, Santa Barbara, Session CC: Growth and Processing of III-V Nitrides, June 1996.
14. E. Piner, J. Roberts, G. McIntosh. Private Communication.

VII. Correlation of Biaxial Strains, Bound Exciton Energies, and Defect Microstructures in GaN Films Grown on AlN/6H-SiC(0001) Substrates

A. Introduction

Mismatches in the lattice parameters (a and c) and the coefficients of thermal expansion (α) exist between heteroepitaxial GaN films and all of the presently used substrates. These mismatches result in interfacial biaxial strain which leads to misfit dislocations and associated threading defects that degrade film quality. Measurement and analysis of these strains have been the goals of the research reported herein.

The most common substrate used for GaN film growth is sapphire (0001). Buffer layers of AlN and GaN have been used to improve GaN film quality, although significant mismatches in the lattice parameters between these layers and sapphire exist ($\Delta a/a_0 \approx 13.6$ and 16.1% , respectively, see Table I). The resulting lattice mismatch strain is compressive for both GaN on AlN and GaN on sapphire and alters the values of both a (decreases) and c (increases) of the films [1,2]. Hiramatsu *et al.*[3] have assumed this strain to be relieved after several nanometers of growth according to the critical thickness theory. The primary relief mechanism is the formation of dislocations at the film/substrate interface during film growth. Upon cooling, the difference in thermal expansion coefficients ($\alpha_{\text{sapphire}} > \alpha_{\text{AlN}} > \alpha_{\text{GaN}}$) results in additional compressive stresses which are often assumed [1,4] to be wholly responsible for the observed compressive strain. However, high resolution transmission electron microscopy (HRTEM) analysis of the GaN/AlN interface on sapphire [5] suggests that the lattice mismatch stress in GaN is not fully relieved. This residual stress was assumed [5] to be accommodated elastically and to give rise to biaxial stresses in the GaN films. However, it is difficult to substantiate this through other characterization techniques since both thermal and lattice mismatch stresses are compressive, and there is a marked variation in published thermal expansion coefficients that could be used in calculations. Moreover, none of these coefficients applies to temperatures above 900°C , where most GaN thin films are deposited.

Recent work [6,7] has used a SiC(0001) substrate/AlN(0001) buffer layer combination. The lattice mismatch strains at both the GaN/AlN and AlN/SiC interfaces are compressive ($a_{\text{GaN}} > a_{\text{AlN}} > a_{\text{SiC}}$), but the reduced lattice mismatch between AlN and SiC ($\sim 1\%$) compared to AlN and sapphire leads to improved GaN film quality. This mismatch is expected to be at least partially relieved by the formation of misfit dislocations, as the calculated critical thickness for AlN(0001) on SiC(0001) is only 47\AA [8]. The differences in thermal expansion coefficients are opposite in sign ($\alpha_{\text{GaN}} > \alpha_{\text{SiC}} \approx \alpha_{\text{AlN}}$) to that for GaN on sapphire and result in a biaxial tensile stress contribution. Hence, the two main stresses in the GaN/AlN/SiC heteroepitaxial

system are opposite in sign, which offer the potential to substantiate if residual lattice mismatch stress exists through lattice parameter measurements and other techniques. Li and Ni [9] measured the lattice parameters for thick GaN films grown directly on both SiC(0001) and sapphire(0001). They observed that the film on SiC was in tension while that on sapphire was in compression. They attributed this variation in strain to the difference in thermal expansion coefficients between the two substrates.

Table I. Comparison of III-Nitride Material Properties with 6H-SiC and Sapphire^a.

Material	Lattice Parameter at RT(Å)	In-Plane Mismatch with GaN (%)	Coefficients of Thermal Expansion (10 ⁻⁶ /K)
GaN	$a=3.1891^b$ $c=5.1855^b$	---	5.59; 3.1,6.2 ^d 7.75 ^c ; 2.8,6.1 ^d
AlN	$a=3.112$ $c=4.982$	2.5	4.15 5.27
6H-SiC	$a=3.08$ $c=15.12$	3.5	4.2; 3.2,4.2 ^d 4.68; 3.2,4.0 ^d
Sapphire	$a=4.758$ $c=12.99$	16.1	7.5; 4.3,9.2 ^d 8.5; 3.9,9.3 ^d

^aLandolt-Börnstein, edited by O. Madelung (Springer, New York, 1982), Vol. 17.

^bC. M. Balkas, C. Basceri, and R. F. Davis, Powder Diffraction 10 266 (1995).

^cProperties of Group III Nitrides, edited by J. H. Edgar (INSPEC, London, 1994).

^dM. Leszczynski, T. Suski, P. Perlin, H. Teisseyre, I. Grzegory, M. Bockowski, J. Jun, S. Porowski, J. Major, J. Phys. D: Appl. Phys. 28 A149 (1995), For T =300-350 K and 700-750 K, respectively.

One consequence of film strain is a shift in the band-gap energy (E_g) [10]. The biaxial strain can be viewed as an isotropic cubic component together with a uniaxial component along the c -axis of the GaN film [11]. The cubic, or hydrostatic term influences the band gap directly, while the uniaxial component introduces subtle shifts between individual lines in the spectrum. However, it is difficult to measure E_g directly in GaN due the strong excitonic features at the absorption edge [12]. Changes in E_g may be detected by shifts in these excitonic features using low temperature photoluminescence (PL). At $T \leq 4.2$ K the PL of high-quality GaN reveals intense near-band edge emission attributed to the recombination of both free excitons and/or excitons bound to shallow neutral donors [4,6,7,12,13]. The bound exciton feature is often the dominant feature due to the nature of GaN, which is always n -type for undoped films. The identity of the shallow donor(s) is unknown, although recent work suggests that both native defects and extrinsic impurities are possibilities [14-16]. Amano, *et al.* [1] observed a shift of the bound exciton energy (E_{BX}) to higher energies that was attributed to biaxial compressive

strain for GaN films deposited on sapphire(0001). Reported E_{BX} values range from 3.467 to 3.494 eV for GaN on sapphire [12,13,17,18], and from 3.463 to 3.472 for GaN on SiC [4,6,7,18,19]. The disparity between the two energy ranges has been attributed to the difference in thermal expansion coefficients of the two substrates [4,18].

In this research, the relationship between E_{BX} and lattice parameters (and hence strain) was determined for 22 GaN films grown on AlN buffer layers previously deposited on 6H-SiC(0001). A value of E_{BX} for relaxed GaN was determined. Poisson's ratio was calculated from lattice parameter measurements and used to determine the shift of E_{BX} with biaxial stress (σ_a). The roles of the AlN buffer layer and the tilt of the SiC substrate on film stress and the associated PL spectra were also determined. Transmission electron microscopy (TEM) was employed to compare and contrast the crystal structure of GaN films grown on the vicinal (off-axis) and on-axis SiC wafers. The GaN/AlN interface was analyzed via high resolution (HR)TEM to determine if any residual lattice mismatch stress occurred.

B. Experimental Procedures

The GaN/AlN films were grown in an organometallic vapor phase epitaxial (OMVPE) system described previously [6,7] on both on-axis and vicinal (2-4° off-axis) 6H-SiC(0001) substrates. The GaN films ranged in thickness from 0.3-3.7 μm and were grown at temperatures ranging from 950-1100°C. The AlN buffer layer for each sample was 1000 Å thick and grown at 1100°C. All of the GaN films were unintentionally doped, with *n*-type carrier concentrations ranging from $<1 \times 10^{16}$ – $1 \times 10^{17}/\text{cm}^3$.

Absolute lattice constants values were measured using a Philips X'Pert MRD X-ray diffractometer in the triple-axis mode. The technique used was originally proposed by Fewster [20], and is comparable to, and in many ways more accurate than, the commonly used "Bond" method. The high resolution of the triple-bounce analyzer crystal and the steps taken to eliminate inaccuracies due to the 2θ zero error and sample centering account for this. The data were collected using 2θ - ω scans, with corrections made for refraction. The accuracy of the lattice parameters measured using this system was 0.0002 Å. The *c*-axis lattice parameter (*c*) was measured using the (002) reflection. Measurements of the *a*-axis lattice parameter (*a*) were made using both the (002) and (015) reflections; however, the low count rate for the asymmetric reflections limited the number of samples that could be measured accurately.

Photoluminescence (PL) measurements of the GaN films on SiC were made at 4.2 K using a He-Cd laser ($\lambda=325$ nm) as the excitation source, unless otherwise noted. TEM studies were performed using a TOPCON EM - 002B HRTEM, operated at 200 kV with a point-to-point resolution of 0.18 nm. The cross-sectional samples in the $[11\bar{2}0]$ orientation were prepared by conventional techniques using mechanical grinding and polishing, and Ar⁺ ion-milling at a low angle in the final stage [21, 22].

PL/XRD Analysis. Low temperature PL of the GaN(0001) films grown in this research exhibited strong near-band-edge emission due to the recombination of both free and donor-bound excitons, as shown in the spectrum from a 3.7 μm thick film in Fig. 1. The emission from the donor-bound exciton (BX) decreased in intensity much faster than that from the free excitons (FX) as the temperature was increased from 10 to 100 K. This behavior is due to the small localization energy (E_b) of the donor-bound excitons compared to the binding energy of the free excitons (E_x). From this data E_b was estimated to be 5.9 meV, which agrees favorably with earlier measurements [7,13]. Recent work on this and other samples measured E_x to be 21 ± 1 meV for the A- and B-free excitons [23], although earlier work suggested a higher (26 meV) value [13]. The PL of the GaN films in this study was dominated by the bound exciton emission, and its dependence on lattice strain as manifest in changes in lattice parameters will be described below.

The bound exciton energies (E_{BX}) determined at 4.2 K as a function of the c-axis lattice parameter (c) for 22 GaN films on SiC are shown in Fig. 2. The lattice parameter measurements were performed at room temperature. It is expected that the tensile strain in the

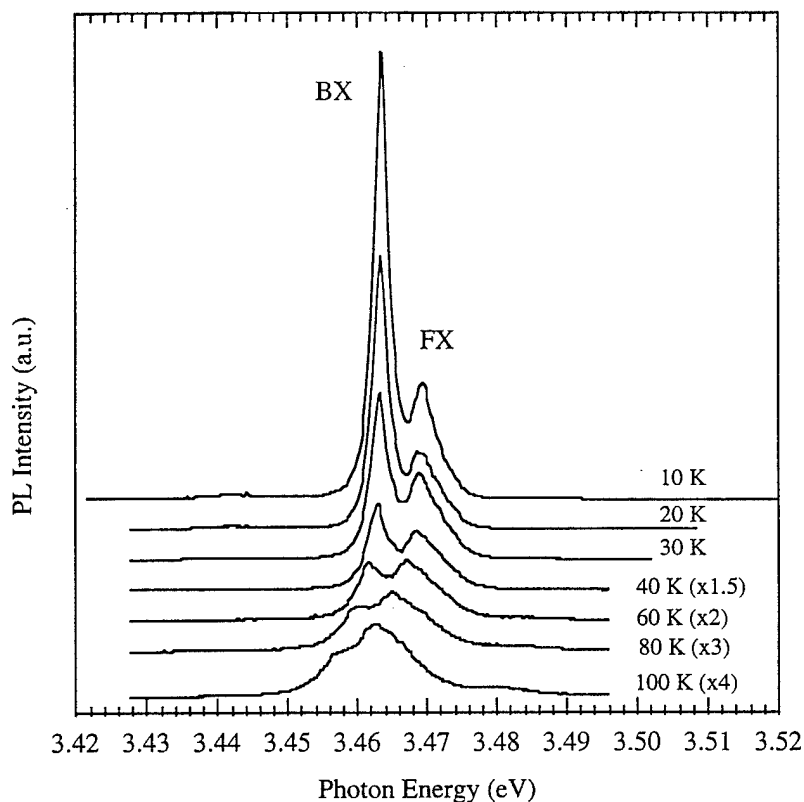


Figure 1. PL of a 3.7 μm thick GaN film on an AlN buffer layer previously grown on a SiC(0001) wafer at 10, 20, 30, 40, 60, 80 and 100 K. The peaks labeled BX and FX are due to the recombination of bound and free excitons, respectively.

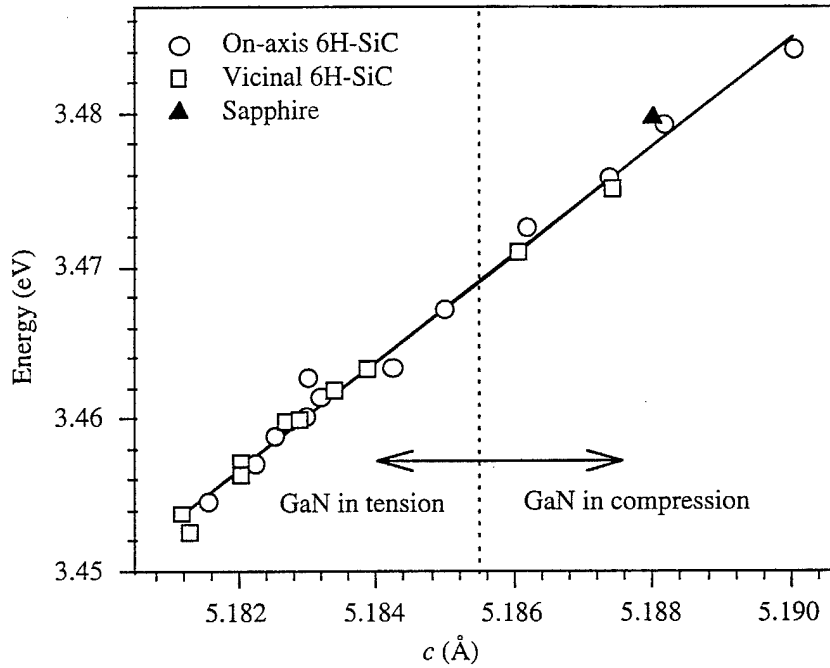


Figure 2. Lattice constant c vs. the bound exciton energy (E_{BX}) for GaN/AlN/SiC. The PL was performed at 4.2 K and the lattice parameter measurements at room temperature. The dashed line indicates the relaxed value of C_0 (5.1855 Å) for GaN. A data point for GaN grown on sapphire is included.

GaN films due to thermal expansion mismatch will increase as the temperature is decreased from room temperature to 4.2 K, but lattice parameter measurements are not possible at these temperatures. A linear relationship between the c and E_{BX} was observed, where the bound exciton peak shifted to lower energies as c decreased. Any change in c is in response to a strain (ϵ_a) along the a -axis (a), $\Delta a/a_0$, which results from the biaxial stress produced in the plane of the film by residual stresses. Thus a decrease in the value of c indicates that the biaxial tensile strain in the film is increasing, which causes E_g to decrease and E_{BX} to shift to lower energies.

The value of c for relaxed GaN has recently been measured to be 5.1855 Å [24]. As shown in Fig. 2, six of the GaN films grown on SiC(0001) have values of c greater than this, which indicates they are compressively strained. This suggests that the compressive strain due to lattice mismatch has not been fully relieved by defect formation in these samples. The highest value of c observed was 5.190 Å, and the bound exciton energy for this sample was 3.484 eV. The highest reported E_{BX} value previously reported for GaN grown on 6H-SiC was 3.472 eV [19]. The n -type carrier concentration of this film was reported to be $1 \times 10^{18} \text{ cm}^{-3}$; thus it is possible that this value was slightly shifted to higher energies by the Burstein-Moss [25] effect rather than by strain. The free carrier concentration for the samples in this study was less than $1 \times 10^{17} \text{ cm}^{-3}$; therefore, it is assumed that the shift observed in E_{BX} in this study was not due to this effect.

Values of E_{BX} can be estimated from a linear regression of the data in Fig 2, which yielded $E_{BX} = (-14.91 + 3.545 \cdot c) \text{ eV}$, where c is in angstroms. Using this relationship E_{BX0} was predicted to be 3.469 eV for relaxed GaN. This compares favorably to reported values of 3.467, [26] 3.469, [27] and 3.472 eV[28]. The marked dependence of the values of E_{BX} on c indicated that the wide range of energy values reported for the donor-bound exciton in the literature are due primarily to different amounts of strain present in the films. For GaN on sapphire, typical E_{BX} values are between 3.467-3.494 eV, which are predominantly in the energy range indicated for films under compression in this study. Included in Fig. 2 is a data point for a 4.7 μm GaN film grown on sapphire, which indicated that E_{BX} can be predicted for GaN grown on any substrate using values of c and the relationship determined in this study.

For biaxially strained wurtzitic films the relationship between the lattice parameters c and a is given by the strain ratio [29],

$$\epsilon_c/\epsilon_a = (\Delta c/c_0)/(\Delta a/a_0) = -2\nu/(1-\nu), \quad (1)$$

where ν is Poisson's ratio and a_0 and c_0 are the relaxed lattice parameters. For GaN, values of ν which range from 0.372 [30] to 0.20 [31] have been calculated using anisotropic elastic constants. A recent survey [32] of x-ray data available in the literature determined $\nu = 0.23 \pm 0.06$ for samples dominated by biaxial strain. In this study a and c were measured simultaneously for 22 GaN films on 6H-SiC, including 10 of those shown in Fig. 2. The relationship between a and c is displayed in Fig. 3. Also included is a data point for the 4.2 μm GaN film on sapphire included in Fig. 2. An average strain ratio of $\epsilon_c/\epsilon_a = -0.455$ was determined for this data set using values of 3.1891 Å and 5.1855 Å for a_0 and c_0 , respectively [28], which resulted in a Poisson's ratio of $\nu = 0.18$. Further analysis showed that remarkably different strain ratios of $\epsilon_c/\epsilon_a = -0.33, -0.47$, and -0.59 were calculated from the same data using other published values for a_0 and c_0 . [32,2,33] This disparity in the strain ratios was due to individual values of c and a that were close to the different values for a_0 and c_0 which resulted in abnormal values in the nominator and/or denominator of equation (1) for that sample's strain ratio. A distortion of the average strain ratio for the data set resulted.

Given this wide variation in the calculated strain ratios two methods were used to obtain a more reasonable estimation of the strain ratio and the resulting Poisson's ratio. The first eliminated those data points (4 total) that had adverse effects on the average strain ratio of the data set. An average strain ratio was then calculated using each of the four sets of published values for a_0 and c_0 [28,32,2,33] and averaged to give a strain ratio $\epsilon_c/\epsilon_a = -0.425$. The corresponding Poisson's ratio was $\nu = 0.18$. The second method fit a line to the data in Fig. 4, and then used the experimentally determined values of c to calculate values of a that fit the line. The strain ratio for each point was then calculated using values of $c_0 = 5.1850$ and $a_0 = 3.1891$,

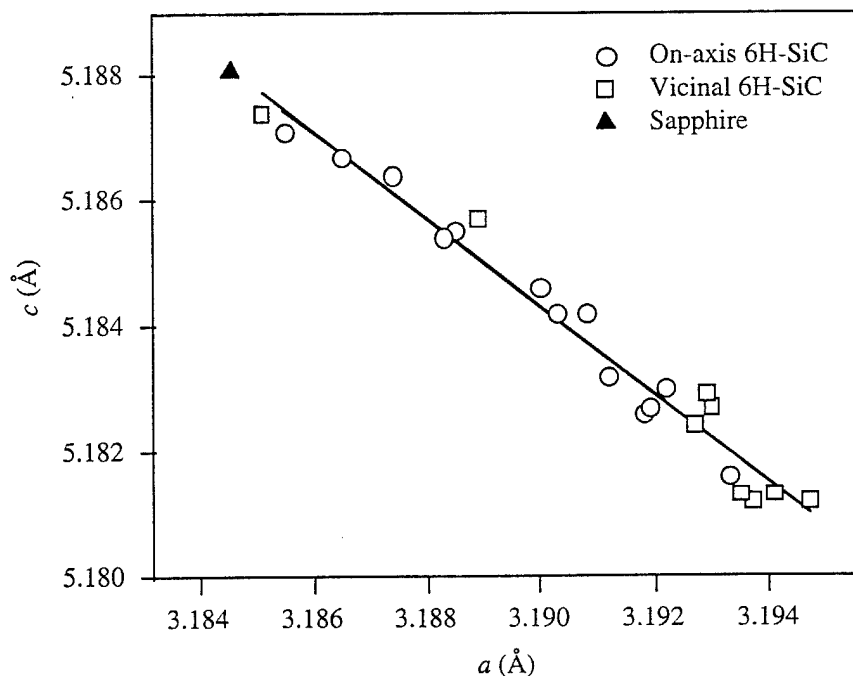


Figure 3. Lattice constant a vs. c for GaN/AlN/SiC. The lattice parameter measurements were performed at room temperature. The Poisson's ratio calculated using this data as $\nu = 0.18 \pm .02$.

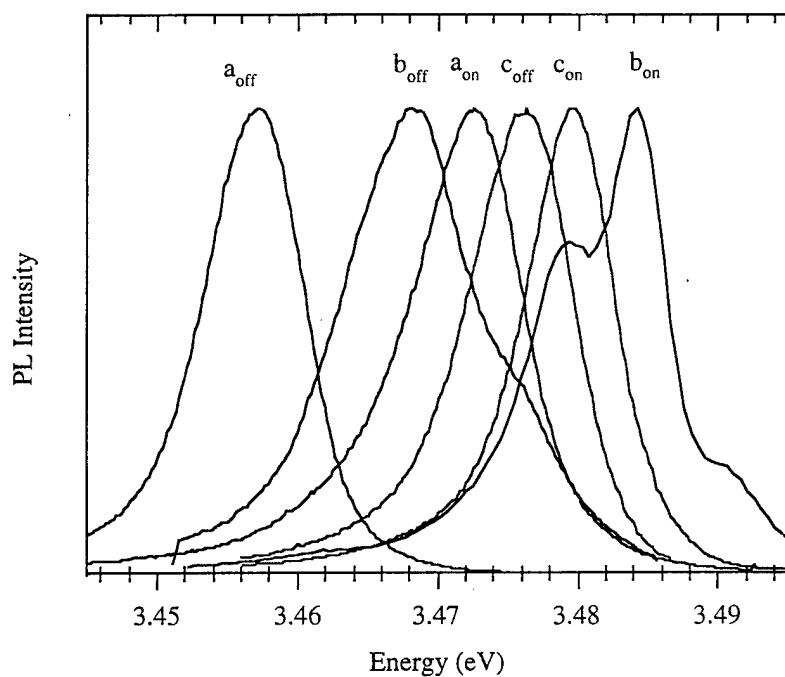


Figure 4. PL at 4.2 K of three sets of GaN films (a, b, c) grown concurrently on vicinal (off-axis) and on-axis SiC. The off-axis tilt of sample c is $\sim 2^\circ$, which is lower than a tilt of $3-4^\circ$ that is typical for the vicinal wafers.

where the latter value was determined from the line fit to the data in Fig. 4. The average strain ratio using this method was $\epsilon_c/\epsilon_a = -0.446 \pm .03$, which resulted in a Poisson's ratio of $\nu = 0.18 \pm .02$. The two calculated values of Poisson's ratio were identical, and they compared favorably with values determined from x-ray data ($0.23 \pm .06$ [32]) and anisotropic elastic constants (0.20 [31], 0.24 [34] and 0.26 [35]).

The shift of E_{BX} as a function of the biaxial film stress ($\Delta E_{BX}/\Delta\sigma_a$) can be estimated from the data in Fig. 2 using the relationship [29],

$$\sigma_a = Y/(1-\nu)\epsilon_a = -Y\epsilon_c/2\nu, \quad (2)$$

where Y is the Young's modulus (290 ± 20 GPa). [32] The first step was to calculate $\Delta E_{BX}/\Delta\epsilon_c$ from the data in Fig. 2, where relaxed values of $E_{BX0} = 3.469$ eV and $c_0 = 5.1855$ Å were assumed. A linear regression of the data yielded $\Delta E_{BX}/\Delta\epsilon_c = 18.1$ eV. Using this expression, and the previously determined Poisson's ratio of $\nu = 0.18$, a value of $dE_{BX}/d\sigma_a = 23$ meV/GPa was calculated. This result is lower than that reported previously for hydrostatic pressure experiments (39 [36] and 40 [37] meV/GPa), but it compared favorably to results for GaN films where biaxial stress was assumed 27 [32,38] meV/GPa). However, the similarity of the value given in Ref. [38] with that determined in this research may be a coincidence given that the authors assumed the wrong relationship between stress and strain. It should be noted that uncertainties in Poisson's ratio and Young's Modulus can have a dramatic effect on these calculations.

The role of SiC off-axis tilt on GaN film stress was investigated using films grown concurrently on off- and on-axis SiC(0001) wafers. Previous analysis in this laboratory of 1.4 µm GaN/AlN films deposited simultaneously on vicinal and on-axis 6H-SiC(0001) substrates showed the microstructural quality of the GaN and AlN layers on the on-axis substrate to be superior [7]. Moreover, double crystal x-ray curve (DCXRC) measurements showed a FWHM of 58 arcsec for the on-axis film, compared to 151 arcsec for the vicinal film. Plan view TEM measurements showed a lower dislocation density for a GaN film on the on-axis SiC, and the AlN buffer layer was of high microstructural quality. The bound exciton energy of the vicinal film was shifted to a lower energy relative to the on-axis film, with $\Delta E_{BX} = 3$ meV.

The PL spectra of the bound exciton emission from three separate GaN film sets grown concurrently on off- and on-axis SiC are displayed in Fig. 4, where the film thickness was ≤ 0.6 µm for all of the samples. In each case the BX emission on the vicinal wafers was shifted to lower energies, with ΔE_{BX} as large as 17 meV. A related shift in the lattice parameter c was observed, with Δc as great as 0.0072 Å. Thus the GaN films grown on vicinal SiC were compressively strained compared to those grown on on-axis SiC. The disparity in E_{BX} and c values persisted as the film thickness increased. However, ΔE_{BX} decreased, and E_{BX} for both

types of films shifted to energies commonly associated with GaN on 6H-SiC(0001) ($E_{\text{BX}} \geq 3.469$ eV). It should be noted that the values of c for the underlying vicinal and on-axis 6H-SiC were identical at the AlN/SiC interface, which indicated that the phenomena discussed is not due to differences in the lattice constants of the substrates.

TEM/HRTEM Analysis. To understand these results it is necessary to examine the defect microstructures of GaN films grown on an AlN buffer on 6H-SiC(0001) substrates. The primary defects in the AlN buffer layers grown on the off-axis SiC substrates were domains and their associated domain boundaries, as shown by HRTEM in Fig. 5 and lower magnification TEM in Figs. 6(a) and (b). Recent studies [39] show that the steps on the vicinal surface provide sites for the growth of inversion domains, which are separated by inversion domain boundaries (IDBs). These defects introduce a marked amount of strain in the AlN buffer layer grown on off-axis SiC substrate. There is also a high density of threading dislocations in the buffer layer.

By comparison, the crystal quality of AlN films grown on on-axis SiC substrate is of improved crystalline quality, as shown by HRTEM in Fig. 7 and TEM in Fig. 8. Most significantly, there is a reduced density of inversion domain boundaries due to the reduction in the density of SiC steps. The primary defects are stacking faults parallel to the AlN/SiC interface and associated partial dislocations. Threading dislocations running from the top to the bottom of the film are also present.

The crystal quality of the GaN is directly influenced by the AlN buffer. The inferior quality of the AlN buffer layer grown on vicinal SiC results in a high dislocation density ($\sim 10^9$ – $10^{10}/\text{cm}^2$) at the interface, as determined from plan-view TEM analysis by counting the number of dislocations per unit area. The dislocation density decreases markedly about two hundred angstroms away from the GaN/AlN interface. The predominant defects are threading dislocations and threading segments that persist throughout the film. In addition stacking faults and dislocation loops are observed close to the interface. Finally, domain boundaries that originate at the GaN/AlN interface are also visible. It should be noted though that recent work has shown that the formation of domains can also be associated with non-stoichiometry or contamination of the AlN surface [40].

The improved quality of the AlN buffer layers on the on-axis SiC carries over into the GaN, as displayed in Fig. 8. A dislocation density in the order of $\sim 10^8/\text{cm}^2$ in the GaN layer was observed in plan-view TEM near the GaN/AlN interface. Most notably there are no planar defects such as stacking faults or domain boundaries in the GaN. The dominant defect in the on-axis GaN films are edge-type dislocations with burgers vectors $\mathbf{b} = 1/3\langle 11\bar{2}0 \rangle$ and $\mathbf{b} = 1/3\langle 1-100 \rangle$. These are the misfit dislocations which form at the GaN/AlN interface. This TEM analysis, as well as that of other [41] NCSU samples, reveal that the lattice mismatch

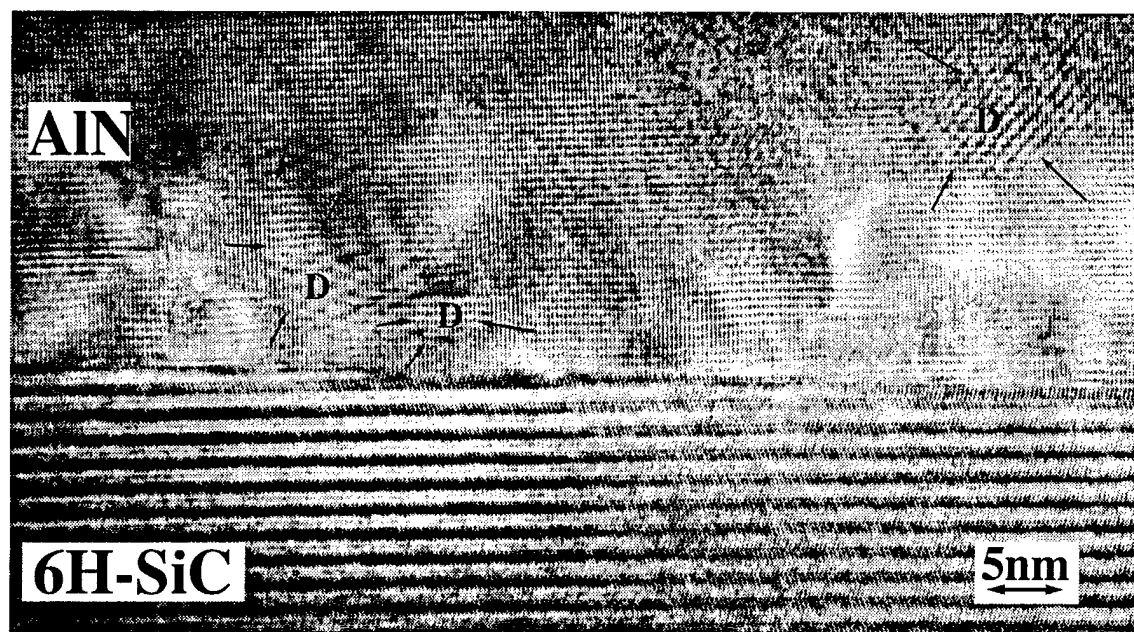
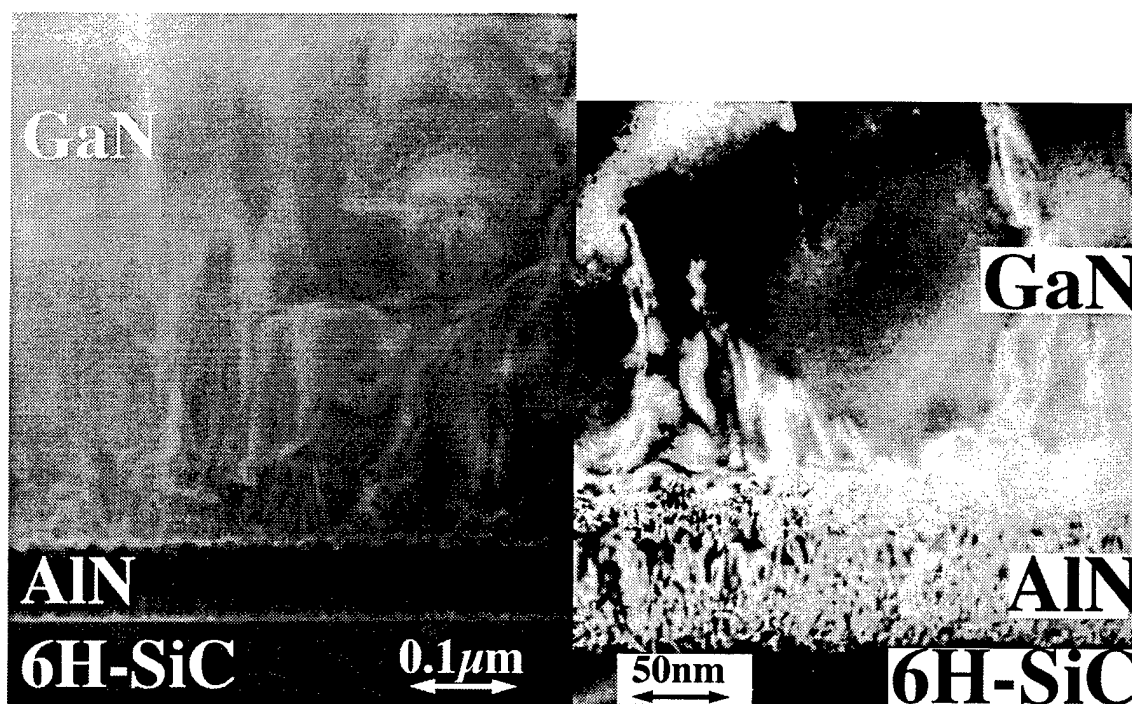


Figure 5. HR micrograph from an AlN/6H-SiC vicinal interface reveals that the strain at the interface is due to the numerous domain boundaries (denoted by D and the arrows) formed when neighboring grains coalesce during the growth process.



(a)

(b)

Figure 6. Low magnification TEM micrographs of a GaN/AlN/vicinal 6H-SiC(0001) heterostructure. (a) the AlN film exhibits domain type of growth with characteristic domain boundaries. Plan view of the GaN film reveals a dislocation density of $\sim 10^{10}$ - $10^{11}/\text{cm}^2$ comprised mostly of threading dislocations and threading segments. (b) The nonuniform contrast in the AlN film is due to the overlapping stress fields at the AlN/6H-SiC and GaN/AlN interfaces from the lattice parameters and coefficients of thermal expansion.

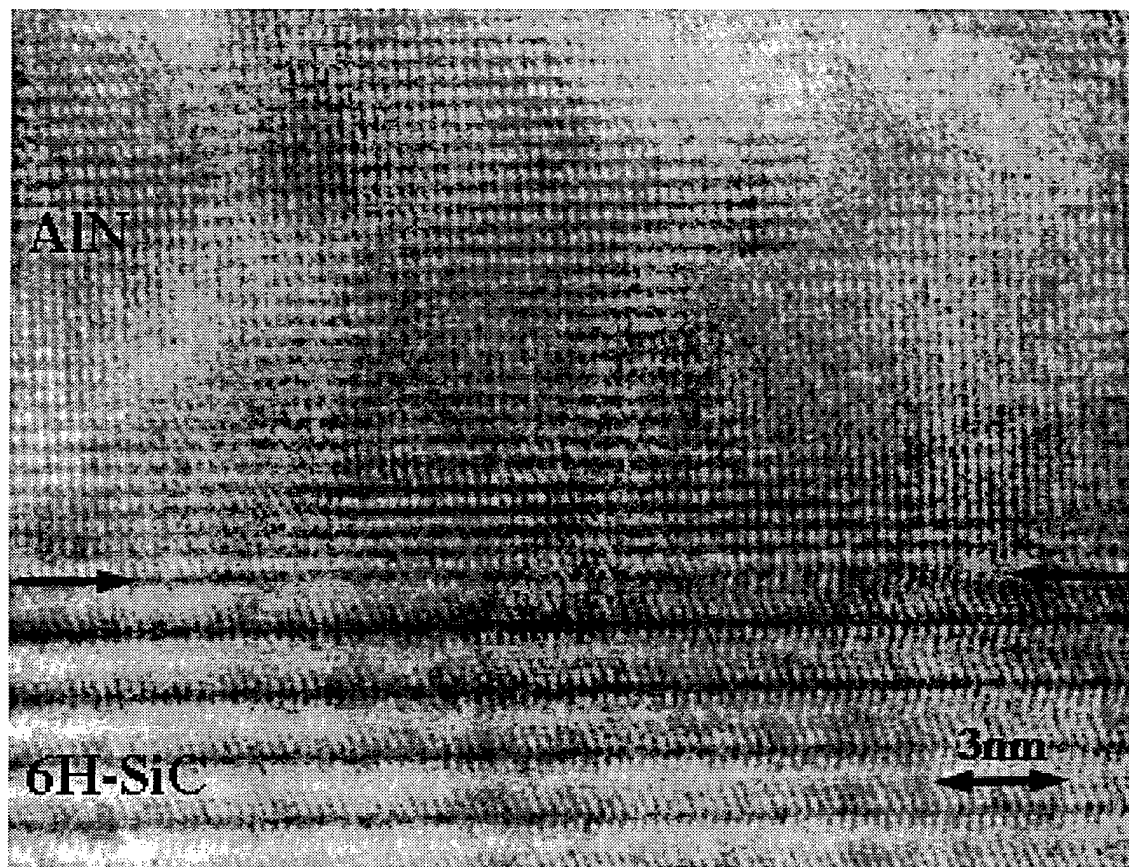


Figure 7. HRTEM micrograph from AlN on on-axis 6H-SiC(0001). There are no domains and associated domain boundaries as observed in the off-axis films shown in Fig. 5.

stress in GaN films grown on the on-axis SiC substrate is accommodated mostly by misfit dislocations. However, our PL, XRD and TEM studies suggest that these defects do not provide full stress relief.

In order to further assess the residual strain in the GaN films, HRTEM studies were performed at the GaN/AlN interface of the on-axis SiC in the $[11\bar{2}0]$ orientation, as shown in Fig. 9. It can be seen that the interface is epitaxial and free of domains, threading dislocations and low angle grain boundaries. Using HRTEM, it is possible to calculate the residual strain at the interface for planes that are perpendicular to the interface and parallel to each other. Ning, *et al.* [5], used this method to calculate the misfit at the GaN/sapphire interface, where they found a $\sim 1\%$ residual strain in the GaN film.

To determine the residual strain in the GaN films grown in the present research, the average lattice mismatch was calculated along the GaN/AlN interface from HRTEM micrographs in $[11\bar{2}0]$ GaN orientation, by counting the number of (1-100) GaN and AlN planes along $[1-100]$ direction that was bounded on each end by commensurate GaN and AlN planes. The

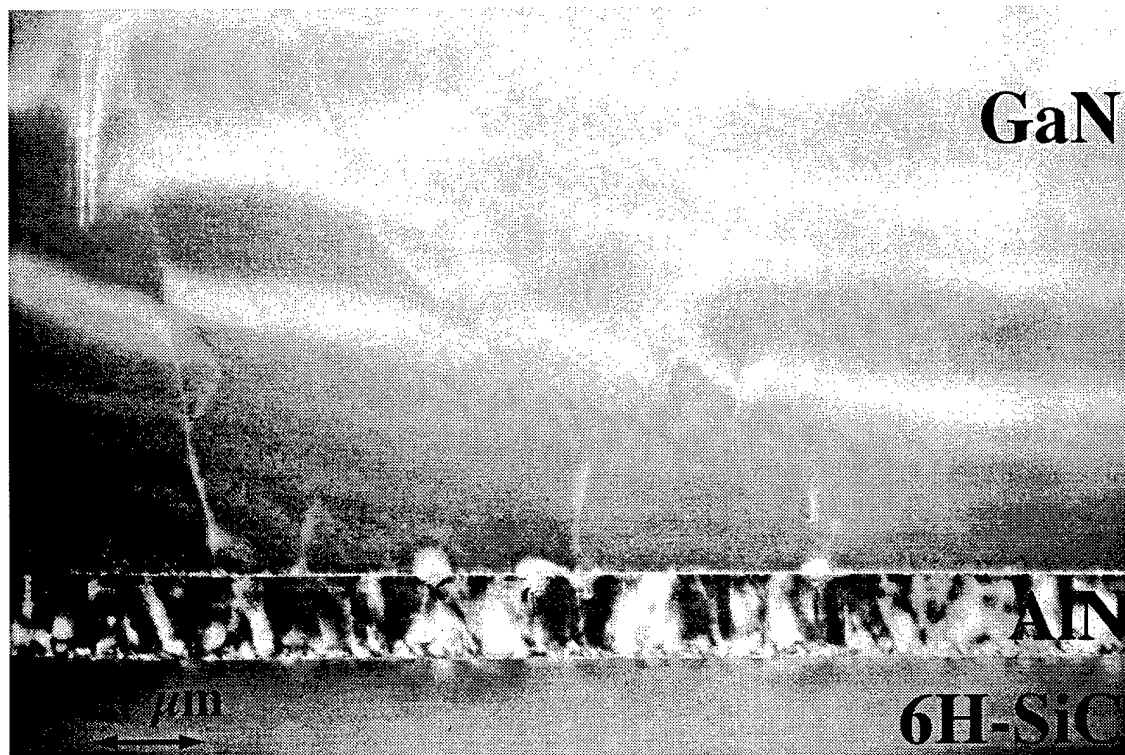


Figure 8. TEM micrograph from the GaN/AlN/on-axis 6H-SiC(0001) heterostructure in [11 $\bar{2}$ 0] orientation showing the considerably improved quality of the GaN/AlN and AlN/SiC interfaces relative to those achieved with the vicinal substrate (see Fig. 6a). Note also the reduction of the defect density in comparison with the structure grown on the off-axis SiC substrate.

experimental mismatch was assessed to be 0.9% lower than the theoretical misfit value of 2.5% for GaN and AlN. The experimental mismatch is equal to $N_{\text{GaN}} - N_{\text{AlN}}/N_{\text{AlN}}$, where N is the number of (1-100) planes perpendicular to the interface (Fig. 9). This calculation was repeated at ~ 20 different locations along the interface, with the average results presented here. Thus, there is a 0.9% residual compressive strain in the on-axis GaN film. This result supports the data from our PL and XRD studies presented earlier.

Additional evidence for the existence of residual compressive strain in the GaN films is the TEM contrast exhibited by the GaN films at distances of 50 - 80 Å from the interface with AlN. As can be seen in Fig. 9, the contrast reveals traces of rounded peaks and grooves, which are typical for films that are under compression [42,43]. Such near surface undulations are formed during heteroepitaxial growth by migration of the atoms deposited on the surface under the strain induced chemical potential gradients. From the same figure, it can be seen that at the grooves the interplanar distances are smaller than at areas close to the peaks. This shows that there is a complementary compression at the areas close to the peaks.

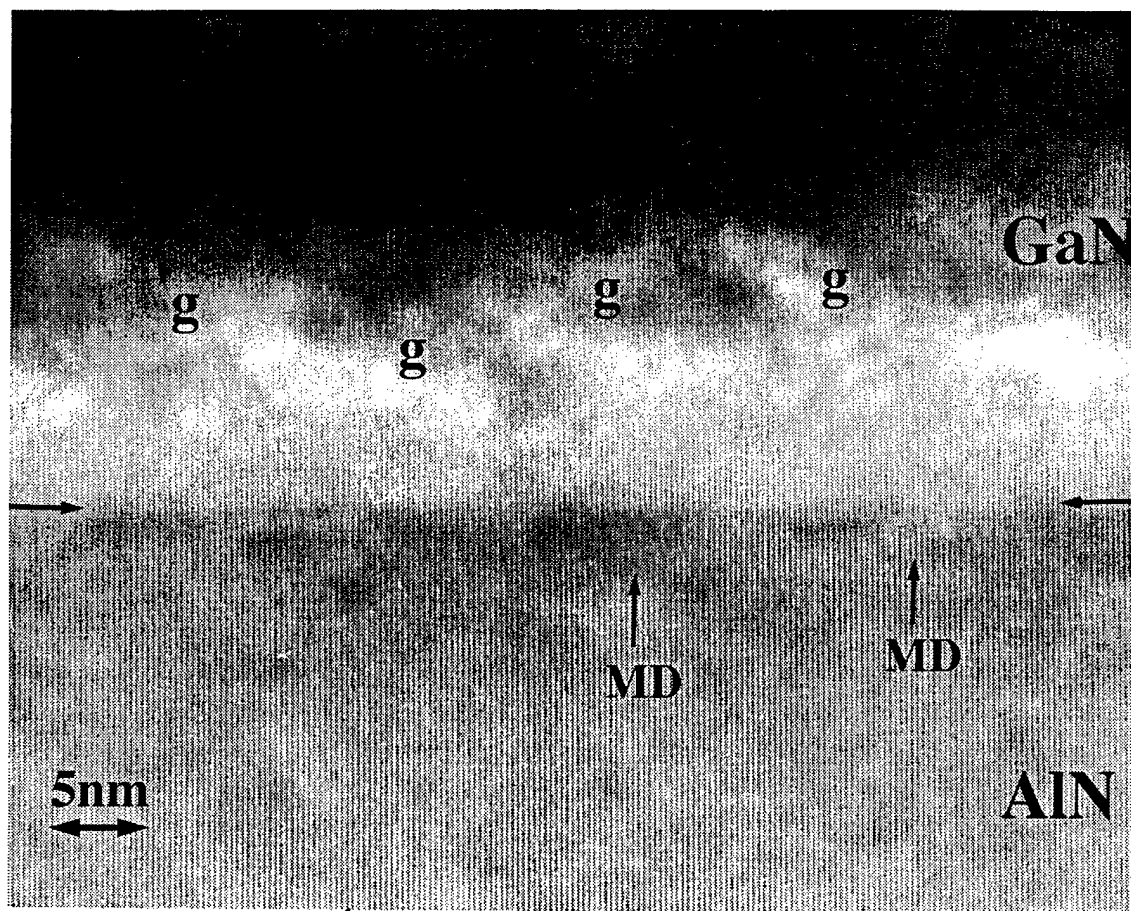


Figure 9. HRTEM micrograph from GaN/AlN interface of GaN/AlN 6H-SiC on-axis heterostructure. Note the extra-half planes in GaN films which are the misfit dislocations (MD) generated to relieve the misfit strain at that interface. The peaks and grooves are denoted by P and D.

Thus our HRTEM studies reveal the stress due to lattice mismatch is not fully relieved at the GaN/AlN for films grown on on-axis SiC. This results in a residual compressive stress that counteracts the tensile stress due to thermal mismatch. If this compressive stress is stronger then the GaN films should be in compression. This explains why the thin ($t \leq 0.6 \mu\text{m}$) GaN films grown on-axis films are in compression, while those grown concurrently on vicinal SiC wafers are in tension, with a maximum $\Delta c = 0.0072 \text{ \AA}$. As thickness increase ($t \geq 1 \mu\text{m}$) this compressive stress lessens, and at greater thicknesses ($t \geq 4 \mu\text{m}$) cracking may occur in the GaN to relieve thermal mismatch stress.

D. Conclusions

Compressive strain in GaN films grown on AlN/6H-SiC(0001) is reported for the first time. Residual biaxial strains determined in the films was due both to mismatches in thermal expansion coefficients and lattice parameters. A linear dependence due to this strain was

determined between E_{BX} and c for 22 GaN films grown on AlN/6H-SiC, and expressed by $E_{BX} = (-14.912 + 3.545 \cdot c)$ eV. Poisson's ratio for GaN was determined to be $\nu = 0.18$ from values of c and a for 22 GaN films. The shift of E_{BX} with biaxial film stress was estimated to be 23 meV/GPa. A marked variation in E_{BX} and c was observed for GaN films grown concurrently on AlN buffers and vicinal and on-axis SiC wafers. This variation was greatest for films ≤ 0.6 μm thick, where a maximum shift of $\Delta E_{BX} = 17$ meV and $\Delta c = 0.0072$ Å was observed, and the samples on the on-axis SiC were in compression.

Related TEM results showed a higher density of steps on the vicinal SiC wafers. These steps acted as formation sites for inversion domain boundaries (IDBs). Threading dislocation densities of $\sim 10^{10}/\text{cm}^2$ and $\sim 10^8/\text{cm}^2$ were observed for GaN on AlN grown vicinal and on-axis SiC, respectively. The on-axis SiC substrate did not contain sufficient steps for defect formation to fully relieve the lattice mismatch via defect formation at the GaN/AlN and AlN/SiC interfaces at the growth temperature. This resulted in residual compressive stresses that counteracts the tensile stresses that formed upon cooling due to the mismatch in thermal expansion coefficients. A 0.9% residual compressive strain at the GaN/AlN interface was calculated by comparing the average experimental lattice mismatch at the interface (1.6%) observed via HRTEM with that theoretically predicted for GaN/AlN (2.5%). It is proposed that this strain was accommodated elastically and resulted in biaxially compressive stresses in the films.

E. Future Research Plans and Goals

Raman Spectroscopy will be used to confirm that some of the GaN films in this study have compressive residual strain. The initial results are promising, and in the next report they will be presented in full detail. GaN films grown by other systems in our group, most notably MBE grown material, will be tested by PL and XRD to see if they fit the model presented for E_{BX} , as well as the calculation of Poisson's ratio. In addition, two additional GaN films on sapphire will be tested.

F. References

1. H. Amano, K. Hiramatsu, and I. Akasaki, *Jpn. J. Appl. Phys.* **27**, L1484 (1988)
2. Detchprohm, K. Hiramatsu, K. Itoh, and I. Akasaki, *Jpn. J. Appl. Phys.* **31**, (10B) L1454 (1992).
3. K. Hiramatsu, T. Detchprohm, and I. Akasaki, *Jpn. J. Appl. Phys.* **32**, 1528 (1993).
4. I. A. Buyanova, J. P. Bergman, B. Monemar, H. Amano, and I. Akasaki, *Appl. Phys. Lett.* **69**, 1255 (1996).
5. X. J. Ning, F. R. Cein, P. Pirouz, J. W. Yang, and M. A. Khan, *J. Mater. Res.* **11**, 580 (1996).
6. T. W. Weeks, M. D. Bremser, K. S. Ailey, E. Carlson, W. G. Perry, and R. F. Davis, *Appl. Phys. Lett.* **67**, 401 (1995).
7. T. W. Weeks, M. D. Bremser, K. S. Ailey, E. Carlson, W. G. Perry, E. L. Piner, N. A. El-Masry, and R. F. Davis, *J. Mater. Res.* **11**, 1011 (1996).

8. S. Tanaka, PhD dissertation, North Carolina State University, 1993.
9. W. Li and W. Ni, Appl. Phys. Lett. **68**, 2705 (1996).
10. S. Krishnankutty, R. M. Kolbas, M. A. Khan, J. N. Kunzia, J. M. Van Hove and D. T. Olson, J. of Electron. Mat. **21**, 609 (1992).
11. J. W. Orton, Semicond. Sci. Technol. **11**, 1026 (1996).
12. B. Monemar, J. P. Bergman, I. A. Buyanova, H. Amano, I. Akasaki, K. Hiramatsu, N. Sawaki, and T. Detchprohm, presented at the Topical Workshop on III-V Nitrides, Nagoya, Japan (1995).
13. C. Merz, M. Kunzer, U Kaufmann, I Akasaki and H. Amano, submitted to Phys. Rev. B., 1995
14. P. Boguslawski, E. Briggs, T. A. White, M. G. Wensell, and J. Bernholc, Mat. Res. Soc. Symp. Proc. **339**, 693 (1994).
15. J. Neugebauer and C. G. Van de Walle, Phys. Rev. B **50**, 8067 (1994).
16. P. Boguslawski, E. Briggs, J. Bernholc, Phys. Rev. B **51**, 17255 (1995).
17. W. Shan, R. J. Hauenstein, A. J. Fisher, J. J. Song, W. G. Perry, M. D. Bremser, R. F. Davis and B. G. Goldenberg, submitted to Phys. Rev. B
18. D. Volm, K. Oetinger, T. Streibl, D. Kovalev, M. Ben-Chorin, J. Diener, B. K. Meyer, J. Majewski, L. Eckey, A. Hoffman, H. Amano, I Akasaki, K. Hiramatsu, and T. Detchprohm, Phys. Rev. B **53**, 16543 (1995).
19. L. Eckey, J. C. Holst, P. Maxim, R. Heitz, A. Hoffmann, I. Broser, B. K. Meyer, C. Wetzl, E. N. Mokhoc, and P. G. Baranov, Appl. Phys. Lett. **68**, 415 (1996).
20. P. F. Fewster and N. L. Andrew, J. Appl. Cryst. **28**, 451 (1995).
21. J. C. Braveman and R. Sinclair, J. Electron Microsc. Technique **1**, 53, (1984).
22. G. M. Ma and S. Chevaharoencul, MCNC Technical report TR90-33 (1990).
23. W. Shan, B. D. Little, A. J. Fischer, J. J. Song, B. Goldenberg, W. G. Perry, M. D. Bremser and R. F. Davis, to be submitted.
24. C. M. Balkas, C. Basceri, and R. F. Davis, Powder Diffraction **10**, 266 (1995).
25. E. Burnstein, Phys. Rev. **93**, 632 (1954).
26. A. Gassmann, T. Suski, N. Newman, C. Kisielowski, E. Jones, E. R. Weber, A. Liliental-Weber, M. D. Rubin, H. I. Heleva, I. Grzegory, M. Bockowski, J. Jun, S. Porowski, J. Appl. Phys. **80**, 2195 (1996).
27. B. Monemar, Phys. Rev. B **10**, 676 (1974).
28. K. Pakula, A. Wyszomolek, K. P. Korona, J. M. Baranowski, R. Stepniewski, I. Grzegory, M. Bockowski, J. Jun, S. Krukowski, M. Wroblewski, and S. Porowski, Solid State Commun. **97**, 919 (1996).
29. K. N. Tu, J. W. Mayer, and L. C. Feldman, in *Electronic Thin Film Science*, (Macmillan, New York 1992) p. 84.
30. V. A. Savastenko and A. U. Sheleg, Phys. Status Solidi A **48** 135 (1978)
31. T. Azuhata, T. Sota, K. Suzuki, J. Phys.: Condens. Matter **8**, 3111 (1996)
32. C. Kisielowski, J. Krüger, S. Rumimov, T. Suski, J. W. Ager III, E. Jones, Z. Liliental-Weber, M. Rubin, E. R. Weber, M. D. Bremser and R. F. Davis, to be submitted to Phys. Rev. B, 1996.
33. *Landolt-Börnstein*, edited by O. Madelung (Springer, New York, 1982), Vol. 17.
34. K. Kim, W. R. L. Lambrecht, and B. Segall, Phys. Rev. B **50**, 150 (1994).
35. A. Polian, M Grimsdich, and I. Grzegory, J. Appl. Phys. **79**, 3343 (1996).
36. W. Shan, T. J. Schmidt, R. J. Hauenstien, J. J. Song and B. Goldenberg, Appl. Phys. Lett. **66**, 3492 (1995).
37. P. Perlin, I. Gorczyca, N. E. Christensen, I. Grzegory, H. Teisseyre, and T. Suski, Phys. Rev. B **45**, 13 307 (1992).
38. W. Rieger, T. Metzger, H. Angerer, R. Dimitrov, O. Ambacher, M. Stutzmann, Appl. Phys. Lett. **68**, 970 (1995).
39. Pirouz P, et. al. Nitride Workshop on Wide Bandgap Nitrides, St. Louis, (1996)
40. A. Westwood, R. Youngman, M. McCartney, A. Cormack and M. Notic, J. Mater. Res. **10**, 1270 (1995).

41. F. Chien, X. Jing, P. Pirouz, M. D. Bremser, and R. F. Davis, Appl. Phys. Lett. **68**, 2678 (1996).
42. C. Roland, MRS Bulletin **21**, 27 (1996).
43. A. Cullis, MRS Bulletin **21**, 21 (1996).

VIII. Ohmic Contact Formation on p-type GaN

A. Introduction

The formation of ohmic contacts with semiconductor materials and devices is a fundamental component of solid state device architecture. As device size has diminished and the scale of integration has increased, the quality of these interfaces has become an increasingly important concern. In addition, the presence of parasitic resistances and capacitances, such as those existing at contact interfaces, becomes more detrimental at higher operating powers and higher oscillation frequencies. For many devices, the losses that occur at the contact interfaces account for a large fraction of the total losses, and as such are responsible for significant impact on device performance.

The development of adequate and reliable ohmic contacts to the compound semiconductors, particularly those with wider band gaps, has met a number of challenges. The subject of ohmic contacts to p- and n-type III-V compounds, mostly GaAs, AlGaAs, and InP, has received a great deal of attention over the past decade, and significant advances have been made [1-12]. By comparison, the III-V nitrides have received little attention in this regard. However, interest in these materials has been renewed in recent years as thin film growth techniques have improved, p-type doping in GaN and AlGaN solid solutions has been achieved, and p-n junctions have been fabricated.

The majority of successful ohmic contact systems that have so far been implemented with the more conventional compound semiconductors have relied upon alloying (liquid-phase reaction) or sintering (solid-phase reaction) via post-deposition annealing treatments, and/or the presence of high carrier concentrations near the interface [1,2,6,12]. However, many otherwise successful ohmic contact systems have only limited thermal stability and are subject to degradation, usually in the form of extensive interdiffusion, interfacial reaction, and interphase growth, accompanied by increase in contact resistivity, under subsequent thermal processing steps. It is reasonable to suppose that the cleanliness and preparation of the semiconductor surface prior to contact deposition plays a significant role in the behavior of the interface, and there are indications in the literature that support this [2,11-13]. Thorough oxide removal is especially important, though it may well prove to be a persistent challenge with Al-containing compounds in particular.

In this study, two main approaches are being taken in the development of ohmic contacts to GaN and AlN. The first approach is similar to that which has resulted in the majority of successful ohmic contacts to the more conventional compound semiconductors such as GaAs: the creation of high carrier concentrations in the semiconductor at the metal interface by means of alloying, sintering, or implantation of dopant species. The so-called pinning of the Fermi level at this surface, particularly with GaAs, results in a more or less fixed potential barrier at

the metal interface. In the case of the pinned Fermi level of GaAs, the approach has generally been to shrink the width of the depletion layer by means of increasing the carrier concentration to the point where carrier tunneling through the barrier occurs readily. Even with optimization of contact composition and annealing times and temperatures, the lowest contact resistivities (ρ_c) have been obtained only on the most heavily doped materials. Though there are indications that high doping levels and extensive interfacial reactions through alloying and sintering are not essential for ohmic contact formation in all cases, these processes have proven useful for minimizing ρ_c [2,11-13].

The other approach toward ohmic contact formation to be taken in this study involves the Schottky-Mott-Bardeen (SMB) model of semiconductor interfaces [14,15]. In this model the relative values of work function of the materials involved determine the band structure of the interface and thus the nature of any potential barriers present. The presence of interfacial states at the semiconductor surface can interfere with the alignment of the Fermi level across the interface and overshadow the effect of the inherent difference in work function between the two materials. The III-V nitride compounds are more ionically bonded than their phosphide and arsenide counterparts, as a result of larger electronegativity differences between the component elements. According to the observations of Kurtin *et al.* [16], and further refined by Schlüter [17], this fact indicates that the nitrides should experience less Fermi level stabilization or "pinning" at the surface than do the more covalent compounds. Thus, the barrier heights of contacts to the nitrides should be more dependent on the contact material than is the case with the more conventional and more covalent semiconductors such as Si, GaAs, InP, SiC, etc. With the work of Foresi and Moustakas [18,19], and more recently M. E. Lin *et al.* [20], this concept is now receiving attention. The SMB model also indicates that the cleanliness of the interface plays an important role in its electrical behavior, particularly in the minimization or elimination of any insulating layers at the interface.

B. Experimental Procedure

The substrates used for III-nitride film growth were 6H-SiC wafers supplied by Cree Research, Inc. The GaN films used in this contacts study were grown by means of metalorganic vapor phase epitaxy (MOVPE). The growth reactor used for the nitride film deposition is described in other sections of this report. Magnesium was incorporated into the films during growth as the acceptor impurity.

Prior to metal deposition, the GaN/SiC films were cleaned with a 1:1 HCl:DI H₂O dip and carefully pulled dry from the solution. Any remaining cleaning solution was blown dry with N₂. A thermal desorption step at 750°C for 15 min under UHV conditions (base pressure 10⁻⁹ Torr) was performed to achieve a cleaner surface. Pt layers were deposited on Mg-doped

GaN (MOVPE-grown, $N_a-N_d=1.0\times10^{19}\text{ cm}^{-3}$) using electron beam evaporation, to a thickness of 1000 Å. Film thickness was monitored using a quartz crystal oscillator.

After deposition, I-V measurements were taken between separate pads of the TLM patterns, using tungsten probe tips and an HP 4145C Semiconductor Parameter Analyzer. Annealing treatments were performed in a flowing N_2 atmosphere at a series of temperatures, 400, 500, 600 and 700°C for 30 s each step, using a Heatpulse 410 rapid thermal annealing (RTA) furnace. TLM measurements were taken by measuring the total resistance between identical contact pads as a function of separation distance l . The TLM test pattern was defined using photolithography and consisted of contact pads measuring $30\times300\text{ }\mu\text{m}$, separated by distances of 5, 10, 20, 30, and 50 μm . The contact resistivity was obtained from the plot of $R(l)$ vs. l , as described by Reeves and Harrison [21]. The mathematical assumptions and pattern geometry inherent in this model yield values for ρ_c that represent an upper limit; thus, the measured values are conservative assessments of performance. In addition, for every test pattern geometry there is a lower limit of ρ_c below which it is not possible to obtain precise ρ_c calculations. This is due to the fact that the linear $R(l)$ plot becomes very steep and very close to the origin with decreasing ρ_c . For the test geometry used in this study to date, and for many of the TLM results reported by other researchers in the field, the practical lower limit for precise ρ_c calculation is about $10^{-6}\text{ }\Omega\cdot\text{cm}^2$.

C. Results

Pt contacts on Mg-doped GaN were ohmic in the as-deposited condition, as shown in Fig. 1 below. Upon annealing at temperatures up through 700°C, the I-V behavior of the Pt contacts became more resistive. The specific contact resistivity ρ_c as a function of annealing is plotted in Fig. 2. Annealing of the samples was not continued beyond the 700°C step because by that point the specific contact resistivity had increased by four orders of magnitude and reached a regime of ineffective performance.

Depth profiling through the Pt contact layers and into the GaN layers revealed that significant intermixing of Pt, Ga, N, and Mg occurred as a result of annealing. Elemental profiles obtained from SIMS analysis of the as-deposited Pt/p-GaN sample are shown in Fig. 3, while similar data from the annealed samples, heated sequentially through 700°C, are plotted in Fig. 4. The data from the as-deposited sample revealed a fairly abrupt Pt-GaN interface. One interesting feature is that the signal from mass number 24, corresponding to Mg, shows some increase in the bulk of the Pt layer even in the as-deposited sample. In the annealed sample, indications of a clear interface between the Pt and GaN layers had completely disappeared. No abrupt changes in elemental distributions are shown, indicating a high degree of intermixing, and the only suggestion of the Pt-GaN interface which had been present before annealing is the gradual disappearance of the Pt signal (mass number 195).

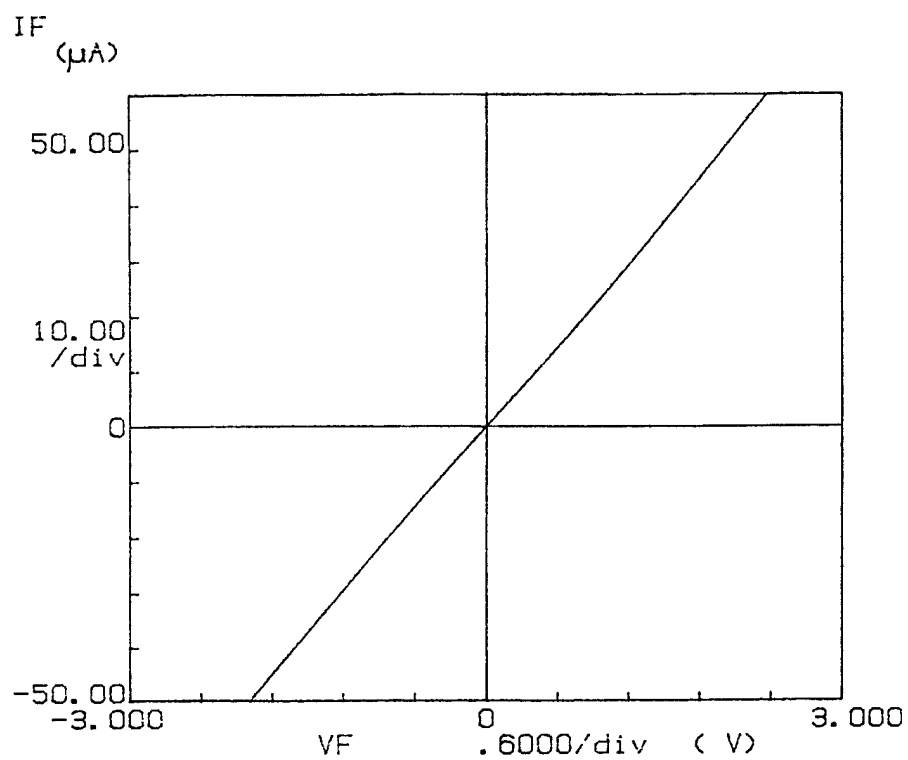


Figure 1. I-V behavior of as-deposited Pt contacts on Mg-doped GaN.

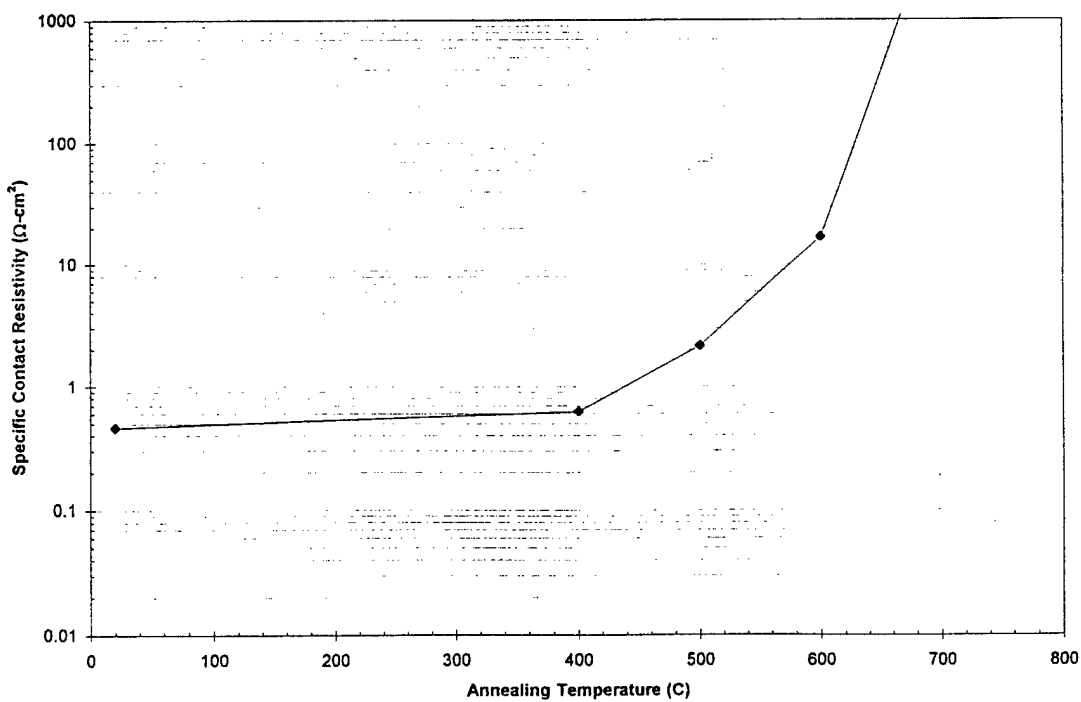


Figure 2. Specific contact resistivity ρ_c of Pt contacts on Mg-doped GaN as a function of annealing temperature.

D. Discussion

Platinum is a very high work function metal ($\phi_{Pt}=5.65$ eV) and, thus, provides a favorable band offset for ohmic contact formation to a p-type semiconductor. In addition, Pt is thermally very stable and highly resistant to oxidation. Investigation of Pt as an ohmic contact candidate for p-type GaN was conducted earlier in this project, but the results varied substantially with GaN film quality and electrical properties. The recent GaN:Mg films used in this study represent the highest quality p-GaN material grown at NCSU to date, and this material quality is reflected in better contact performance than had been measured earlier.

The work of Sands *et al.* [22,23] has shown that extensive interfacial reaction can occur between Pt and GaAs, due to metallurgical reactions involving both Ga and As. Though lacking the mobile and reactive As species, GaN nevertheless has shown the ability to react with noble metals when annealed at high temperature, as has been documented by the authors

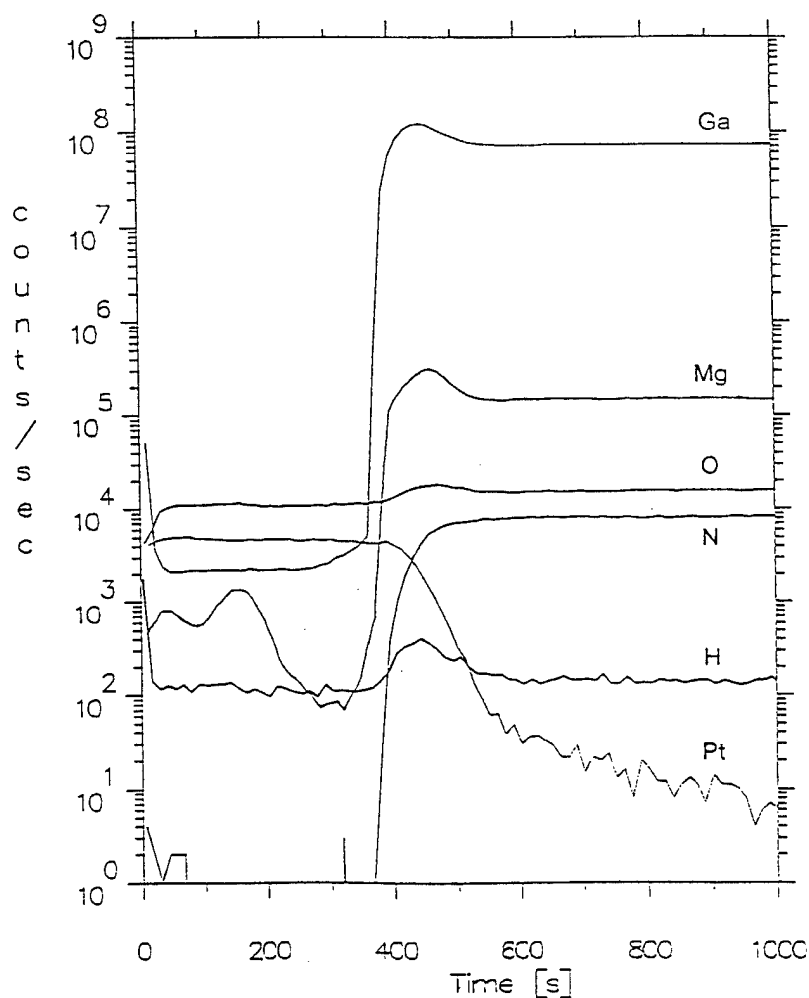


Figure 3. SIMS depth profile of as-deposited Pt/p-GaN:Mg contact layers, showing abrupt Pt-GaN interface and indications of Mg in the bulk of the Pt layer.

in earlier studies [24]. Thus, changing behavior of the Pt contacts as a function of annealing temperature is not surprising. The increasing resistance is likely due to a combination of effects, including (1) the neutralization and/or outdiffusion of the Mg acceptor impurities in the interfacial region, which lowered the effective carrier concentration at the contact interface; (2) the outdiffusion of N from the GaN, which created shallow-donor N vacancies that compensated the p-type conduction; or (3) an unfavorable reaction between Pt and Ga that increased the bulk and/or interfacial resistivity.

E. Conclusions

Evaporated Pt contacts on Mg-doped GaN exhibit ohmic, moderate-resistivity behavior in the as-deposited condition. Annealing treatments through 700°C resulted in substantial increases in specific contact resistivity. Elemental depth profiling analysis via SIMS revealed

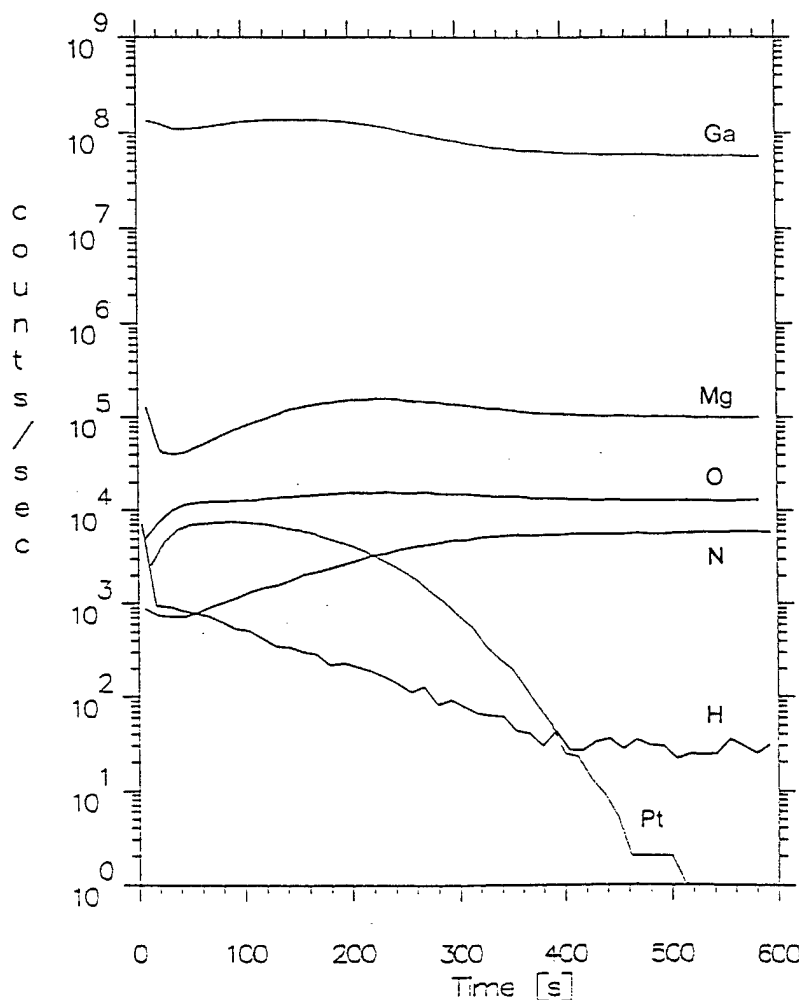


Figure 4. SIMS depth profile of Pt/p-GaN:Mg contact layers annealed through 700°C, showing intermixing of elements and absence of a well-defined Pt-GaN interface.

that significant intermixing of the components of the contact system occurred as a result of annealing. The achievement of low-resistivity ohmic contacts to p-GaN is a necessary component for the development and application of many types of GaN-based devices. Further characterization of contact candidates for p-type material, including microstructural information obtained from X-TEM analysis, will yield greater understanding of the chemical and structural contributions to contact behavior and will allow more rapid and knowledgeable development of improved contact schemes and their capabilities.

F. Future Plans and Goals

For p-GaN, the challenges to contact improvement, described above, are formidable. By comparison, the advances that have been made with n-GaN contacts have been rather easily achieved. However, further improvement of p-GaN contacts must be made to reduce the high series resistance inherent in the devices now being fabricated. Despite the stronger need for progress in this area, very little detailed electrical characterization of p-GaN ohmic contacts has been reported to date. The only values for specific contact resistivity ρ_c that have been made available have come from the present work and announcements from Cree Research, Inc., which have reported ρ_c values on the order of $10^{-2} \Omega \cdot \text{cm}^2$ for $p=10^{18} - 10^{19} \text{ cm}^{-3}$ [25]. For proprietary reasons, the ohmic contact schemes used by Cree have not been described.

In order to take greater advantage of the valuable properties of GaN and to achieve the full range of superior device performance envisioned by the solid state community, it is necessary to reduce the ρ_c of p-GaN contacts at least three or four orders of magnitude below the levels already obtained. To accomplish this, it is almost certainly necessary to take full advantage of the two main avenues of contact improvement described above: to increase acceptor concentrations and to reduce the semiconductor band gap at the contact interface. With this in mind, the following approaches are recommended for further investigation, to identify the most efficient means of achieving superior contacts:

- Increase the doping level of acceptor impurities near the top surface of p-GaN films during growth. To improve the incorporation of acceptor impurities, it may be necessary to adjust the Ga-N ratio during growth to facilitate the addition of dopant atoms to the Ga sites. Activation of the dopant species must be optimized.
- Add acceptor impurities to the near-surface region of p-GaN films by means of ion implantation, prior to metallization. Again, activation of the dopant species must be optimized. Performing the implants at high temperature and/or post-implant annealing will be necessary to achieve this.
- Make use of metallurgical reactions of contact metal components with GaN, in order to draw Ga out of the GaN structure and leave behind Ga vacancies that can be filled with acceptor impurities. Nickel is suggested as a favorable candidate for this purpose.

Contact studies by Trexler *et al.* [26], thermodynamic studies by Mohny *et al.* [27,28] and the surface analytical work of Bermudez *et al.* [29] have demonstrated that Ni reacts extensively with GaN, with some reaction occurring even at room temperature. At higher temperatures (~600°C and above), Ga dissolves into Ni layers while the released N desorbs.

- Make use of InN or a gradation of InGaN as an interlayer to reduce the semiconductor band gap at the contact interface. To accomplish this for p-GaN contacts, it will be necessary to either (1) improve InN growth and achieve high-quality p-InGaN and p-InN films, or (2) incorporate In into contact metals such that In is able to substitute into the p-GaN lattice upon annealing of the contacts.

G. References

1. T. C. Shen, G. B. Gao, H. Morkoç, J. Vac. Sci. Technol. B **10** (5) 2113 (1992).
2. R. Williams, *Modern GaAs Processing Techniques* (Artech House, Norwood, MA, 1990).
3. M. Murakami, Materials Science Reports (5) 273 (1990).
4. A. Piotrowska and E. Kaminska, Thin Solid Films **193/194** 511 (1990).
5. A. Piotrowska, A. Guivarc'h and G. Pelous, Solid-St. Electron. **26** (3) 179 (1983).
6. V. L. Rideout, Solid-St. Electron. **18** 541 (1975).
7. K. Tanahashi, H. J. Takata, A. Otsuki and M. Murakami, J. Appl. Phys. **72** (9) 4183 (1992).
8. H. J. Takata, K. Tanahashi, A. Otsuki, H. Inui and M. Murakami, J. Appl. Phys. **72** (9) 4191 (1992).
9. M. C. Hugon, B. Agius, F. Varniere, M. Froment and F. Pillier, J. Appl. Phys. **72** (8) 3570 (1992).
10. W. O. Barnard, G. Myburg and F. D. Aurret, Appl. Phys. Lett. **61** (16) 1933 (1992).
11. G. Stareev, Appl. Phys. Lett. **62** (22) 2801 (1993).
12. E. D. Marshall and M. Murakami, in *Contacts to Semiconductors*, edited by L.J. Brillson (Noyes, Park Ridge NJ, 1993).
13. F. W. Ragay, M. R. Leys and J. H. Wolter, Appl. Phys. Lett. **63** (9) 1234 (1993).
14. H. K. Henisch, *Semiconductor Contacts*. (Clarendon Press, Oxford, 1984).
15. E. H. Rhoderick, *Metal-Semiconductor Contacts* (Oxford University Press, New York, 1988).
16. S. Kurtin, T. C. McGill and C. A. Mead, Phys. Rev. Lett. **22** (26) 1433 (1969).
17. M. Schlüter, Phys. Rev. B **17** (12) 5044 (1978).
18. J. S. Foresi, *Ohmic Contacts and Schottky Barriers on GaN*, M.S. Thesis, Boston University (1992).
19. J. S. Foresi and T. D. Moustakas, Appl. Phys. Lett. **62** (22) 2859 (1993).
20. M. E. Lin, Z. Ma, F. Y. Huang, Z. F. Fan, L. H. Allen, and H. Morkoç, Appl. Phys. Lett. **4** (8) 1003 (1994).
21. G. K. Reeves and H. B. Harrison, IEEE Electron Device Lett. **EDL-3** 111 (1982).
22. T. Sands, V. G. Keramidas, A. J. Yu, K-M. Yu, R. Gronsky, and J. Washburn, J. Mater. Res. **2** (2) 262 (1987).
23. T. Sands, V. G. Keramidas, K-M. Yu, J. Washburn, and K. Krishnan, J. Appl. Phys. **62** (5) 2070 (1987).
24. L. L. Smith, M. D. Bremser, E. P. Carlson, T. W. Weeks, Jr., Y. Huang, M. J. Kim, R. W. Carpenter, and R. F. Davis, in *Gallium Nitride and Related Materials*, edited by R. D. Dupuis, J. A. Edmond, S. Nakamura, and F. A. Ponce (Mat. Res. Soc. Proc. 395, Pittsburgh, PA, 1996).

25. J. Edmond, 3rd Nitride Workshop, St. Louis, MO, March 13-15, 1996.
26. J. T. Trexler, S. J. Miller, P. H. Holloway, and M. A. Khan, in *Gallium Nitride and Related Materials*, edited by R. D. Dupuis, J. A. Edmond, S. Nakamura, and F. A. Ponce (Mat. Res. Soc. Proc. 395, Pittsburgh, PA, 1996).
27. S. E. Mohny, B. P. Luther, X. Lin, and T. N. Jackson, in *Gallium Nitride and Related Materials*, edited by R. D. Dupuis, J. A. Edmond, S. Nakamura, and F. A. Ponce (Mat. Res. Soc. Proc. 395, Pittsburgh, PA, 1996).
28. S. E. Mohny and X. Lin, *J. Electronic Materials* **25** (5) 811 (1996).
29. V. M. Bermudez, R. Kaplan, M. A. Khan, and J. N. Kuznia, *Phys. Rev. B* **48**, 2436 (1993).

IX. Schottky Barriers on GaN

A. Introduction

In the past few years, there has been a resurgence in the interest of using the high band gap nitride semiconductors for device applications. One of the high band gap semiconductors receiving such attention is GaN. This renewed interest in GaN stems from its band gap value of 3.45 eV and its desirable physical properties, which have been improved with new growing techniques. Gallium nitride has excellent chemical and thermal stability that makes it appealing for use in high-temperature electronics, optoelectronics, and high-power devices [1]. Device applications mentioned for GaN are blue light emitting diodes, lasers, detectors, and high-frequency, high-power and temperature transistors [2]. Accordingly, for such devices to be fabricated, the properties of metal-GaN contacts must be determined. Investigation into which metals make ohmic contacts and which make rectifying or Schottky barrier contacts must be performed for commercial applications.

Experiments are currently underway at North Carolina State University to determine the barrier height of Pt on n-type GaN. The Schottky-Mott theory should apply to the determination of the barrier heights because of the ionic nature of GaN [2]. The Schottky-Mott theory states that the barrier height is the difference between the metal work function and the electron affinity of the semiconductor [3].

$$\phi_b = \phi_m - \chi_s$$

Where ϕ_b is the Schottky barrier height, ϕ_m is the metal work function and χ_s is the electron affinity of the GaN. Thus, the higher the metal work function, the higher the barrier height. The work function of Pt is 5.65 eV and the electron affinity of GaN is 3.3 eV. Therefore, Pt is a good choice for a Schottky contact metal based on this theory.

B. Experimental Procedure

The GaN used for this experiment was grown on a 6H-SiC substrate. The orientation of the SiC was on-axis without an epilayer. Cree Research, Inc. supplied the SiC wafer. The Si doped n-type GaN was grown in a OMVPE reactor at the NCSU Nitride laboratory under the direction of Dr. R. F. Davis. Capacitance-voltage techniques were used to measure the doping of the GaN film. The result of C/V testing indicated that the doping level ($N_d - N_a$) is $8 \times 10^{16} \text{ cm}^{-3}$. The thickness of the film is 2 μm and the size of the sample is 1.5 cm by 1.5 cm.

The sample was degreased by submerging it in acetone for one min. followed by a dip in methanol for one min. To remove the oxides on the surface of the sample, it was placed in a HCl bath for 15 min. Following the HCl dip, the sample was mounted onto a sample holder and placed into vacuum. Once under vacuum, the sample was thermally desorbed at 750°C for 15 min.

After the sample temperature returned to room temperature, a 1000Å blanket layer of platinum was deposited on the GaN. A layer of photoresist was placed on top of the Pt. The exposed Pt was then etched back using a mixture of HCl, HNO₃ and DI:H₂O in the ratios 8:1:7. The remaining Pt formed the Schottky contacts. After the etching of the Pt, another layer of photoresist was patterned on the sample. This time, Al was deposited on the sample and photoresist. Using liftoff, the Al and the ohmic contacts were fabricated. The pattern of the fabricated contacts can be seen in Fig 1.

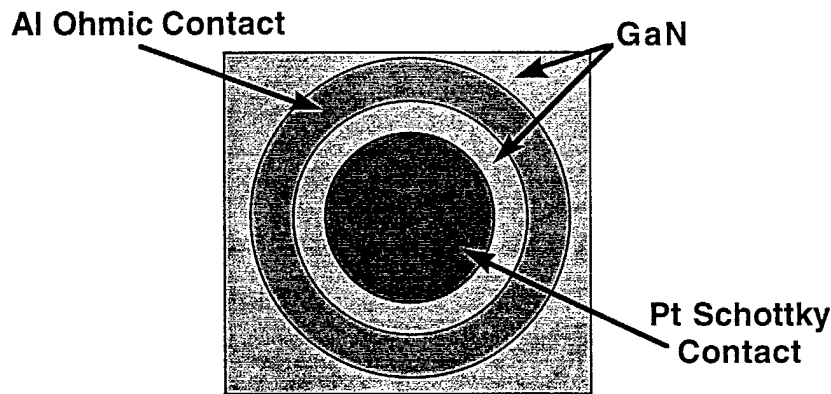


Figure 1. Schottky contact pattern.

The contacts consist of the Schottky contact, a Pt disk, surrounded by a ring of Al. The Al ring is the ohmic contact. Diameters of the Schottky contacts are 50, 100, 150 and 200 μm. The separation between the ohmic and Schottky contacts ranged from 10 to 30 μm. Overall, the pattern of contacts consisted of an array of contacts of different separation distances for contacts of different diameters. For example, the 50 μm Schottky contact array consisted of multiple contacts of different separation distances.

After the fabrication of the contacts, testing of the sample consisted of collecting electrical data using current-voltage (I/V) techniques. The data collection was achieved using a computer-controlled Keithley Source Measure Unit. This unit was then connected to tungsten probe tips which made contact to the fabricated devices.

C. Results and Discussion

The collected I/V data can be analyzed to find the values of the ideality factor n and the Schottky barrier height ϕ_b . Current-voltage characteristics of a forward biased Schottky diode follow the equation [3],

$$I = I_s \exp\left(\frac{qV}{nkT}\right) \cdot \left[1 - \exp\left(-\frac{qV}{kT}\right)\right].$$

However, if the voltage is greater than $3kT/q$ (.075 eV) then the equation can be simplified to the following [3]:

$$I = I_s \exp\left(\frac{qV}{nkT}\right).$$

Where I_s is the saturation current, n is the ideality factor, and the rest of the terms have their usual meanings. The data can be plotted with axes of $\ln(I)$ vs. V for the forward biased values. The resulting plot should have a linear region where the diode behaves ideally [3].

This linear region should span many decades in the semilog plot. By curve fitting this linear region, we can calculate the ideality factor by comparing the curve-fitted data to the simplified equation above. The barrier height can then be determined by using the following equation and solving for the barrier height ϕ_b ,

$$I_s = A^* T^2 \exp\left(\frac{-\phi_b}{kT}\right).$$

Where A^* is the Richardson constant for GaN, T is the temperature and k is Boltzmann's constant. A reported value for A^* is $26.4 \text{ A cm}^{-2} \text{ K}^{-2}$ [4].

The $50 \mu\text{m}$ diameter contacts were tested first. The data for one of these contacts can be seen in Figs. 2 and 3.

As can be seen in Fig. 2, the reverse bias characteristics of the device are quite good. In fact, the leakage current at -10V reverse bias for this device is less than 1 nA . This is the lowest reported leakage current for Pt Schottky contacts of this size to date. Most researchers are

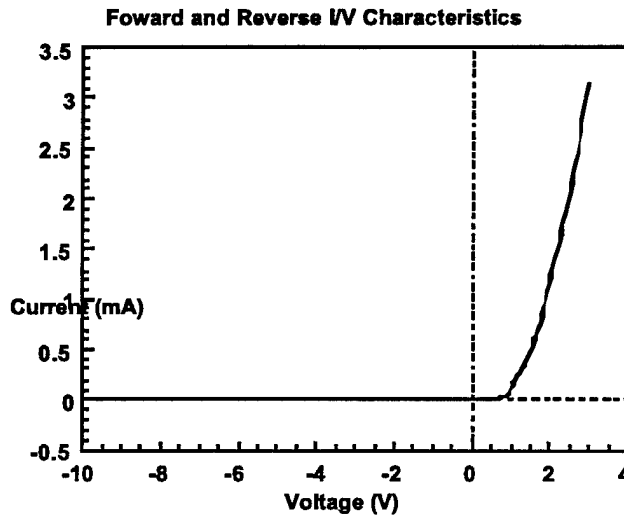


Figure 2. Forward and reverse I/V characteristics for a $50 \mu\text{m}$ contact.

reporting leakage currents in the μA range for Pt contacts on GaN grown on sapphire. Figure 3 is a semilog plot of the forward voltage region of fig 2. In Fig. 3, the linear region of the plot spans more than 5 decades, which is usually an indication of a good Schottky contact. By performing the analysis outlined above, we calculated the Schottky Barrier Height (SBH) for this device to be 1.36 eV with a corresponding ideality factor of 1.13. These values are consistent with the values calculated for the other contacts of the same size tested. The ranges for the calculated SBH and ideality factor for the $50\text{ }\mu\text{m}$ contacts can be seen in Table I.

The $100\text{ }\mu\text{m}$ contacts were tested next. The forward and reverse current voltage plots can be seen in Figs. 4 and 5. Again, the current characteristics for the $100\text{ }\mu\text{m}$ contacts are quite good. The leakage current is extremely low, $< -1\text{ nA}$, at a reverse bias of -10V . The forward characteristics also yield good results. For this device tested, the barrier height turned out to be 1.28 eV with an ideality factor of 1.13. The range for the electrical properties of the $100\text{ }\mu\text{m}$ contacts tested can also be seen in Table I.

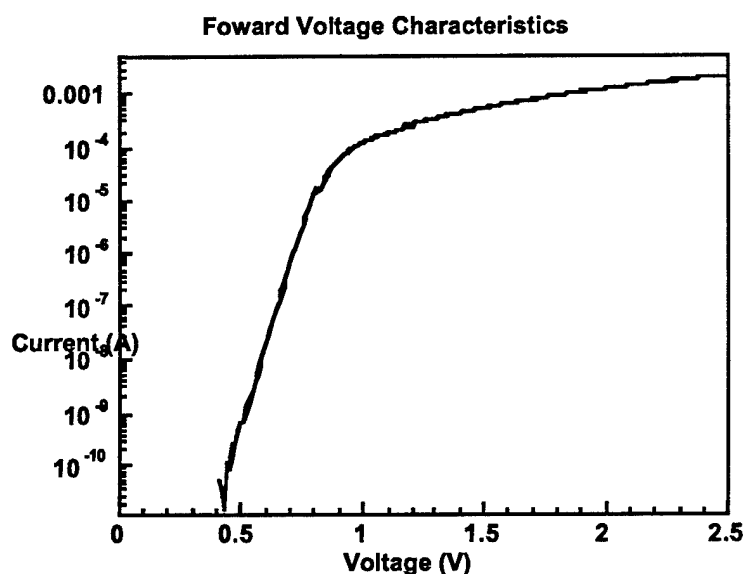


Figure 3. Forward bias voltage characteristics for a $50\text{ }\mu\text{m}$ contact.

Table I. Electrical Characteristics of Pt Schottky Contacts on n-type GaN

	$50\text{ }\mu\text{m}$ dia contacts	$100\text{ }\mu\text{m}$ dia contacts
Schottky Barrier Height (eV)	1.01 to 1.36	0.98 to 1.28
Ideality Factor	1.13 to 1.71	1.13 to 2.11
Avg. Leakage Current at -10V (A)	$< 1 \times 10^{-10}$	$< 1 \times 10^{-10}$
Compliance (-1A) at (V)	not tested yet	77.4

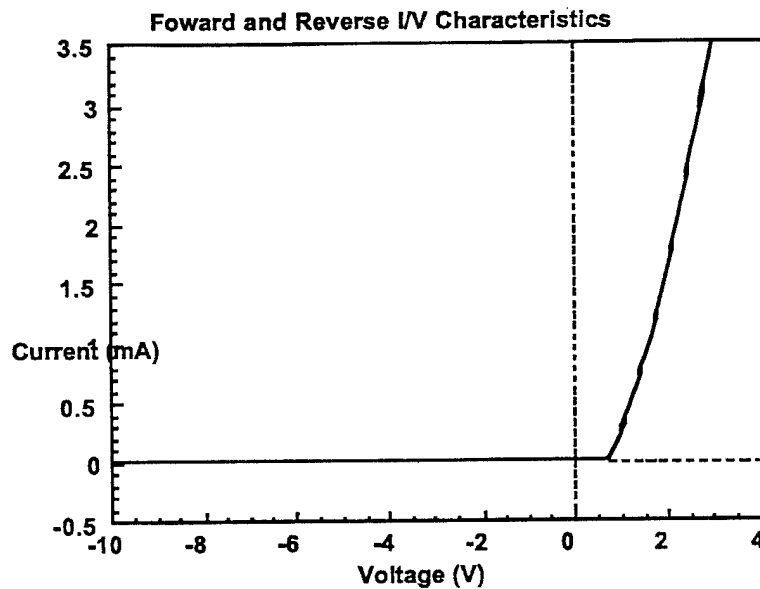


Figure 4. Forward and reverse I/V characteristics for a 100 μm contact.

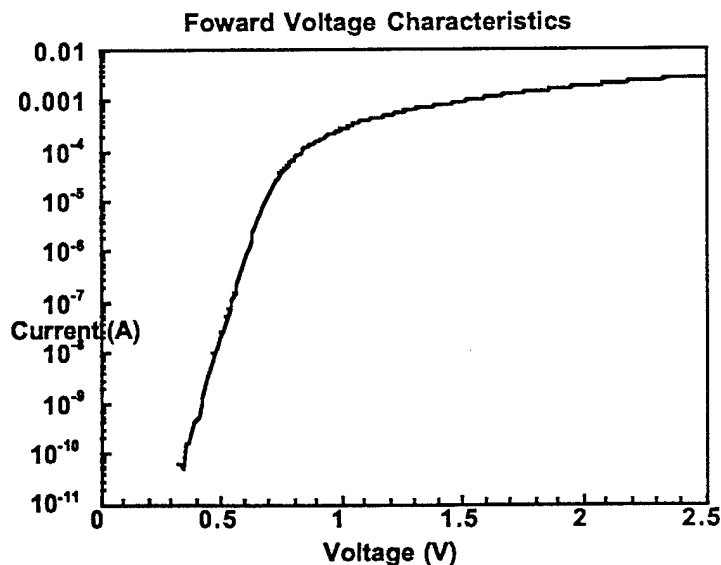


Figure 5. Forward bias voltage characteristics for a 100 μm contact.

From Fig. 5, we can see that the linear region of the plot spans more than 5 decades, again indicating a good device. Finally, the breakdown of this device was investigated. Figure 6 is a plot of the breakdown of this diode.

From Fig. 6, the leakage current from 0 to -10V was less than -1 nA. As the reverse bias voltage increased to -20V, the leakage current also increased to -17 nA at -20V. As the bias voltage progressed to -40V, the current also increased to -2.7 μA . The diode finally reached the compliance value of the SMU (-0.1A) at a reverse bias of -77.5 volts.

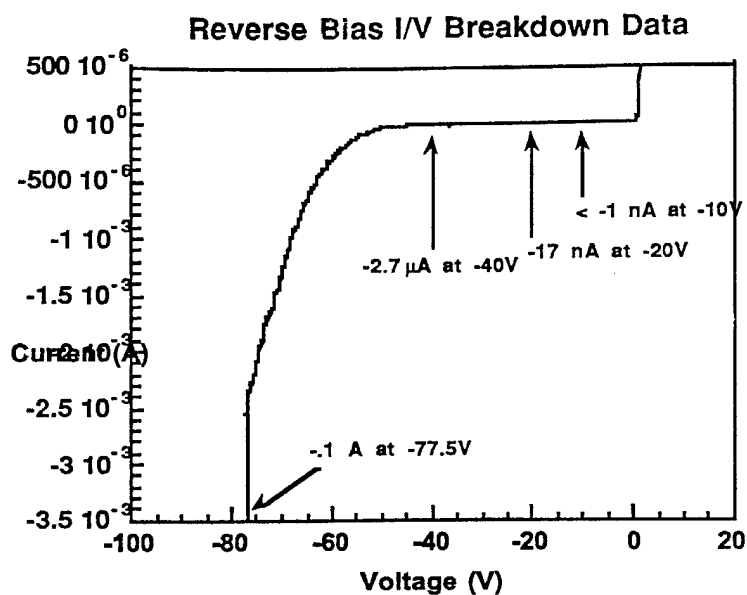


Figure 6. Breakdown of a 100 μm contact.

D. Conclusions and Future Work

We have fabricated new Pt Schottky contacts on n-type GaN with a doping of $8\text{E}16\text{ cm}^{-3}$. The results are very encouraging. We are achieving high barrier heights and low ideality factors for both 50 and 100 μm diameter contacts. The offsetting of our ideality factors from 1 is believed to be caused by recombination at defects in the GaN. The diodes tested have been consistent in terms of low leakage currents.

In the future, we plan to test the 150 and 200 μm contacts before temperature effect studies are started on the electrical properties of these devices. Also, C/V measurements will be taken to compare to the I/V results.

X. Dry Etching of Gallium Nitride

A. Introduction

Gallium nitride is a wide bandgap semiconductor which has applications such as short wavelength light emitters and detectors, high temperature, frequency, and power electronics [1,2]. A crucial step in creating these devices is to etch anisotropic features in the GaN. Wet etching has been employed in many semiconductor processes. Thus far, wet etching has produced poor results on GaN, such as slow etch rate and isotropic etch profiles [3]. Both of these characteristics are undesirable for commercial applications. As technology advances, the need for anisotropic etch profiles increases to accommodate a smaller, more densely packed network of devices. Dry etching is an attractive alternative to wet etching. Varying degrees of anisotropy along with high etch rates can be achieved using different dry etch techniques.

There are four primary dry etch techniques that have been employed on GaN. They are Reactive Ion Etching (RIE), Electron Cyclotron Resonance Etching (ECR), Magnetron Enhanced Reactive Ion Etching (MIE), and Inductively Coupled Plasma Etching (ICP). Out of the four techniques, RIE produces the slowest etch rates and lowest degree of anisotropy [4-6]. ECR, which has had much attention from Pearton *et al.* [1,3,7-8], produces significantly better results than RIE. MIE, was employed by McLane *et al.* [2], and produced results comparable to that of ECR etching. Inductively coupled plasma etching is the newest addition to the dry etching techniques of GaN. Shul [9] has shown that ICP can produce etch characteristics similar to that of ECR.

The objectives of this report are to discuss recent advances in etching GaN with the three techniques of dry etching. In the following sections, each of the etching techniques will be discussed and compared, along with a discussion of the work being done etching GaN in our labs and the results to date.

B. Etching Overview

As previously stated, each of the three primary dry etch techniques will be discussed. They will be presented individually, and then compared at the end of this section.

Reactive Ion Etching. As the III-V nitride technology advances, the need for commercially viable processes is getting more important. In this case, a commercially viable etching process would be one that produces the fastest controllable etch rate along with etch profiles that are suitable for the desired electronic device. Reactive ion etching is lacking in both of these areas. The reason for these shortcomings are the parameters that are involved in the process. Reactive ion etching is generally performed at pressures between 10 and 100 mTorr [4-6]; at these pressures, the mean free path of the bombarding ions is between 5 and .5 mm, respectively. With mean free paths this small, the bombarding ions will hit other ions and scatter. This

scattering will result in the ions not hitting the GaN surface at 90° angles, resulting in a lesser degree of anisotropy than is usually desired. There are some cases where isotropic etch profiles are desired, but for the most part, anisotropic etch profiles are desired.

Etch rate is another area where RIE has fallen behind the other two methods. Lin *et al.* [4] have reported the highest etch rate to date via RIE of 105 nm/min in a BCl₃ plasma. This is actually a fairly high etch rate, but at what cost? The parameters were 15 sccm BCl₃, 10 mTorr pressure, 150 w RF power, and -600 v dc bias. The etch rate is in part a function of the dc self bias and the energy of the bombarding ions is also a function of the dc self bias. As the ion energy increases, there is a better the chance of etch induced damage to the surface of the material. There have been no etch induced surface damage studies on GaN reported to date. Murtagh *et al.* [10] showed via photoreflectance spectroscopy that the larger the dc self bias, the greater the surface damage to GaAs. Even though GaN is a much stronger material than GaAs, it could still undergo the same damage as GaAs, just to a lesser extent.

Electron Cyclotron Resonance Etching. Out of the major types of etching GaN, ECR has the most widespread use in the research field. Shul *et al.* [9] have recently obtained etch rates of 900 nm/min in a Cl₂/H₂/ Ar plasma using ECR etching. One of the reasons for the high etch rates is that ECR produces a high density plasma, which results in higher etch rates as compared to RIE. The plasma in an RIE is everywhere in the chamber between the source and ground. In an ECR etching system, the plasma is magnetically confined by permanent magnets on the outside of the chamber.

The potential for surface damage to the material is reduced in an ECR etcher. ECR etching uses a microwave source instead of a RF source to produce the plasma, and a separate RF source on the substrate to bias the substrate. Since the microwave source produces a high density plasma, a lower bias is required to etch the material. With a lower dc bias on the substrate, the energies of the ions bombarding the surface of the material is in turn lowered. This reduces the risk of producing etch induced surface damage.

Magnetically Enhanced Reactive Ion Etching. The major difference between RIE and MIE is that the plasma is magnetically confined in an MIE etcher. The magnetic field confines the plasma around the cathode that the sample is on. This in turn increases the etch rate and lowers the dc bias. Along with other things, the dc bias is a function of the surface area of the ground. Since the plasma is confined, the surface area of the ground that the plasma is exposed to is significantly reduced. McLane *et al.* [2] have reported etch rates of 350 nm/min using a BCl₃ plasma which is the highest reported to date.

Inductively Coupled Plasma Etching. A newcomer to etching GaN, ICP has already proven to have much potential as the best etching technique for GaN. Etch rates over 7000 Å/min have been achieved by Shul [9] using Cl₂/H₂/Ar chemistries in a commercial ICP system. Like ECR, ICP produces a high density plasma and has a separate RF source on the substrate to

control the dc bias. ICP has some distinct advantages over ECR etching, such as better control of plasma density, higher operating pressures, more economical, and more easily scaled up to production.

The above has been a brief description of the four primary dry etch techniques for GaN. The ICP, ECR, and MIE improve upon three major faults of RIE; namely the slow etch rate, surface damage, and isotropic etch profiles. Table I is a summary of the four different etching methods and some typical etching parameters along with the corresponding etch rates.

Table I. Etch Rate Parameters for Dry Etching of GaN

Maximum Etch Rate (nm/min)	Plasma Gasses	Pressure (mTorr)	Power (watts)	DC Bias (- volts)	Reference
700	Cl ₂ /H ₂ /Ar	1	750	280	[9] ICP
900	NM#	1	1000	290	[9] ECR
285	Cl ₂ /H ₂ /CH ₄ /Ar	2	275	NM#	[11] ECR
110	Cl ₂ /H ₂	1	1000	150	[1] ECR
110	HI/H ₂ /Ar	1	1000	150	[8] ECR
90	HBr/H ₂ /Ar	1	1000	150	[8] ECR
350	BCl ₃	7	NM#	100	[2] MIE
105	BCl ₃	10	150	231	[4] RIE
60	HBr/Ar	50	NM#	350	[6] RIE
50	SiCl ₄ /Ar	20	NM#	400	[5] RIE

NM# designates a parameter that was not mentioned in the reference.

C. Experimental Procedure

Experimental Apparatus. Figure 1 shows the basic etching setup. It consists of an inductively coupled plasma etcher, gas handling/storage, gas scrubber, optical emission spectrometer, and Laser Reflectance Interferometer. The etcher consists of a custom designed and built stainless steel chamber with a loadlock, with a water cooled anodized aluminum cathode. A 2000w 13.56 MHz power generator and autotuning matching network provide power to the inductive source antennae for plasma generation. Pressure in the chamber is monitored by an MKS 627A Capacitance Manometer. A Leybold mechanical pump and an Alcatel turbomolecular pump maintain the proper level of vacuum required for processing along with a base pressure of 4E-7 Torr.

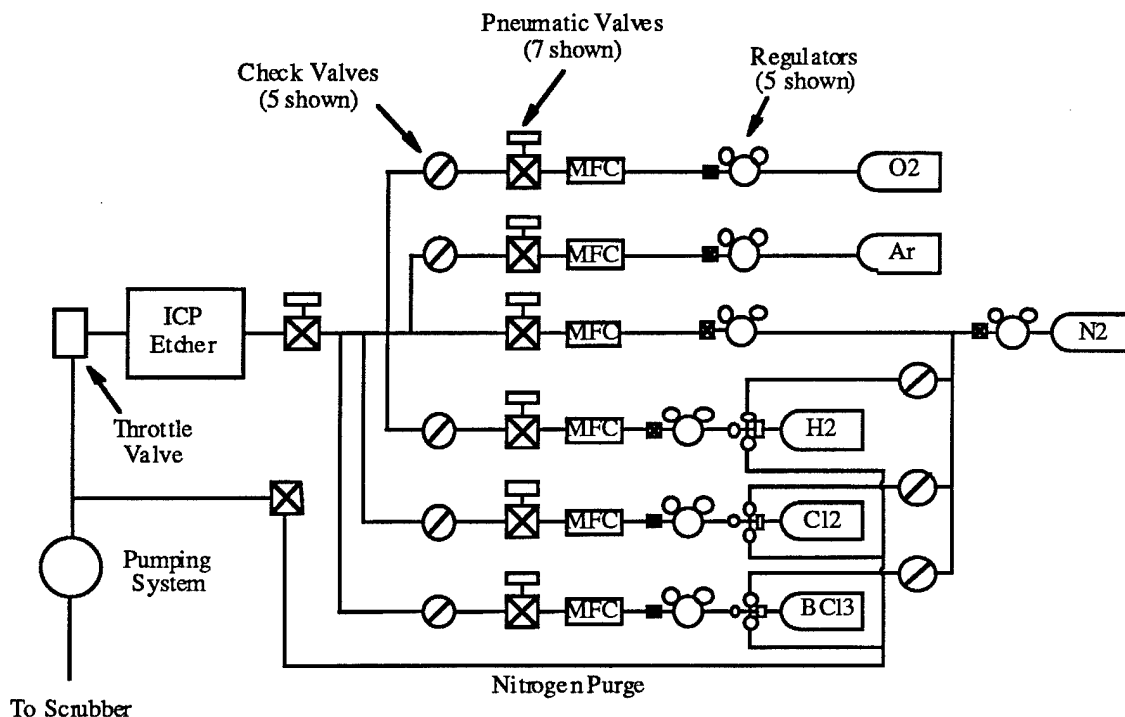


Figure 1. ICP schematic diagram.

Choice of Process Gasses. The gasses that the etching system will be capable of using are BCl₃, Cl₂, H₂, O₂, N₂, and Ar. Chlorides have proven to be effective gasses to etch GaN [1,2,4,8,11].

Etching Procedure. An etching procedure has not yet been fully developed. Photoresist is still being tested as an etch mask. It was originally thought to work well, but further testing has shown erosion of the photoresist.

The analytical tools that are used to characterize the etch are a profilometer for the step height, an SEM for the slope of the step, AFM for the surface roughness, and AES/XPS to observe the residual gas species on the sample surface. Schottky contacts are also going to be deposited to see how etching affects the barrier height, ideality factor, and leakage current [12].

D. Results and Discussion

Construction is complete for the new ICP etching system. Minor finishing details are being tended to and tests are being performed.

Preliminary results have shown etch rates of 4400 Å/min. using Cl₂/Ar/H₂ for the process gasses. The surfaces look smooth under an SEM with sidewall of approximately 55° with 90° being vertical. Figure 2 shows a typical etch profile obtained in the preliminary studies. The reason for the slope of the etch appears to be erosion of the photoresist mask. If the sidewalls of the photoresist mask are not vertical, then the resultant profile of the etch will not be vertical.

Figure 3 shows an example of this effect. The original mask was $1\mu\text{m}$ thick and eroded down to approximately $.3\mu$ thick. Figure 4 shows an etched sample from the edge of the sample where the photoresist is thicker. The sidewall is closer to being vertical than in Figs. 2 and 3.

E. Future Research

Once the problem of mask erosion is worked out, parametric studies will be done varying the process gas and flow rates, ICP and RF power, and pressure to determine which combination yields the fastest etch rates and least surface damage/contamination. This will be aided as with the use of Laser Reflectance Interferometry to get *in situ* etch rates. Optical emission spectroscopy will be used to aid in the understanding of the plasma chemistry when

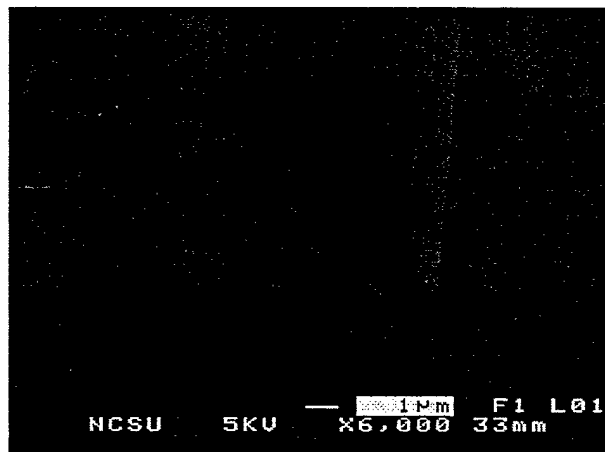


Figure 2. Typical etch profile obtained in the preliminary studies.

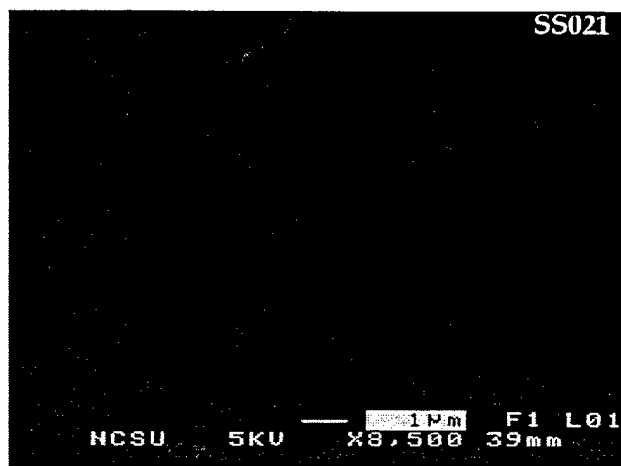


Figure 3. The resultant profile of the etch will not be vertical if the sidewalls of the photoresist mask are not vertical.

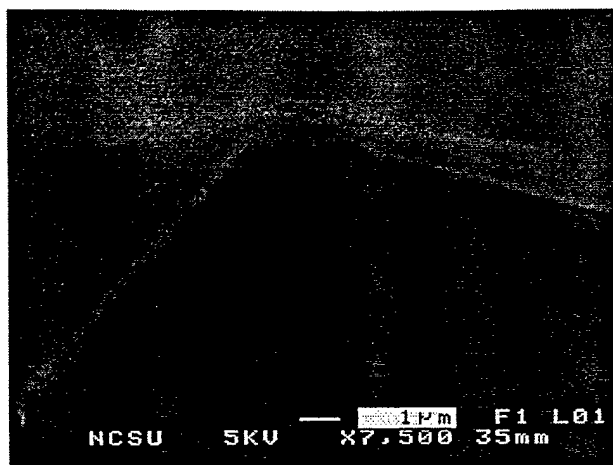


Figure 4. Etched sample from the edge of the sample where the photoresist is thicker.

etching the III-N materials. The primary gasses are going to be chlorides, but the use of other gasses may be explored. Surface analysis techniques will be employed to determine the roughness of the surface, etch profiles, step height, and surface contamination. Since the end product of the III-N research is electronic devices and optoelectronic devices, knowing the effects of etch induced surface damage is very important. If an etched surface is highly contaminated or very rough, it may not be good for electronic and optoelectronic devices. Determining the surface effects is equally important as determining the etch rates. Other effects such as heating or cooling the sample may also be explored. The ultimate goal of this research is to etch anisotropic features with etch rates suitable for industry, and damage/contamination free etch surfaces.

F. References

1. S. J. Pearton, C. R. Abernathy, F. Ren, Appl. Phys. Lett. **64**, 2294 (1994).
2. G. F. McLane, L. Casas, S. J. Pearton, C. R. Abernathy, Appl. Phys. Lett. **66**, 3328 (1995).
3. S. J. Pearton, C. R. Abernathy, F. Ren, J. R. Lothian, P. W. Wisk, A. Katz, J. Vac. Sci. Technol. A **11**, 1772 (1993).
4. M. E. Lin, Z. F. Fan, Z. Ma, L. H. Allen, H. Morkoc, Appl. Phys. Lett. **64**, 887 (1994).
5. I. Adesida, A. Mahajan, E. Andideh, Appl. Phys. Lett. **63**, 2777 (1993).
6. A. T. Ping, I. Adesida, M. A. Khan, J. N. Kuznia, Electronics Letters **30**, 1895 (1994).
7. S. J. Pearton, C. R. Abernathy, F. Ren, J. R. Lothian, P. W. Wisk, A. Katz, C. Constantine, Semicond. Sci. Technol. **8**, 310 (1993).
8. S. J. Pearton, C. R. Abernathy, C. B. Vartuli, Electronics Letters **30**, 1985 (1994).
9. R. J. Shul, Presentation Viewgraphs
10. M. Mortagh, P. V. Kelly, P. Herbert, M. O'Connor, G. Duffy, G.M. Crean, Applied Surface Science **63**, 158 (1993).
11. R. J. Shul, A. J. Howard, S.J. Pearton, C.R. Abernathy, C.B Vortuli, P.A. Barnes, M. J. Bozack, J. Vac. Sci. Technol. B **13**, 2016 (1995).
12. G. F. McLane, W. R. Buchwald, Mat. Res. Soc. Symp. Proc. **340**, 221 (1994).

XI. Ion Implantation, Annealing and Microstructural Investigations in GaN Thin Films

A. Introduction

The control of the electrical properties of the III-V nitride semiconductors is a major obstacle in the development of these materials for use in optoelectronic and microelectronic devices. To date, the majority of the research has been concentrated on the growth of the material with the desired properties, while very little research has been performed on post-growth processing to achieve the desired electrical properties. One post-growth processing method that is widely used in the semiconductor industry but that has gotten little attention concerning the III-V nitrides, is ion implantation. Ion implantation is a convenient method to incorporate electrically active dopants into the host crystal, post growth, using a highly-energetic beam of ions that strike and penetrate into the crystal. This method allows for a precisely controlled amount of impurity to be introduced into the crystal independent of the solubility of the impurity. The major drawback of this method is the enormous amount of damage that is induced on the host crystal due to the kinetic energy of the impinging ions.

The most comprehensive study of ion implantation in the nitrides is the historic work of Pankove and Hutchby [1,2]. In this article, 35 ion species were implanted into gallium nitride and the photoluminescence was reported. It was found that Mg, P, Zn, Cd, Ca, As, Hg, and Ag were the only ion species that gave a characteristic photoluminescence signature with Zn being the most efficient radiative center. The other ions all showed a broad peak around 2.15 eV which is thought to be implantation induced and a peak around 1.75 eV which is thought to be due to the annealing treatment as it was seen in the control sample after annealing. Wilson *et al.* performed a more recent study of Er-implanted GaN and AlN [3] The Er^{3+} was coimplanted with oxygen and showed optically excited 1.54-micron luminescence. In both these studies, data on the electrical behavior of the material was not given.

Wilson *et al.*, in another study, implanted several key elements for the purpose of studying the distribution of the implanted species in the nitride films [4]. The ions implanted were Be, C, Mg, Zn, Si, S, Ge, and Se. Wilson *et al.* found that in most cases the distribution followed a Gaussian behavior. Also Wilson *et al.* studied the redistribution of the implanted species in the films with a post implantation anneal. It was found that even with anneals up to 900°C the distribution of the implanted species did not change except for S which started to redistribute above 600°C and for Zn and Se which redistributed above 800°C. Again, data on the electrical behavior of the material was not given.

Very little work has been presented on the electrical characterization of the implanted layers. Rubin *et al.* were the first to show, by hot-probe tests, P-type material upon implantation of Mg into intrinsic GaN. This was the first paper to deal with the electrical behavior of the implanted films. The film had a resistivity of 4 Ω/cm [5]. Binari *et al.* reported on the

implantation of H, He, and N to produce semi-insulating GaN. The He implant produced films with as-implanted resistivities as high as $10^{10} \Omega\text{-cm}$. This implanted material remained highly resistive after annealing up to 800°C . N also produced resistive GaN, after an anneal at 400°C . Samples of H were highly resistive upon implantation but after an anneal at 300°C the resistivity dropped to less than $10 \Omega\text{-cm}$ [6]. Pearton *et al.* performed a detail study of the electrical behavior of implanted GaN. In this study activation of both an n- and p-type dopant were achieved. Si^+ was implanted for n-type while Mg^+/P^+ was implanted for p-type. The dopants became activated, 93% for Si and 62% for Mg, after an anneal at $\sim 1100^\circ\text{C}$ [7]. This shows that post growth processing of the GaN can be used to achieve the desired electrical properties for the material.

B. Experimental Procedure

Gallium nitride is grown by MOCVD in this lab on $\alpha\text{-SiC}$ substrates. Several ions are being investigated for ion implantation and electrical activation in the GaN films including Si, Mg and Ca/P. The ions are Si, for N-type; Mg, for P-type; and Ca/P for P-Type. The energies, doses, and temperature of the implants can be seen in Tables I, II, III respectively for the ions.

C-V measurements, RBS/C and PL were performed on the samples after the implantation. The samples were then annealed at 900°C and 1100°C and characterized again using C-V measurements, photoluminescence and RBS/C. The cross-sectional TEM samples were made after implantation by cutting two pieces of the specimen and gluing them together face on. Two Si support pieces were also glued to the outside of the specimen sandwich. The sample was then ground down, polished, dimpled, and ion milled as described in [8] to get a proper TEM sample. The specimens were then imaged using a TOPCON EM0002B electron microscope and a Philips CM200 FEG.

C. Results and Discussion

The electrical characterization, performed by C-V measurements, showed that activation of the species was not achieved as implanted. This result was expected as Pearton, *et al.* had to anneal the implanted species greater than 1050°C in order to achieve activation [7]. RBS/C showed that the samples exhibited no damage as compared to a virgin sample for the Si and Mg ions. This was unexpected as the high doses ($1\text{e}15 \text{ cm}^{-2}$) would have caused considerable damage in other semiconductor materials (i.e. Si and GaAs). For the Ca/P ions small damage was seen after implantation with the largest damage being present in the samples with the largest dose of $4\text{e}15 \text{ cm}^{-2}$ as is seen in Fig. 1. Damage was expected at this dose level, however, the relative amount of damage in this material is much lower than in other semiconductor materials.

Table I. Mg Implantation

Ion	Energy (KeV)	Dose (c ⁻²)	Implant Temp (°C)
Mg,24	120	1e14	500
Mg,24	120	5e14	500
Mg,24	120	1e15	500
Mg,24	120	5e14	RT

Table II. Si Implantation

Ion	Energy (KeV)	Dose (c ⁻²)	Implant Temp (°C)
Si,29	160	1e14	500
Si,29	160	5e14	500
Si,29	160	1e15	500
Si,29	160	1e14	RT
Si,29	160	5e14	RT
Si,29	160	1e15	RT

Table III. Ca/P Implantation

Ion	Energy (KeV)	Dose (c ⁻²)	Implant Temp (°C)
Ca,20/P,15	180/130	5e14	550
Ca,20/P,15	180/130	1e15	550
Ca,20/P,15	180/130	4e15	550
Ca,20/P,15	180/130	5e14	RT

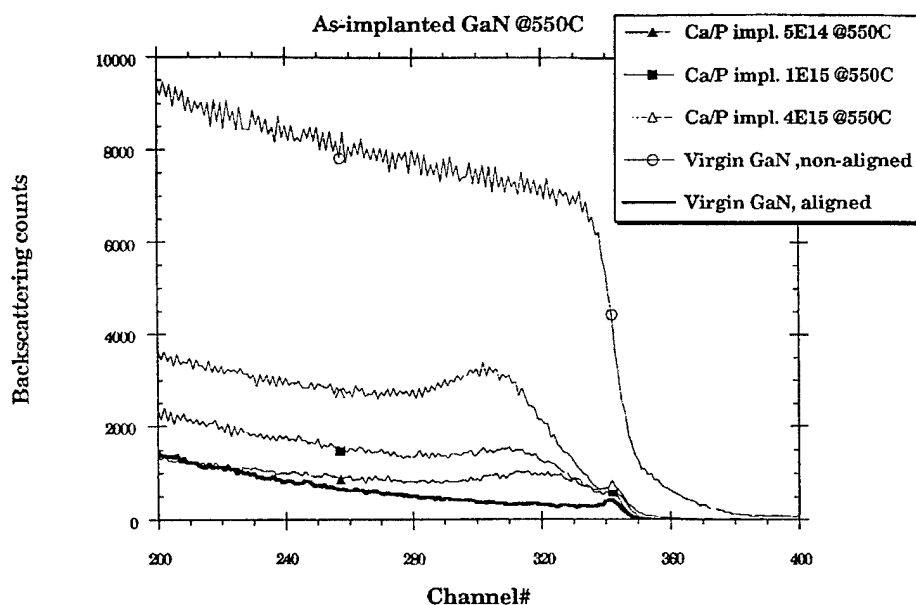


Figure 1. RBS/C of Ca/P samples implanted at 550°C.

The PL spectra showed that no emission was detected from the implanted regions of the samples even at the lowest dose. This was in contrast to the band edge emission that was observed on the same samples in the regions that were not implanted due to the clip used to mount the samples in the implanter. This implies that considerable damage indeed occurred contrary to the RBS/C results. All cross-sectional TEM images were taken in a $[1\bar{1}20]$ orientation. Figure 2 shows a cross-sectional TEM image of GaN implanted with Mg at 550°C. As can be seen in the figure, there is a damaged layer near the top surface of the film which is ~275 nm thick.

Figure 3 shows an enlarged image of this damage layer. Figure 4 shows a cross-sectional TEM image of GaN implanted with Si at 550°C. As can be seen in the figure, there is a damaged area near the top surface of the film which is ~295 nm thick.

Figures 5 and 6 show high resolution TEM (HRTEM) images GaN implanted with Mg at 550°C. Figure 5 is from an undamaged region of the GaN film while Fig. 6 is from a region of the GaN damaged by the implantation process. The arrows in Fig. 6 indicate areas of potential damage.

The implantation damage observed in Figs. 2, 3, and 4 is similar to damage observed in ion-implanted silicon [9,10,11]. The implantation process damaged the top surface of the GaN film at both RT and 550 C, but a completely amorphous region was not formed. This result indicates that the implantation dose was not high enough to cause complete amorphization of the implanted region [9], but was high enough to either (1) cause small "packets" of amorphous regions in the damaged layer or (2) form point defects (vacancies and interstitials) in the damaged region. The TEM images do not correlate well with the data from RBS/C measurements which show an undamaged sample.

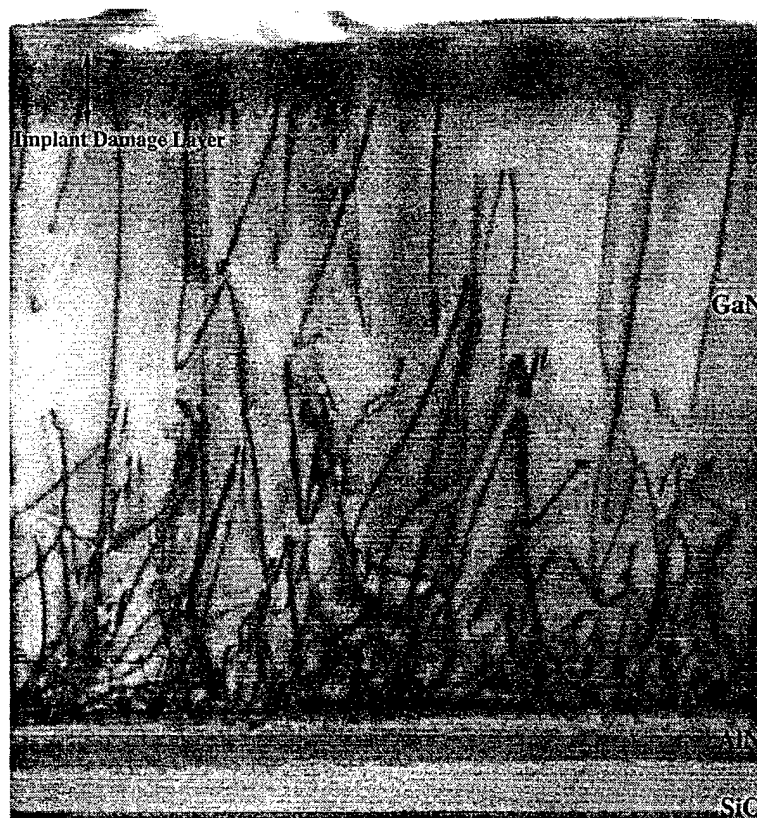


Figure 2. TEM image of Mg implanted GaN film. The implant damage layer is ~275 nm thick.

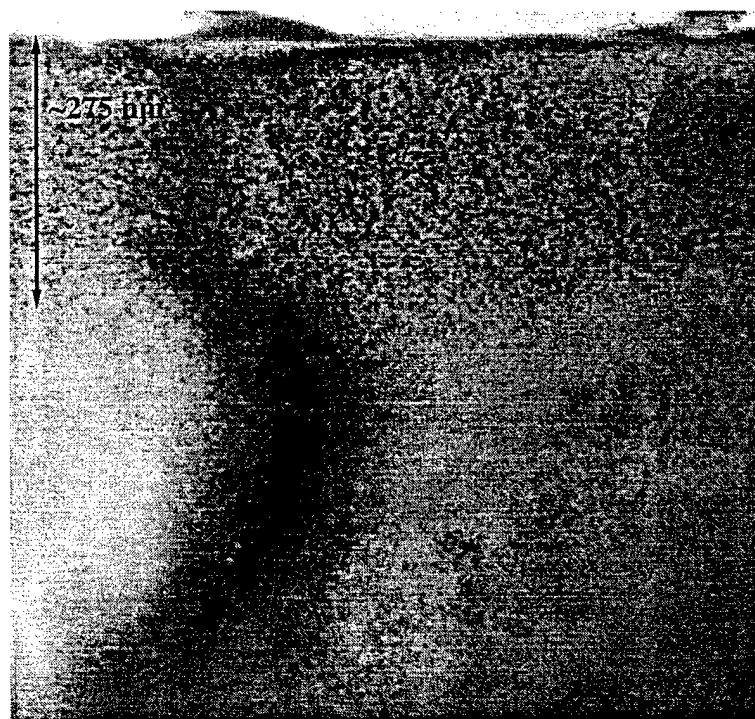


Figure 3. TEM image of damaged layer in a Mg implanted GaN film.

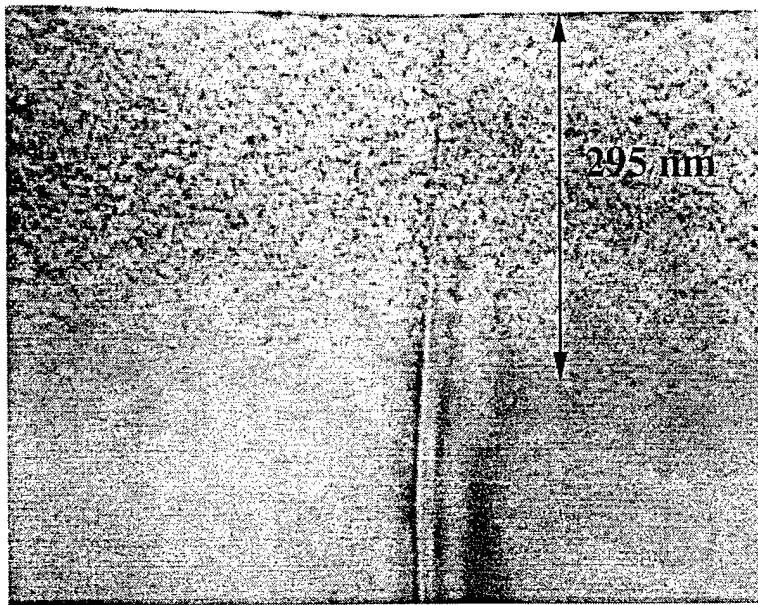


Figure 4. GaN film implanted with Si at 550°C.

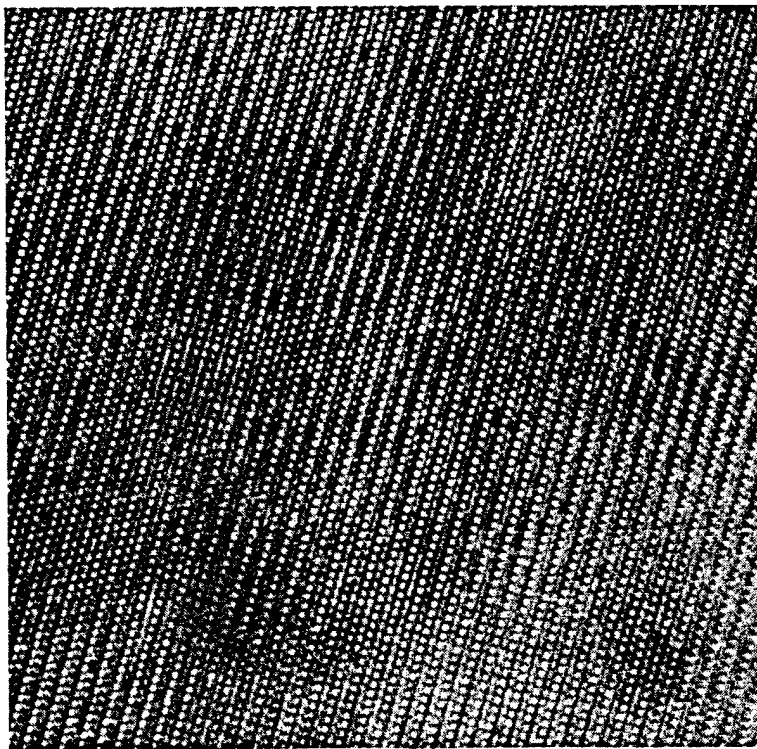


Figure 5. HRTEM of undamaged GaN layer.

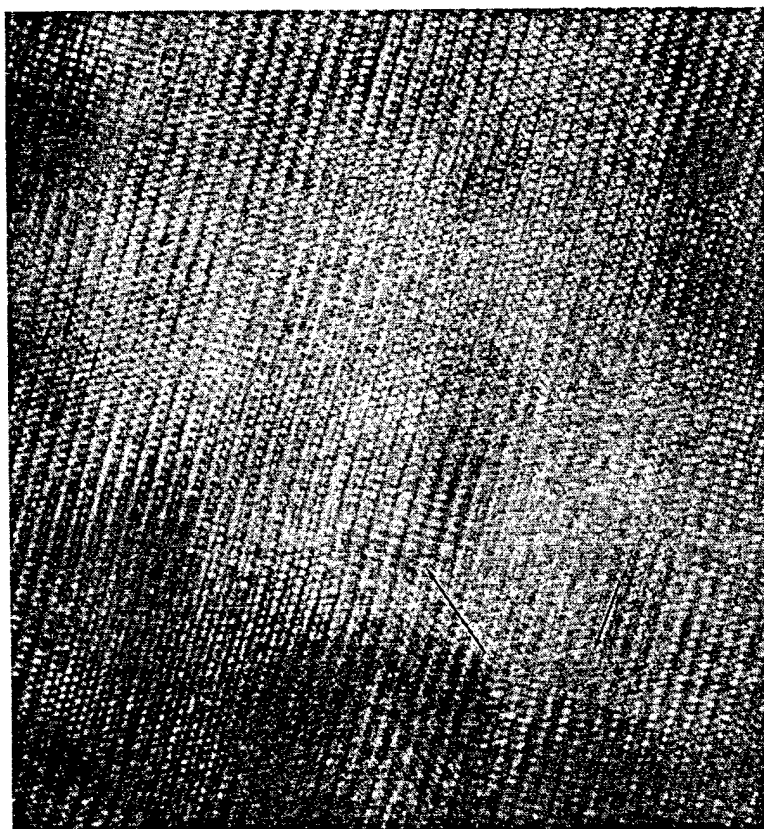


Figure 6. HRTEM of damaged region in Mg implanted GaN. The arrows point to areas of possible implantation damage. The exact nature of the damage, however, could not be determined using HRTEM.

Upon annealing the samples to 900°C for 60 sec. no electrical activation of the species was seen for Si or Mg. The PL spectrum again did not show any emission from the implanted regions of the samples. A 30 second 1100°C RTA anneal was performed in a face to face orientation with a virgin GaN sample in Flowing N₂ at atmospheric pressure. The surface of the samples degraded at this temperature possibly due to the escape of N from the surface region of the samples. Due to the surface degradation no electrical characterization was possible. The degradation was also apparent in RBS/C as the surface of the film became more “damaged” after annealing at 1100°C.

Also an initial annealing experiment for the Mg implanted samples was done to attempt to determine the exact nature of the implantation damage. One sample was annealed at 700°C for one minute in a RTA furnace. Another sample was annealed at 900°C for one minute. It was hoped that this annealing would reveal the nature of the implantation damage. If the damage was point defects, one should see a coarsening effect upon annealing. If the damage was amorphous regions, annealing should cause a gradual decrease in the damaged area as the annealing temperature is increased. Figures 7 and 8 show TEM images taken from these annealed samples. As is seen in the images, annealing appears to not have affected the damaged regions at all. A more extensive annealing experiment needs to be conducted.

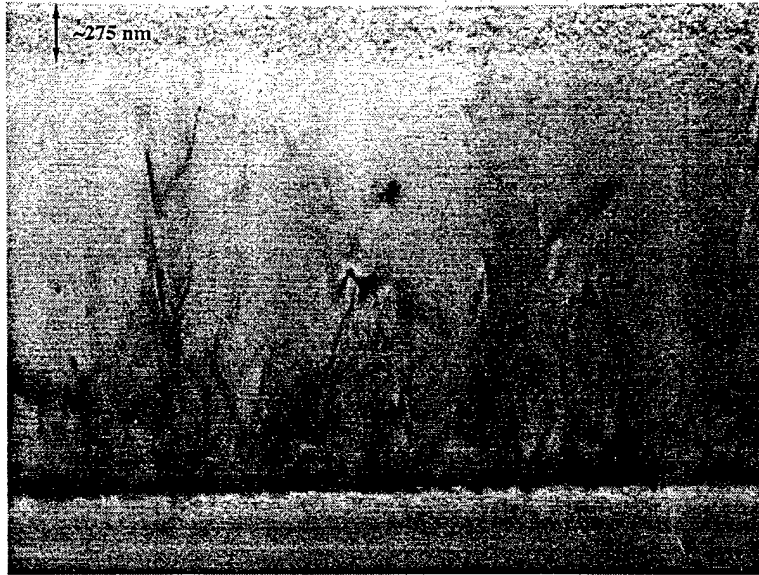


Figure 7. Mg implanted GaN samples annealed at 700°C for one minute.

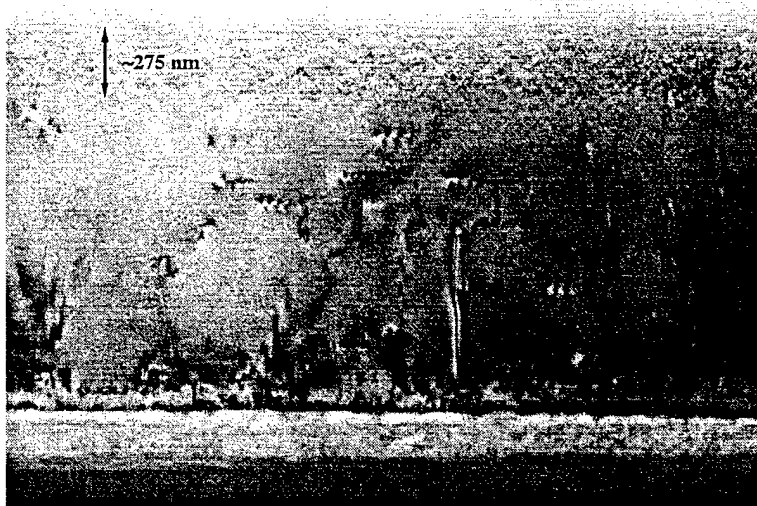


Figure 8. Mg implanted GaN sample annealed at 900°C for one minute.

D. Future Research Plans and Goals

The goal of the implantation is to achieve activation, thus the samples need to be annealed to activate the implanted species as was seen by Pearton, *et al.* An annealing schedule needs to be found that does not damaged the surface of the samples. Pearton, *et al.* annealed their samples at 1100°C for 10 sec. and they saw no degradation of the surface of the film. The time difference in the anneals may be the difference.

In order to determine the exact nature of the implantation damage, a series of annealing experiments is planned. By annealing a series of the implanted samples of GaN at progressively increasing temperatures and observing the microstructure using cross-sectional TEM, the exact nature of the damage should be revealed. If the damage is small packets of amorphous regions, the TEM images from the annealed samples should show a gradual decrease in the damaged area as the annealing temperature rises. If the damage is point defects, the TEM images from the annealed samples should show the formation of vacancy clusters and loops which should anneal out as the annealing temperature increases.

E. References

1. J. I. Pankove, and J. A. Hutchby, *J. Appl. Phys.* **47**, 5387 (1976).
2. J. I. Pankove, and J. A. Hutchby, *Appl. Phys. Lett.* **24**, 281 (1974).
3. R. G. Wilson, R. N. Schwartz, C. R. Abernathy, S. J. Pearton, N. Newman, M. Rubin, T. Fu, and J. M. Zavada, *Appl. Phys. Lett.* **65**, 992 (1994).
4. R. G. Wilson, S. J. Pearton, C. R. Abernathy, and J. M. Zavada, *Appl. Phys. Lett.* **66**, 2238 (1995).
5. M. Rubin, N. Newman, J. S. Chan, T. C. Fu, and J. T. Ross, *Appl. Phys. Lett.* **64**, 64 (1994).
6. S. C. Binari, H. B. Dietrich, G. Kelner, L. B. Rowland, K. Doverspike, and D. K. Wickenden, *J. Appl. Phys.* **78**, 3008 (1995).
7. S. J. Pearton, C. B. Vartuli, J. C. Zolper, C. Yuan, and R. A. Stall, *Appl. Phys. Lett.* **67**, 1435 (1995).
8. G. M. Ma and S. Chevacharoenkul, MCNC Technical Report TR90-33 (1990).
9. J. Narayan, and O. W. Holland, *J. Electrochem. Soc.* **131**, 11 (1984).
10. J. Narayan, D. Fathy, O. S. Oen, and O. W. Holland, *J. Vac. Sci. Technol. A* **2**, 3 (1984).
11. J. Narayan, O. S. Oen, D. Fathy, and O. W. Holland, *Mat. Letts.* **3**, 3 (1985).

XII. III-V Nitrides for Use in Semiconductor Microelectronic Device Applications

A. Introduction

With their distinct combination of physical and electronic properties the III-V nitrides are promising materials for optoelectronic and microelectronic applications; AlN, GaN, and InN have direct band gaps of 6.2, 3.2, and 1.9 eV respectively. In conjunction with their continuous solid solubility, one has the ability to engineer band gaps within the range of 1.9 to 6.2 eV, which can be used to construct blue LEDs and deep UV lasers.

Along with their wide band gaps the III-V nitrides have advantageous physical properties such as high thermal stability, high physical hardness, and high chemical stability. In combining these properties the III-V nitrides lend themselves as excellent candidates for high-power and high-temperature devices [1].

At present, there is one significant drawback to the use of the III-V nitrides, the lack of a homoepitaxial substrate. In order to achieve monocrystalline thin films, heteroepitaxy has been employed using a number of different substrates. This method has allowed the production of single crystal films, but the films have had poor crystal quality and high unintentional doping levels [2].

Recent developments have shown that good single crystal thin films of AlN and GaN can be grown using techniques such as metal organic chemical vapor deposition (MOCVD) and molecular beam epitaxy (MBE) [3-7]. The most successful of these films, which exhibit high resistivity and low unintentional doping, have been grown on Al₂O₃ (sapphire) and α -SiC. Conductive n and p-type GaN films have also been produced using the appropriate doping impurities.

With the production of device-quality material, successful attempts have been made to produce microelectronic devices using the III-V nitrides [8-15]. Khan *et al.* have made many strides in this area, including being the first to fabricate a MESFET device from the nitrides. Binari *et al.* have also fabricated MESFET devices along with MISFET structures. As shown in Fig. 1, Binari fabricated an depletion mode device using Si₃N₄ as the gate insulator. For a gate length of 0.9 μ m, the transconductance was 16 mS/mm at 30°C and 11 mS/mm at 200°C. The frequency response of these devices were measured resulting in an f_T and f_{max} of 5 and 9 GHz respectively [15].

Currently much of the research concerning MISFET devices is directed towards depletion mode devices. This can be attributed to the inability to successfully process the material. Currently many strides have been made in the areas of implantation and etching [16-18]. Other areas of research which are beginning to be addressed include the investigation of insulator

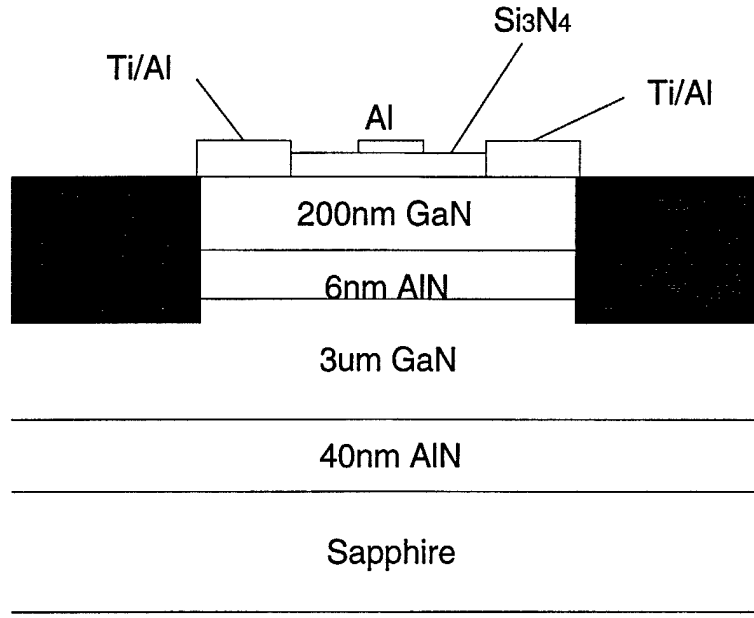


Figure 1. MISFET cross section.

materials. Some initial work has been done by Casey *et al.* on SiO₂-GaN MOS capacitors [19]. His results indicate that SiO₂ grown on GaN by a remote plasma method yielded a structure with low interface trap density.

It is the plan of this project to complete the steps needed to construct a MISFET structure. The steps will be discussed further in the following section.

B. Results

In order to produce a viable IGFET device a suitable insulating material must be found to use as the gate insulator. Three materials have been chosen to be investigated for this research. They include SiO₂, Si₃N₄, and AlN. To properly study the characteristics of the insulators on the semiconductor metal insulator semiconductor capacitors used.

To theoretically model these devices modified versions of the equations derived for two terminal devices Si, from Tsividis [20] and Nicollian and Brews [21], are used. Due to GaN's long generation rate and short minority carrier lifetime, on the order of 10¹¹ years and 10⁻⁸s respectively, the inversion layer contribution to the capacitance can be ignored. This leaves only the accumulation and depletion modes to characterize. From this analysis an equation for the semiconductor capacitance is derived:

$$C_c(y) = \left[F \frac{\sqrt{N_d}}{2} \left(\phi_i e^{\left(\frac{\psi}{\phi_i} \right)} - \psi - \phi_i \right)^{-\frac{1}{2}} \cdot \left(e^{\left(\frac{\psi}{\phi_i} \right)} - 1 \right) \right] A \quad (1)$$

Where $F=(2q\epsilon_{\text{GaN}})^{1/2}$, N_d is the semiconductor doping concentration, ϕ_t is the thermal voltage, and ψ is the surface potential. Substituting the results of the equation 1 into the following equation,

$$C_t(\psi) = \left(\frac{1}{C_{ox}} + \frac{1}{C_c(\psi)} \right)^{-1} \quad (2)$$

where C_{ox} is the capacitance of the insulator, the capacitance for the device can be calculated at various surface potentials. The equation for the gate voltage is derived from the potential drops across the capacitor:

$$V_{gb}(\psi) = V_{fb} - \frac{Q_{cs}(\psi)}{C_{ox}} - \psi \quad (3)$$

where V_{fb} is the flatband voltage and $Q_{cs}(\psi)$ is the charge at the semiconductor/insulator interface. From the above equations a theoretical C-V curve can be generated for n-type MIS capacitors.

This research group has demonstrated the ability to grow high quality single crystal thin films of GaN and AlN with high resistivity and low levels of unintentional doping. These films have been grown by MBE and MOCVD on α -SiC, utilizing a high temperature monocrystalline AlN buffer layer. Through these methods both n and p type doping of the GaN films has been achieved.

Using the n-type GaN Grown by MOCVD (MIS) capacitors have been fabricated. These devices were fabricated in a lateral orientation rather than the typical vertical orientation used in silicon technology. This was done to avoid the insulating AlN buffer layer. Silicon oxide was grown via a low temperature chemical vapor deposition process and by a remote plasma-enhanced CVD process [22]. The LTCVD oxide was deposited at the microelectronics laboratory located at North Carolina State University and the RPECVD oxide was deposited by G. Fountain at Research Triangle Institute, Research Triangle Park, NC. Aluminum was used as the gate metal and the ohmic contact for this device.

Capacitance-voltage measurements were performed using a HP4284A precision LCR meter in conjunction with MDC software. The resulting curves from the LTCVD oxides showed that a large amount of leakage was taking place when the device was biased in the accumulation range. This large leakage prevents accurate data from being obtained. In an attempt to overcome the leakage annealing studies were performed at varying temperatures and with different gases. None of these attempts were successful. It was surmised that the use of e-beam evaporation to deposit the Al contacts was introducing defects into the oxide from the x-ray produced during post anneal processing which lead to the large leakages.

The initial C-V measurements completed on the RPECVD oxide capacitors, which were fabricated using thermal evaporation to deposit the Al contacts, indicate that the leakage is much

lower than in any previous capacitors. Studies into the interface trap characteristics are currently ongoing utilizing hysteresis and varying temperature C-V measurements.

To properly analyze C-V curves a good theoretical curve must be obtained. At this juncture a piece of information is missing that is needed to complete a proper curve. The value of the flatband voltage, which is the difference in the workfunctions of the gate metal and the semiconductor, is unknown because the workfunction of GaN has not been quantified. A solution to this problem has been devised and will be discussed further in the following section.

C. Discussion

Now that functional two terminal oxide devices have been fabricated proper analysis on the characteristics of the insulator must be completed. Further work must also be done to determine if other insulating materials are better candidates for use as the insulators in the IGFET structures.

To reach the goal of an IGFET device advances in material processing need to be made. Specifically in the areas of contacts, ion implantation, and etching. All of which are currently being addressed within this research group.

D. Conclusion

With their combination of thermal and electrical properties the III-V nitrides have the potential to be excellent materials for use in high-power and high-temperature applications. With the production of device quality material the time has arrived to develop these devices. There are a number of factors that will determine when fabrication will be realized. It is the goal of this project to complete the work needed to achieve a working device.

E. References

1. R.F. Davis, Proc. IEEE **79**, 702 (1991).
2. S. Strite and H. Morkoç, J. Vacuum Sci. Technol. B **10**, 1237 (1992).
3. M. Asif Khan, J.N. Kuznia, J.M. Van Hove, D.T. Olson, S. Krishnankutty, and R.M. Kolbas, Appl. Phys. Lett. **58**, 526 (1991).
4. H. Amano, T. Asahi, and I. Akasaki, Jpn J. Appl. Phys. **29**, L205 (1990).
5. S. Yoshida, S. Gonda, and S. Misawa, J. Appl. Phys. **53**, 6844 (1982).
6. M. Hegems and H. C. Montgomery, J Phys. Chem Solids **34**, 885 (1973).
7. C. Wang and R.F. Davis, Appl. Phys. Lett. **63**, 990 (1993).
8. M. Asif Khan, J. N. Kuznia, A. R. Bhattarai, and D. T. Olson, Appl. Phys. Lett. **62**, 1786 (1993).
9. M. Asif Khan, J. M. Van Hove, J. N. Kuznia, and D. T. Olson, Appl. Phys. Lett. **58**, 2408 (1991).
10. M. Asif Khan, J. N. Kuznia, J. M. Van Hove, N. Pan, and J. Carter, Appl. Phys. Lett. **60**, 3027 (1992).
11. M. Asif Khan, A. R. Bhattarai, J. N. Kuznia, and D. T. Olson, Appl. Phys. Lett. **63**, 1214 (1993).

12. M. Asif Khan, J. N. Kuznia, D. T. Olson, W. J. Schaff, J. W. Burm, and M. S. Shur, Appl. Phys. Lett. **65**, 1121 (1994).
13. M. Asif Khan, M.S. Shur, J. N. Kuznia, Q. Chen, J. W. Burm, and W. J. Schaff, Appl. Phys. Lett. **66**, 1083 (1995).
14. S. C. Binari, L. B. Rowland, W. Kruppa, G. Kelner, K. Doverspike, and D. K. Gaskill, Electronics Lett. **30**, 1248 (1994).
15. S. C. Binari, L. B. Rowland, G. Kelner, W. Kruppa, H. B. Dietrich, K. Doverspike, and D. K. Gaskill, *Proc. 21st Int. Symp. on Compound Semiconductors*, September 1994, San Diego.
16. R. J. Shul, A. J. Howard, S. J. Pearton, C. R. Abernathy, C. B. Vartuli, P. A. Barnes, and M. J. Bozack, J. Vac. Sci. Technol. B **13**, 2016 (1995).
17. G. F. McLane, L. Casas, S. J. Pearton and C. R. Abernathy, Appl. Phys. Lett. **66**, 3328 (1995).
18. S. J. Pearton., C. B. Vartuli, J. C. Zolper, C. Yuan, and R. A. Stall, Appl. Phys. Lett. **67**, 1435 (1995).
19. H. C. Casey, G. G. Fountain, R. G. Ailey, B. P. Keller, Appl. Phys. Lett. **68**(13), 1850 (1996).
20. Y. P. Tsividis, *Operation and Modeling of the MOS Transistor*, McGraw Hill Book Co., New York, 1987.
21. E. H. Nicollian and J. R. Brews, *MOS (Metal Oxide Semiconductor) Physics and Technology*, John Wiley & Sons, New York, 1982.
22. G. G. Fountain, R. A. Rudder, S. V. Hattangady, R. J. Markunas, P. S. Lindorme, J. Appl. Phys. **63**(9), 4744 (1988).

XIII. Distribution List

Dr. Colin Wood Office of Naval Research Electronics Division, Code: 312 Ballston Tower One 800 N. Quincy Street Arlington, VA 22217-5660	3
Administrative Contracting Officer Office of Naval Research Regional Office Atlanta 101 Marietta Tower, Suite 2805 101 Marietta Street Atlanta, GA 30323-0008	1
Director, Naval Research Laboratory ATTN: Code 2627 Washington, DC 20375	1
Defense Technical Information Center 8725 John J. Kingman Road Suite 0944 Ft. Belvoir, VA 22060-6218	2